Natural and Drilling Induced Fractures in the Grosmont Formation, Alberta: Implications for the State of Stress

by

Micah L. Morin

A thesis submitted in partial fulfillment of the requirements for the degree of

Master of Science

in

Geophysics

Department of Physics

University of Alberta

Abstract

The Devonian Grosmont formation is a huge heavy oil carbonate reservoir located in northeastern Alberta that has an estimated 64.5 x $10^9 m^3$ initial oil in place. This thesis will focus on issues related to the in situ state of stress and the natural fracture statistics within the Grosmont formation as determined from the numerous image logs obtained at the site.

Natural fractures were interpreted from an image log data set of 22 wells and analyzed for preferred orientation using statistical tests and density contouring. Of the wells, 6 tested positive for a preferred fracture dip orientation striking north-south. Equal area lower hemisphere statistical contouring results also showed that fracture orientations preferred a north-south strike. Drilling induced tensile fracturing were observed in log data of 20 of the wells and the maximum and minimum in-situ horizontal stress orientations were determined using these to be 50°NE and 140° SE respectively with circular standard deviation 9°.

Vertical stresses were calculated by integrating bulk density logs to the Grosmont C and D units and values ranged from 6 - 9MPa. Since data for evaluating in-situ horizontal stress magnitudes were limited, a procedure was devised using concentrations of azimuthal hoop stress at the borehole wall to bound horizontal stress magnitudes. The procedure took advantage of the lack of borehole breakouts caused by shear failure and the existence of tensile failure in the borehole in conjunction with laboratory measurements of carbonates in literature. Horizontal stress magnitudes in the area were constrained to $11.6\ \text{MPa} - 15.0\ \text{MPa}$ for maximum horizontal stress and $5.4\ \text{MPa} - 6.6\ \text{MPa}$ for minimum horizontal stress. The stress regime was ascertained to be strike slip.

Using pore pressure data available in the area and carbonate frictional properties from literature, a fault stability analysis was preformed to identify fracture zones of stability. The study area was determined to be extremely stable while steeply dipping (>70°) fractures within the strikes of 45-70° of the maximum horizontal stress falling in the zone of instability. The implication of this are that these fractures won't slip, meaning no induced seismicity during production but more practically slow slip won't damage casings in-situ.

Acknowledgements

The excellent dataset in this thesis was provided by Laricina Energy Ltd. and Osum Oil Sands Corporation.

Sincere thanks to Dr. Doug Schmitt for his advice, guidance, encouragement and excellent editorial work on this thesis. He allowed this project to be my own. No matter how intensely busy his schedule was, he always found time to address issues I had. I've learned so much from Doug starting in his undergraduate rock physics course, during my undergraduate research project, in the field on numerous projects across the country and throughout my MSc degree.

I would also like to thank my office mates and friends: Nam Ong, Arif Rabbani, Chris Nixon, Tariq Mohammed and Ryan Ferguson. With whom I've spent countless hours collaborating with in and outside the office.

I must express my heartfelt thanks to my family for their unyielding support and encouragement during my years of study and throughout this project. I am especially grateful to my parents Arlene and Pierre to whom I owe more than I can repay.

Table of Contents

List of Tables

List of Figures

1. Introduction

1.1. Introduction

In Alberta, in-situ crude bitumen production has been steadily increasing this decade with in-situ production exceeding that of surface strip mining for the first time in 2012. The annual production of in-situ crude has increased an average of 11.5% per year in Alberta since 2002 (ERCB, 2013). This increase can be attributed to the improvements on recovery techniques such as steam assisted gravity drainage. These techniques have largely been applied to oil sands however, and there still remain large resources that are potentially recoverable within carbonates.

The Devonian Grosmont formation (Figure 1.1) is a huge heavy oil reservoir located in northeastern Alberta that has an estimated 64.5 x $10^9 m^3$ initial oil in place (ERCB 2013). Hosting approximately 24% of Alberta's crude bitumen, the Grosmont reservoir is a substantial portion of the 272.3 x $10^9 m^3$ in situ initial volume of oil in place. It is believed that this is the largest carbonate heavy oil reservoir in the world; hereafter we refer to it simply as the Grosmont.

Briefly, the Grosmont is a late-Devonian shallow-marine carbonate platform. Geographically the Grosmont reservoir is approximately 150 km wide and greater than 600 km long (Machel et al. 2012) (Figure 1.1). Bitumen also resides in adjacent carbonate formations, particularly the Nisku Formation. The unique aspect of this is that the bituminous formations lie immediately beneath the major geological unconformity between Paleozoic and Cretaceous rocks. That is, the Paleozoic rocks were initially at the surface and, as is the usual case for carbonate formations, this surface was highly karsted. Karsting results essentially from the dissolution of the carbonate rocks by acidic water over time and the resulting geomorphology contains a wide variety of features that include caves and dolines (sinkholes). The rock mass itself can be highly fractured and contain large vugs. This complexity is two edged in that it provides for generous amounts of rock void space that may be filled with hydrocarbons but at the cost of complicated development.

As a result, although the existence of the Grosmont reservoir has been known for some time, there still is little if any production from it. This is because the risks involved in producing such a viscous bitumen from the carbonates remain unknown. Investments in research and development of this resource have not been continuous and have depended greatly on the world price of petroleum.

The first large research program was initiated by the Alberta Oil Sands Technology and Research Authority (AOSTRA) together with a number of industry partners in the mid 1980's. A number of small pilot projects centred in Townships 87 and 88, Ranges 19-20, west of the 4th meridian were built at this time to test different strategies for enhanced recovery. However, geophysical technologies in the mid to early 1980's are not nearly as advanced as they are today and drilling and completions were started without any advance knowledge of subsurface conditions. Horizontal drilling, too, was still for many in the realm of science fiction and it was subject to, surprisingly in hindsight, considerable opposition. The lack of geological inputs combined with the use of vertical boreholes was problematic as much of the bitumen resides within complex karsted carbonate formations that varied rapidly both vertically (e.g. caves) and laterally (i.e. dolines or sinkholes). Vertical boreholes drilled only a few tens of metres away from one another would hit quite different geological conditions that confounded the intended production strategies. The decline in oil prices during the early 1980's that culminated in the drastic drop in 1986 forced an abrupt termination of the AOSTRA project. Much of the data collected then remained unanalyzed. For example, the extensive seismic data sets obtained during this work remained untouched, they were not integrated with one another and studied using modern technologies until recently (e.g., Ezeuko et al., 2015 , Ardakani et al., 2015).

There was little interest in pursuing the Grosmont further until the mid-2000's where activities again increased with leases being purchased by numerous operators, the most famous of which was the $M465 land acquisition by Royal Dutch Shell in 2006. The Alberta Research Council (currently Alberta Innovates) initiated their 'Carbonates Research Program' to first re-investigate the large mass of data collected during the 1980's. Regrettably, the results from this study remain proprietary.

Independent of this, Laracina Inc. and OSUM Inc. carried out their own research project that culminated in the Saleski pilot project in which the 'Steam Assisted Gravity Drainage' (SAGD) technique that is heavily employed in the oil sands was tested within the Grosmont carbonates. In contrast to the AOSTRA studies of the 1980's, Laracina and OSUM acquired exceptional sets of geological and geophysical data during the planning phases for the Saleski pilot; the data used in this thesis comes from these detailed studies on the geology inferred from the dense core sampling integrated with high resolution 3D seismic imaging (Russel-Houston & Gray 2014), on the

interpretation of geophysical logs and integration with core (Macneil, J. 2015), and on the overviews of the production engineering strategies (Mohebati et al. 2014). This thesis will focus on issues related to the in situ state of stress and the natural fracture statistics within the Grosmont formation as determined from the numerous image logs obtained at the site.

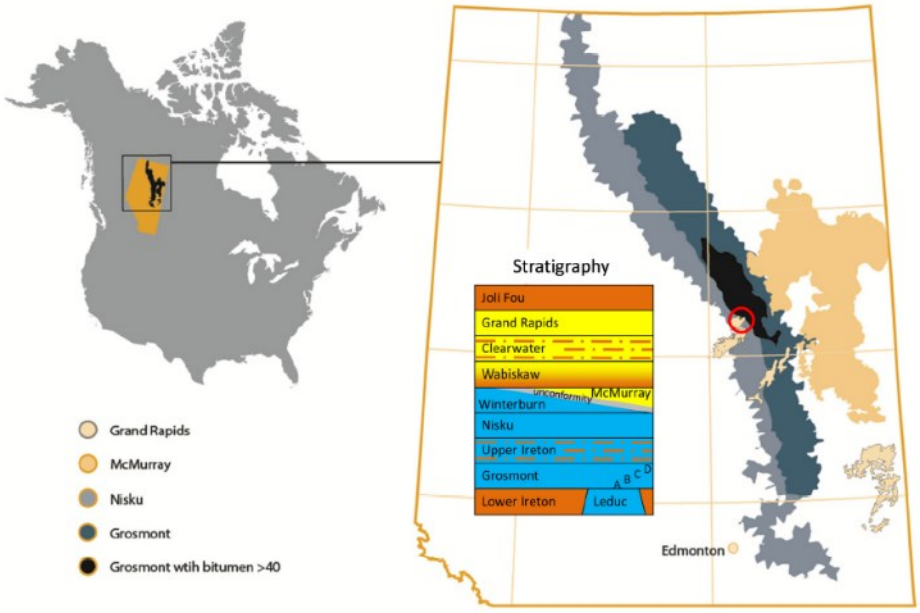

Figure 1.1: The Grosmont platform with the study area (red circle). The stratigraphic units are: brown – shale; yellow – sand; blue – dolomite and limestone. (modified from Russel-Houston & Gray 2014)

The region studied in this thesis is small spanning the Townships 84-85 and the Ranges 19-20, which provides an approximately 12 km by 10 km (Figure 1.1). Within this relatively small area we were granted access to 22 sets of image logs (Figure 1.2). A primary motivation of this study is the uniqueness of the data available in the subsurface. Similar fracture studies focusing on fracture density, fracture typology, fracture orientation and studies with a focus on subsurface stress may have few (2-5) wells with data let alone image log data (Genter et al. 1997, Brudy & Zoback 1999). These data can also be tens of kilometers apart from each other (Brudy & Kjørholt 2001). This study provides a unique opportunity for natural and drilling induced fracture identification and analysis of an abundance of good quality downhole image data. This is not only

an opportunity to study effects of macro stress orientations and the subsequent effects on the natural or drilling induced features but also to investigate the correlation between of such events between wells.

A further benefit in this study is the ability for direct comparison of the geologic features noted in the core and the downhole image data collected. Specifically of great interest in economic reservoirs are the fractures. In the Grosmont the fractures can provide fluid pathways during recovery processes increasing the effective permeabilities during extraction. Furthermore, matching in-situ downhole data with extracted samples, such as drilling chips, images drilled cores and further imaging techniques of cores, will contribute to the overall geologic picture of the subsurface. For instance, the ability to align the removed core with the reservoir rock downhole can yield a more complete understanding of the information extracted on the area as a whole.

In summary, the main purpose of this thesis is to employ borehole geophysical data primarily in the form of advanced digital image logs to better characterize the natural fractures and the in situ state of stress.

Chapter 2 contains background information to the current study. The first section provides a brief overview of the geological setting of the site. The second section reviews the necessary theory related to the description of stress and how it is concentrated by the borehole to produce indicators of crustal stress.

X-ray CT scans of some of the core collected were also made. Chapter 3 describes an attempt to put this information into a full 3D view and construct from its surface a 2D unwrapped image of the core. Such core scanning is standard in scientific drilling programs, but this technology has had difficulty being introduced to industry. We had hoped that this would allow the core (and hence the features within it) to be properly oriented by allowing direct comparison to the similarly unwrapped borehole image logs. While this showed promise, the relatively sparse CT scan sampling along the core did not produce sufficiently high resolution images. Regardless, the essential ideas are presented and may allow for application of this technique to future studies as is being used in the scientific drilling community.

Natural fractures are key to the development of such reservoirs as they will be the primary pathways through which fluids are delivered to the borehole from the formation. Using the

extensive series of image logs available from the project we analyze the fracture grouping, dips and preferred orientation of natural fractures.

The in-situ state of stress is studied from the image log data in Chapter 4. The data set is rich with drilling induced tensile fractures. This is somewhat surprising in that the Grosmont formation is at rather shallow depths of ~300 m to ~470 m. We find that the orientations of these drilling induced tensile fractures, which indicate the direction of the principal horizontal compression, are highly uniform. We further quantitatively constrain the state of stress by noting that only drilling induced tensile fractures exist and no borehole breakouts caused by shear failure were seen.

The thesis concludes in Chapter 5 with a summary of the results, a discussion of their implications particularly as regards the stress field in Alberta, and thoughts on future directions for this research.

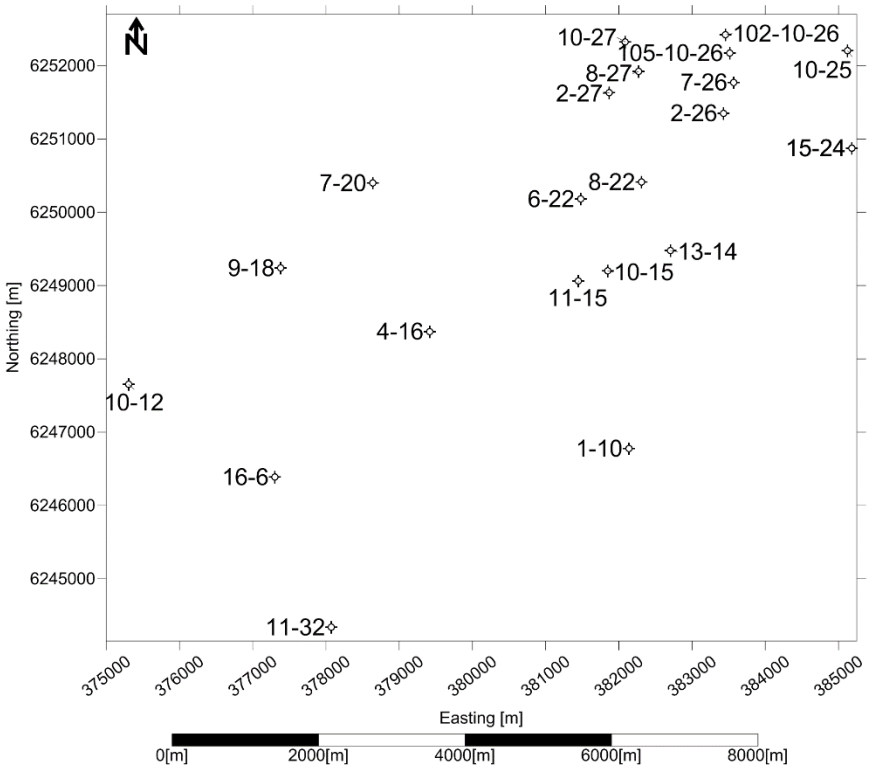

Figure 1.2: Local detail map of area of study Laricina Salenski plot showing relative locations of wells. In the map, each of the well positions is designated for brevity only by its Section and Township with the Range (either 19 or 20) and Meridian (all West of Meridian 4) excluded.

2. Background Information

2.1. Geological Structure

In this section we place the study area into the broader geological context. This includes the geological history and structure of the Grosmont Formation leading to a brief discussion of the knowledge of the state of stress in the Western Canada Sedimentary Basin.

The Grosmont member was first described using drill cuttings from the Imperial Grosmont No. 1 13-17-67-23W4 as well as cores from nearby wells were used by Belyea (1952) to first delineate the Grosmont. It was declared to be the Grosmont Formation by Law (1955). Its vast size consists carbonate platform nearly 400 km and a maximum width of 150 km covering an area of nearly 100000 km^2 was further outlined by Belyea (1956). The Bahama platform is a modern day analog in terms of environment and dimensions (Figure 2.1).

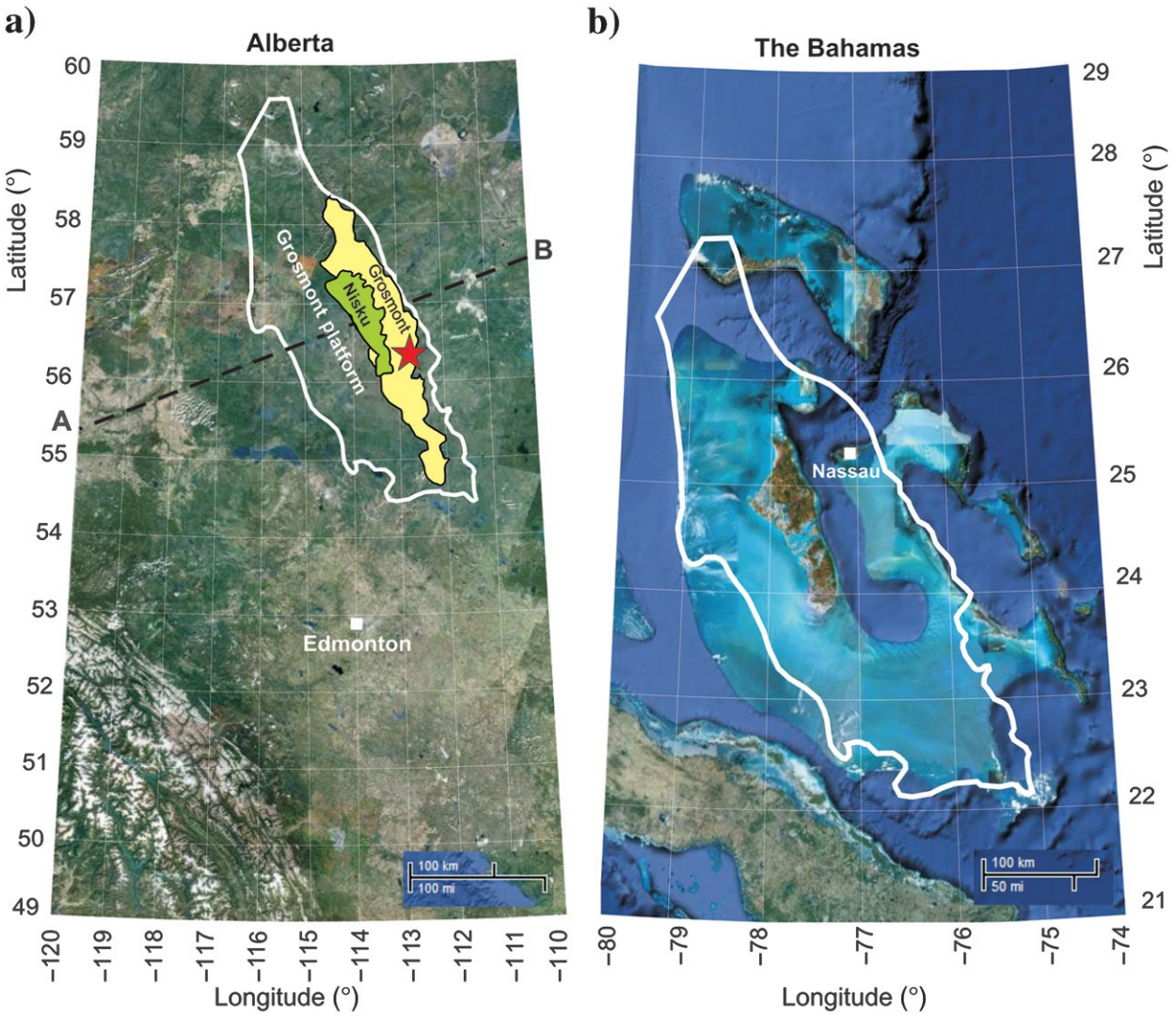

Figure 2.1: Comparision of satellite images over a) Alberta and b) the Bahama Banks. The extent of the Grosmont Platform is shown in white with the areas of bitumen saturation in the Grosmont and overlying Nisku Formations highlighted in yellow and green respectively. The red star denotes the area of the Saleski Pilot. The Grosmont platform is superimposed at the same scale over the Bahama Banks that is a modern analog. Figure from Ardakani and Schmitt (2014) with permission granted from the Society of Exploration Geophysicists through their Fair Use Policy.

In the Paleozoic (542 to 251 Ma) much of Alberta resided near the equator. In the later Devonian period (~416 to 360 Ma) this was passive continental margin submerged beneath a warm intracratonic extending from the Arctic to Wyoming. These warm seas gave ideal conditions for the deposition of vast quantities of limestone and shale. It also allowed the 300 m high reef complexes to grow. The Grosmont Formation is one of the lithologies deposited at this time of

rapid sedimentation. The Grosmont Formation is part of the larger Woodbend Group that includes a number of formations such as the Leduc reefs, the Duvernay calcareous mudstones which are an important source rock, and the Grosmont Platform.

It subsequently experienced subsidence and burial in which the Grosmont limestone was changed into dolomite. These formations were then uplifted and eroded; and it is useful to note that for the most part the geological record for the next 220 Ma is lost. What is known is that portions of the Grosmont Formation were at or near the Earth's surface at approximately 118 Ma because it lies immediately below the major geological unconformity separating the Devonian and Cretaceous deposits. Importantly, this put carbonate rock near the surface and because of this it is heavily karsted. Karst terranes exist whenever carbonates are exposed to the surface and there is the possibility that water can circulate. If the water is weakly acidic it will dissolve the carbonate forming both high porosity vuggy material and eventually leading to caves and dolines.

As the present day Rocky Mountains were up lifted approximately 118 Ma this added mass bent the lithosphere creating a depression that was filled with siliclastic sediments (sands and shales). The Cretaceous Mannville Group sediment above this unconformity are mostly flat-lying while the underlying carbonates dip to the south west at a shallow angle of only about 0.05° (Russel-Houston and Gray, 2014). At the project site, the Mannville Group, Lower Cretaceous Wabiskaw Formation lies immediately above the carbonates across the major unconformity.

Current models suggest that shortly after this uplift (10Ma) migration of large volumes of oil occurred into and through the Grosmont Formation. Because of proximity to the surface, the light oil was degraded into bitumen by bacteria present in the formation water with such processes perhaps continuing today.

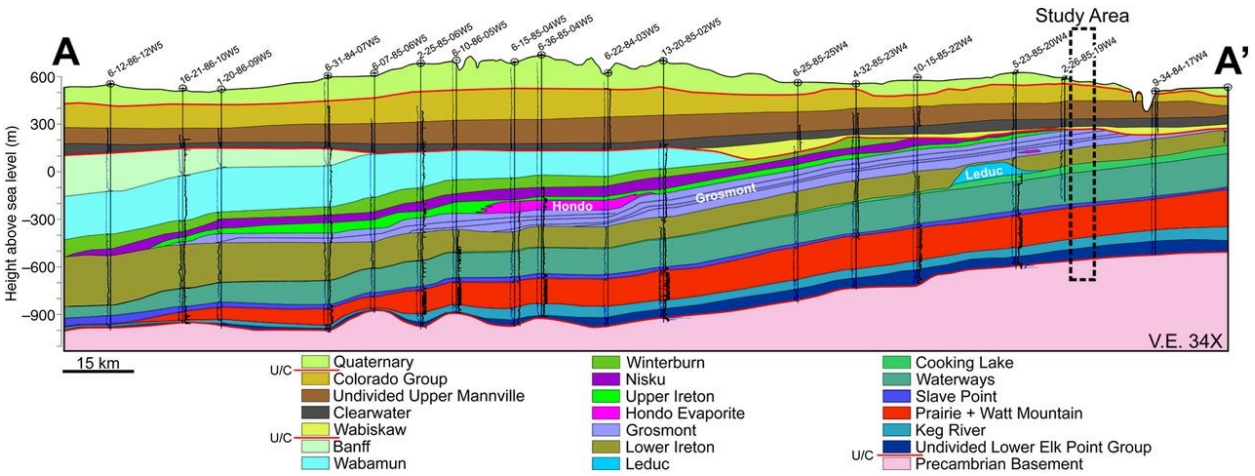

Figure 2.2: Regional geological cross section running from West to East through the study area illustrating the regional shallow dip of the Devonian carbonate deposits that are overlain by the Cretaceous siliclastic sediments. From Figure 3 of Russel-Houston and Gray (2014) used with permission of the American Association of Petroleum Geologists fair use policy (http://archives.aapg.org/pubs/aapgcopyright.cfm).

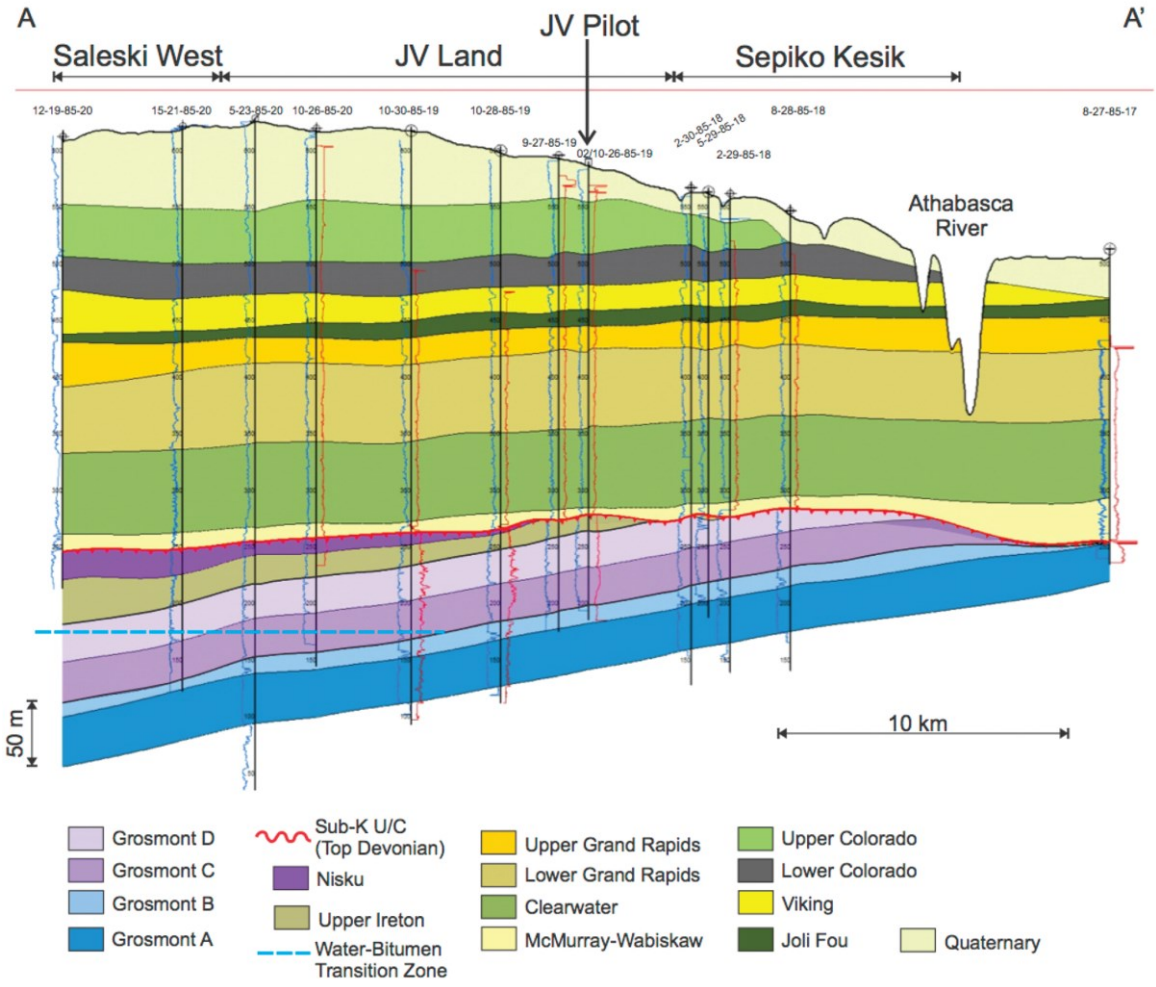

Figure 2.3: Detailed view of stratigraphy through the study site showing details of the informal separation of the Grosmont Formation into the A, B, C, and D units. Dashed blue line represents the approximate location of the bitumen-water contact. JV pilot indicates the location of the study area in the cross-section. From Figure 3 of (Macneil, J. 2015) used with permission in accordance with the Society of Professional Well Log Analysts permitted use policy (http://www.spwla.org/SPWLA/Publications/Journals/Society_Of_Petrophysicists_And_Well_Log_Analysts_Online_Journal_Member_License.aspx)

The Grosmont units are commonly assigned stratigraphic terminology in ascending order from first deposited to last and had initially been called by some workers the Lower Grosmont (LGM) and Upper Grosmont 1, 2, 3 (UGM 1, 2, 3) (e.g. Cutler 1982). This designation has not disappeared but more recently these same Grosmont units are also called in ascending age order as: A, B, C, D, respectively. Units A and B remain primarily limestone while C and D are pervasively dolomitized. Each unit is separated from the other by thin marl layers displaying higher natural gamma ray values; these are often called the 'Grosmont Shale Breaks'. Specifically, bitumen

mainly resides in the uppermost Grosmont C and D. A generic set of geophysical logs from the region for purposes of reference is provided in Figure 2.4 while one specific example log from the study site is shown in Figure 2.5.

At its greatest, the Grosmont C is about 33m thick when not disturbed by karsting. It is divided into three more sub units: the 13m thick Lower C Argillaceous Dolomite, the 13m thick Middle C and the 7m thick Upper C. The Lower Argillaceous dolomite contains a significant clay component and is fine grained and therefore not considered reservoir. There is an abundance of varyingly sized vugs in the Grosmont Middle C unit. From bottom to top it's classified into three sub-units based on the vugs: large vugs, small vugs and disaggregated dolomite. The lowest sub-unit is defined as having large vugs with diameter greater than 0.5cm. These are thought to be a result of leaching of fossil burrows (Barrett & Hopkins 2010). Furthermore vug porosities are commonly connected by sub vertical cracks. The Upper Grosmont C unit is fine grained laminated dolomite grainstone containing small vugs <0.5cm diameter. This unit is considered reservoir facies with good intra-particle and inter-crystalline porosity. Separating the Upper Grosmont C sub-unit and the Grosmont D unit is approximately a 1m thick Grosmont C/D Marl.

The 30m thick Grosmont D unit is subdivided into three divisions: the 12 m thick Lower, 10m thick Middle and 8m thick Upper units. The Lower D is bitumen-saturated and very porous interval consisting of karst breccia with angular clasts enclosed in bitumen saturated fine disaggregated dolomitic crystals (Barrett and Hopkins, 2010). The Middle Grosmont D is commonly fractured and contains vugular porosity in the floatstone facies caused by leaching; it is noted that the bitumen saturation in this subunit is lower than in all other intervals (Barrett and Hopkins, 2010). Lastly, the Upper Grosmont D commonly contains a brecciated dolomite indistinguishable from the Lower Grosmont D sub-unit, however, it is a mainly clay free dolomite grainstone and is bitumen saturated.

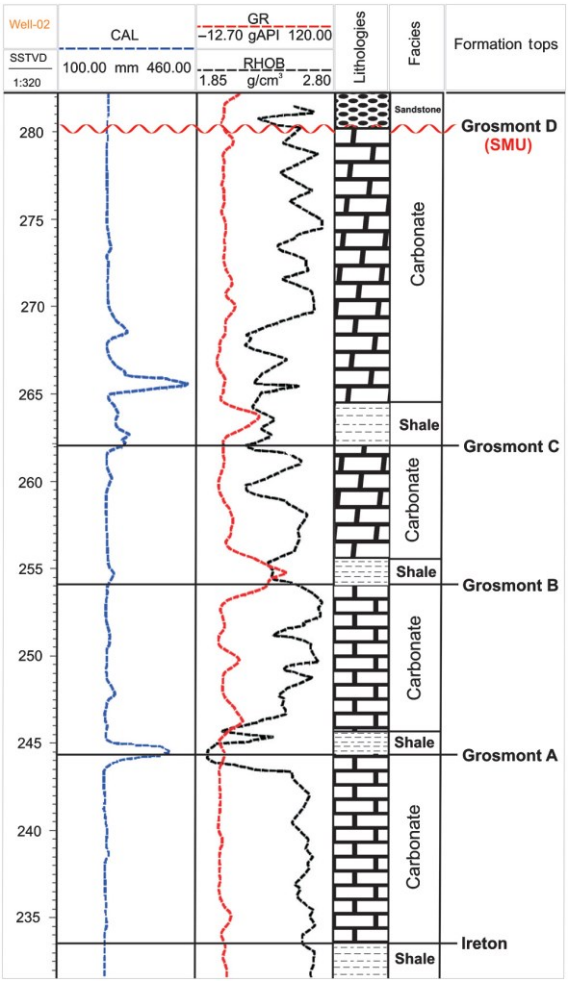

Figure 2.4: Typical log from the Grosmont Formation showing its interpretation based on gamma ray log signatures and highlighting the Grosmont A, B, C, and D. Shale units separate each of the carbonates and their higher natural radioactivity provide geological markers that are often called the Grosmont Shale Breaks. SMU refers to the SubManville Unconformity which is the major unconformity between the Paleozoic and Cretaceous sediments. From Fig. 4 of Ardakani et al., (2015) used by permission of the Society of Exploration Geophysicists under their fair use policy.

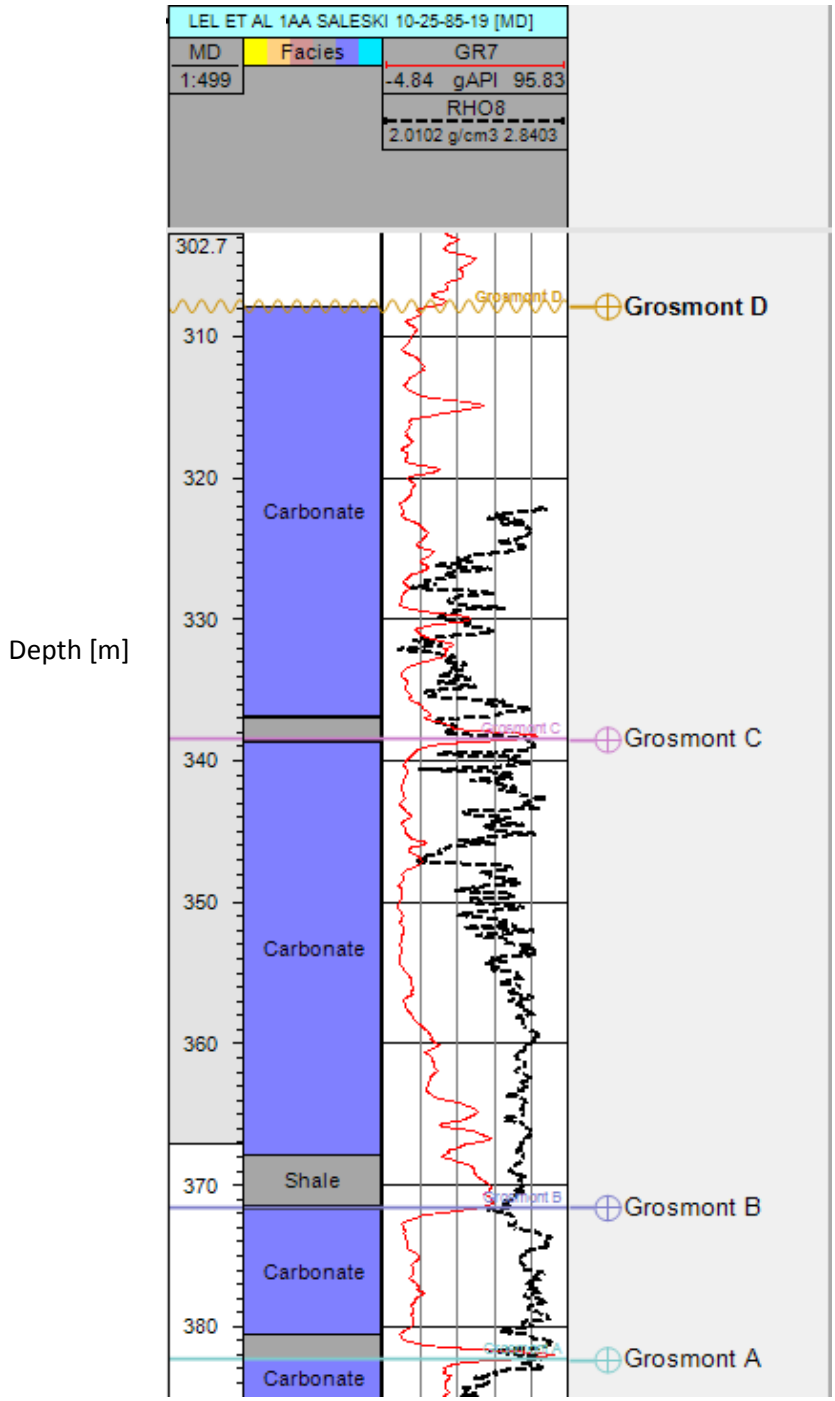

Figure 2.5: Grosmont well logs from the study area portraying characteristic shale breaks between formation tops. Above the red GR7 log is the gamma ray log while RHO8 is the bulk density well log. The high spikes in the gamma ray log show radioactive content contained in shales (data from Well 10-25-85-19W4).

Natural fractures are pervasive in the Grosmont reservoir and can range in length from centimetre to tens of metres. Natural fractures are seen on extracted core and in downhole data imagery. They can be sorted and analyzed by fracture depth, fracture dip, fracture spacing, and fracture density allowing statistical analysis to be performed on the naturally occurring fractures in this reservoir. Further, fractures can also be induced by the act of drilling, these provide information on the stress directions and may allow for some constraint of stress magnitudes. Natural fractures at the study site will be one of the main focuses of Chapter 4 while the relationship between the observed drilling induced fractures and in situ stress states is also discussed.

Natural fractures increase the effective permeability of a reservoir significantly. Indeed, their existence is key to whether a given reservoir may be economic and there has been a great deal of importance given to them. Surprisingly, there are few studies of joints and fractures available within the Western Canada Sedimentary Basin despite the importance of natural fractures to both reservoir productivity and in situ states of stress (e.g. Whitaker & Engelder 2005), there are surprisingly few public-domain studies of in situ fractures, faults, and joints in the Western Canada Sedimentary Basin. It is worth reviewing the literature that does exist, however.

Babcock (1973; 1974;1978) carried out an extensive field mapping program of outcrops in southern and central Alberta primarily in Cretaceous sediments and in the Devonian Waterways formation near Fort McMurray. Two systems of orthogonal joints existed in all of these areas. The predominant joint set, which he called System I, appears to be oriented approximately parallel and perpendicular to the trend of the Rocky Mountains with average strikes of 065° and 155° in southern Alberta (between latitudes 49° and 51°), strikes of 055° and 140° in central Alberta (between latitudes 51°N and 54°N), and 050° and 145° near Fort McMurray (about 57°N latitude). The less prevalent System II joint set strikes approximately N-S and E-W. A critical point is that nearly all of these joints are nearly vertically oriented. Scheidegger's (1983) statistical tests of Babcock's data sets confirmed the existence of the two joint Systems. To the southeast of the study area, Gendzwill and Stauffer (Gendzwll & Stauffer 1986) oriented over 7000 extensional joints at 16 outcrops localities in Saskatchewan, Montana, and North Dakota. They found two orthogonal joint sets striking on average at 049° and 139°, although variability in these directions did exist.

In coals, the natural fractures are referred to as cleats. Campbell (1979) also noted that the 'face cleats' (i.e. dominant fractures) in coal seams as measured in shallow mines across much of Alberta and into north east British Columbia also orient in the NE-SW direction. Indeed, this trend is so prevalent that Bell and Bachu (2003) replotted Campbell's data.

Under the presumption that modern day surficial features are related to underlying faults and fractures, these workers extended the outcrop information by searching for 'lineaments'. Babcock (1974) mapped 925 joints in outcrop in southern Alberta that showed mean strikes of 070° and 158°. The orientations of 4792 lineaments measured from air photos in the region averaged 052° and 158°; this relative agreement appears to suggest that the lineaments and the mapped outcrop joints were related. Babcock and Sheldon (1976) suggested that air photo lineaments and mapped joint systems (Babcock 1974) to the north of Fort McMurray were similarly related. Outside of the Fort McMurray area, however, Schiedegger (1983) disputed this relationship based again on his statistical analysis of the data. Stauffer and Gendzwill (1986) noted a correspondence between the mapped joint sets and the orientations of the rivers in their study area and suggested an underlying relationship on this basis. Misra et al (1991) interpreted satellite images of the Western Canada Sedimentary Basin between 48°N and 64°N finding lineaments that with predominant strikes of NE-SW and NW-SE that they attribute to the existence of vertical joint patterns. They associated higher lineament densities to known large scale structural elements of the basin such as the Sweet Grass and Peace River arches. Building on this work, Pana et al. (2001) carried out an extensive survey that searched for lineaments within northern Alberta in support of mineral exploration. They provided a number of lineament maps derived from inferred changes in facies or formation thicknesses in the sedimentary column (their Figure 6) and from satellite imagery and digital elevation mapping (their Figure 7) display the same NE-SW and NW-SE trends. The uniformity of these trends in lineament analysis seems remarkable, but it is difficult at this point in history to unambiguously associate such interpreted trends to actual in-situ fracture and joint systems.

Because fractures permeability overwhelms the rock matrix permeability, fractures have been studied in some detail in the Grosmont Formation. Wagner et al. (2010) briefly describe fractures in Shell's Grosmont lease seeming to indicate that most of them are bed-bound. Regrettably this

work has only been described in short abstracts and is difficult to incorporate such information most of which remains proprietary.

Machel et al (2012) note that generally the Grosmont is 'pervasively fractured'. They suggest that the fractures in the Grosmont Formation were formed in 3 or 4 different time periods referred to as F1 through F4. F1 fractures are of unknown age but must have existed before karsting, they may have been formed by differential compaction along the reef trends. F2 fractures are claimed to be pervasive throughout the Grosmont and are attributed to dissolution of the underlying Middle Devonian evaporates due to percolation of meteoritic water as part of the Late Jurassic – Early Cretaceous karst formation. Broughton (2013) also discusses fracture formation via dissolution. The F3 fractures are interpreted to result from tectonics and they have associated these with the trends found by Babcock (1973;1974). Presumably these result from to the bending of the lithosphere by crustal loading during formation of the Rocky Mountains as described earlier. The fractures in the Grosmont presumably resulted from extension over the forebuldge. Finally, F4 fractures are relatively recent and result from reactivation of the earlier F1-F3 fractures during the many cycles of glacial loading and unloading during the Quaternary. Machel et al (2012) do not discuss, however, the orientations of these various fracture sets.

Over the study area MacNeil (2015) indicated that the Grosmont C and D are 'variably to intensely fractured'. He found fracture families that ranged from horizontal bed-bound sets to large aperture, steeply-dipping fractures that cross multiple units. He suggested that the apertures of these fractures from < 1mm to < 20 mm were enlarged by dissolution. Most interestingly, these fractures are mostly bitumen saturated except in the uppermost D near the unconformity where water and clays can reside. Yang et al, (2014) show a rose diagram of the observed fracture dips provided by consultants from the same image logs, but it is not clear that the difference between drilling induced and natural fractures had been properly accounted for. In this thesis we will update these data by analysis of the extensive set of image logs provided.

Figure 2.6: Core photo from well 4-16-85-19W4 at depth 418.05-419.00m. Core shows vugs, fracturing and bitumen staining.

Figure 2.7: Core photo from well 7-20-85-19W4 at depth 424.25-425.00m. Core shows fracturing and vuggy porosity with bitumen staining.

2.2. Basic Theory for Stress Analysis

This project is a unique opportunity to focus more on the understanding of the geomechanical aspects of the reservoir. The study is unique in that the abundance of wells and image logs in a small study area allow for a rare chance for analysis of the natural and drilling induced fracturing of the reservoir and therefore a study of the regional and local stresses in place. As the Grosmont deposit is shown to have high values of porosity, saturation and permeability (Buschkuehle et al. 2007) solidifying its potential as a prospective reservoir and as stress directions and relative magnitudes of stress are more than useful in hydrocarbon recovery methods in a number of situations (Bell & Babcock 1986), this stress study may be useful for well project planning and in-situ methods for hydrocarbon recovery.

In this section, we review the basic theories and definitions related to the determination of crustal stress. This is preparatory to the stress analysis carried out in Chapter 4.

Simply put, stress is defined as the ratio of force per unit area; it is measured in Pascals [$Pa = N/m^2$]. Stress can also be thought of as an expression of internal forces that adjacent particles exert on each other. Elastic deformation is governed by Hooke's Law and can be illustrated by considering a rod of length x with cross sectional area A that is extended by a small amount δx due to an applied force F. The extensional increase in length $\frac{\delta x}{x}$ is proportional to the applied force and inversely proportional to the cross-sectional area:

$$\frac{\delta x}{x} \propto \frac{F}{A}. \qquad (2.1)$$

Taking the limit as the cross-sectional area becomes infinitesimal is the stress σ:

$$\sigma = \lim_{A \to 0} \left(\frac{F}{A}\right). \qquad (2.2)$$

Consider a hypothetical small rectangular cube with sides of area *A* that has forces acting on it. If we consider one of the sides *A* of the cube, two types of stresses can be defined: those that act perpendicular to the area, denoted by σ_{ij}, and those that act parallel to the area, denoted by τ_{ij}. In a right-handed coordinate system with principle axes *x, y,* and *z,* the subscripts *i* and *j* denote the direction of the normal of the plane on which the stress acts and the direction it acts in respectively. This defines a second order Cauchy stress tensor that can be written as

$$\sigma_{ij} = \begin{matrix} \sigma_{xx} & \tau_{xy} & \tau_{xz} \\ \tau_{yx} & \sigma_{yy} & \tau_{yz} \\ \tau_{zx} & \tau_{zy} & \sigma_{zz} \end{matrix}. \qquad (2.3)$$

It can be shown that the stress tensor is symmetric ($\tau_{xy} = \tau_{yx}; \tau_{yz} = \tau_{zy};\ \tau_{zx} = \tau_{xz}$) and therefore the 9 stress components of the stress tensor reduce to 6 unique components. To expound on this symmetry briefly, consider a cube of material at rest, and therefore in equilibrium, with shear stresses acting on each face. In order for the cube to satisfy the principle of conservation of angular momentum (ie: not move), τ_{xy} must equal τ_{yx} and likewise for the other shear stresses. Stresses acting perpendicular to the sides *A* ($\sigma_{xx}, \sigma_{yy}, \sigma_{zz}$) are called normal stresses while stresses acting parallel to *A* ($\tau_{xy}, \tau_{yz}, \tau_{xz}$) are called shear stresses (Figure 2.8). First, note that in the usual convention for Earth science, compressional stress is taken to be positive because environmental stresses such as burial at depth, confining pressure, fluid pressure in pores, are always compressive. Further, there exists a set of coordinate axes rotated from the principle axes where the shear stresses reduce to 0. These axes are defined as the principal axes of stress and the normal stresses associated with them are called principal stresses. The principal stresses are denoted in order of descending magnitude as σ_1, σ_2 and σ_3 with $\sigma_1 > \sigma_2 > \sigma_3$.

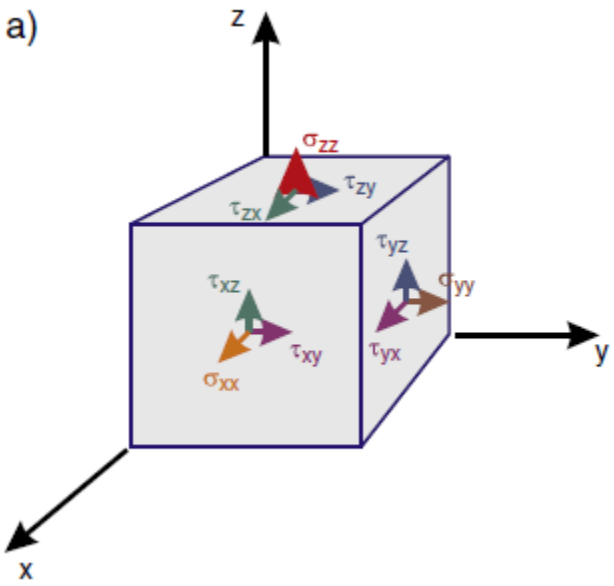

Figure 2.8: Hypothetical cube of material in the Earth with infinitesimally small forces acting on it. The first stress subscript denotes the normal of the plane in which the force is acting and the second subscript denotes the direction in which the force acts. Figure 1a) reproduced from Crustal stress determination from boreholes and rock cores: Fundamental principles by Schmitt et al, 2012 with permission to reprint granted from Elsevier.

2.3. Stress in the Earth

The state of stress in the Earth's crust in commonly described in terms of the three principal stresses ($\sigma_1, \sigma_2, \sigma_3$). Historically when considering the formation of geological features formed by stress such as faulting, a system of forces that has existed in geological time has to be considered (Anderson 1951). In tectonically active regions with earthquakes, faulting is produced by these tectonic forces that continue to produce and grow faults even today. It may be shown mathematically that stresses acting within the rock at a time of equilibrium can be resolved into three principle stresses acting at right angles to each other (Anderson 1905).

In areas of subtle topography (such as the study site) the three principal axes of stress in the upper crust of the earth are assumed to be oriented horizontally and vertically (Zoback et al. 1989). This is designated as a "free-surface" as the top boundary of the topographic surface is in contact with the Earth's atmosphere. If the topography is sufficiently subtle, then one of the principal stresses must be aligned vertically; it is usually denoted S_V. Furthermore, absolute stress magnitudes are very difficult to obtain in-situ in the Earth's crust; however, relative stress magnitudes can be obtained from the stress features and style of faulting deformation in the region. A consolidation

of in-situ stress orientation indicator data has been collected by the World Stress Map (WSM) project as well as establishing a quality ranking system to facilitate the comparison between multiple regions (Tingay et al. 2008).

When considering stress fields in the Earth, it's common to assume that one of the principal stresses is vertical (denoted S_v) because, in addition to the free surface argument above, at an arbitrary point inside the Earth's crust there will be compressive stress generated by the overlying rock with gravity acting downwards (see McGarr & Gay 1978). The vertical stress can be calculated by integrating the product of gravity g with the density *ρ(z)* of the overlying rocks with depth *z:*

$$S_v(z) = \int_0^z \rho(z) g \, dz \, . \qquad (2.4)$$

Furthermore, the vertical stress can be relatively easily obtained if the densities are known above the point of investigation. These densities are usually obtained by a standard bulk density borehole logs.

It follows that the remaining two principal stresses found in the Earth are directed horizontally. The two horizontal principal stresses are denoted S_H and S_h, with $S_H > S_h$. These two principal stresses represent the greatest and least horizontal compressive stresses and are aligned with the principle axes. However, the magnitudes of the two horizontal stresses are not so easily obtained. For example, horizontal stresses can result from combinations of tectonic stresses such as plate-boundary forces, geodynamic process forces, effects of topography or inhomogeneous density distributions (Zoback et al. 1989).

Anderson (1951) proposed that faulting regimes could be classified based on various combinations of the Earth's principal stresses and moreover that the relative magnitudes of these stresses control the motion of faulting in the Earth. The three combinations he proposed as reference states are (Figure 2.9)

- Extensional faulting regime (normal faulting): $S_v > S_H > S_h$
- Thrust faulting regime (reverse faulting): $S_H > S_h > S_v$
- Strike slip faulting regime: $S_H > S_v > S_h$.

Here we focus on the state of stress in the crust in the Western Canada Sedimentary Basin. The review here will demonstrate that while we appear to know the stress directions within the WCSB quite well, there is currently little understanding past this. Faulting environments remain essentially unknown although, as will be seen, it is likely in many cases that S_V cannot be the greatest compression.

To our knowledge the state of stress in the WCSB was completely unknown until the late 1970's. (Bell & Gough 1979) first suggested that remarkably consistently-oriented borehole elongations observed by Cox (1970) and later by Babcock (1978) using an dual-caliper logging tool (i.e. dipmeter) result from failure of the borehole wall rock because of the amplification of the virgin stresses by the borehole as will be discussed in detail later. The elongations, or breakouts, were strongly oriented at opposing azimuths around the borehole of 137° and 317° suggesting to them an anisotropic state of horizontal stress with S_H trending NE-SW and S_h trending NW-SE. They further reasoned that $\sigma_1 \neq S_v$ because if this was the case it was not thought likely that the horizontal stresses could be sufficiently large to overcome the rock strength at depths of about 1 km. This leaves either strike-slip or thrust faulting environments as possibilities but they could not without additional information say which exists.

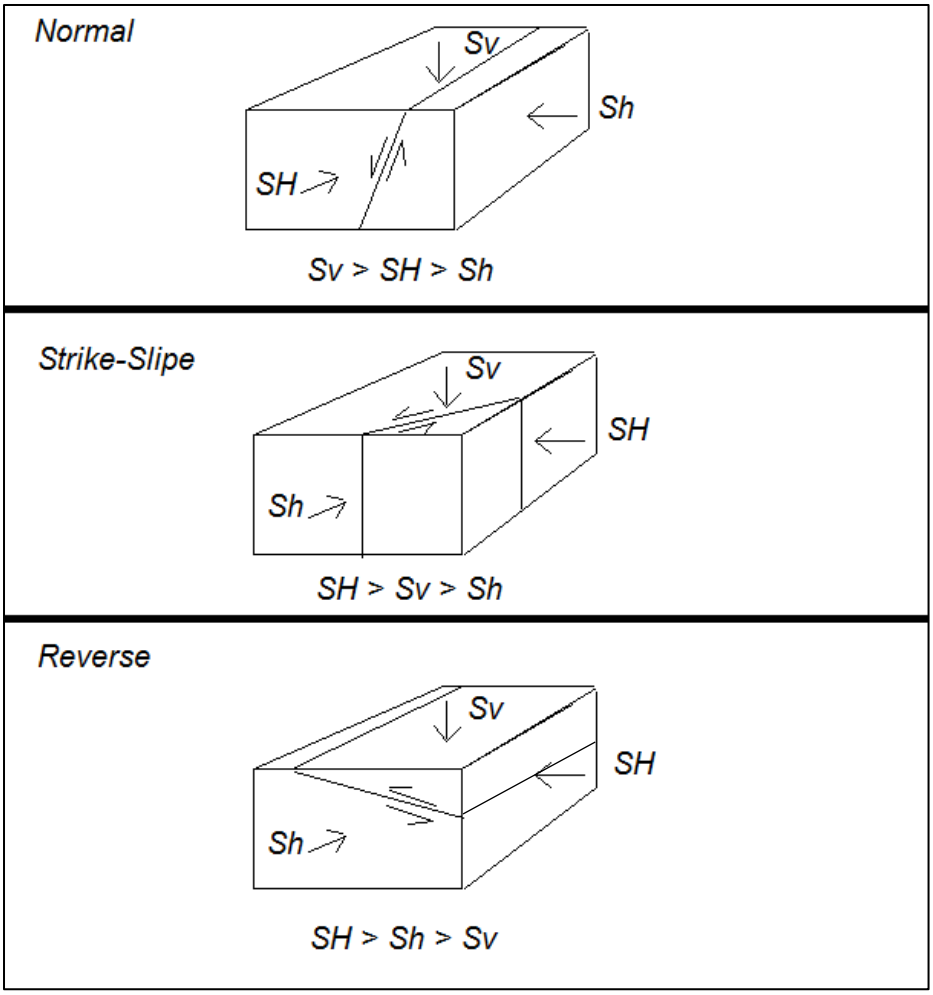

Figure 2.9: An illustration showing the Anderson Faulting regimes

These studies were further amplified in Gough and Bell (1982) and Fordjor et al. (1983). Gough and Bell (1980) added additional new breakout data. They made two further observations that may help constrain the faulting environment. In the Pembina oil field industry observers had commented that water flooding enhanced first oil productivity but then early water breakthroughs along a NE-SW trend. Gough and Bell (1980) suggested that this was due to vertical hydraulically induced fractures oriented in this direction that served as efficient pathways for fluid motions. Similarly, in the Cold Lake heavy oil reservoir, highly pressurized steam appeared to have created vertical fractures also running NE-SW (see also comments by Dusseault (1977)). These two points indicate a strike-slip environment for the simple fact that one would expect induced fractures to propagate in the horizontal plane if σ_3 was equal instead to S_v.

Fordjor et al (1983) added more new data from breakouts (Figure 2.10) and were able to incorporate some quantitative measures of stress from hydraulic fracturing stimulations. They also noted anomalous breakout directions between latitudes 55°N and 56.5°N that are rotated to point nearly E-W, they suggested this may be due to the existence of the Peace River Arch. They were also able to extract from the literature quantitative estimates of the horizontal stress magnitudes using values obtained during construction of a mine shaft in southern Alberta to 235 m depth (Kaiser, 1982), and from hydraulic fracturing stress measurements around the Province ((Mcleod 1979), (Wyman & Hunter 1980), (Hassan 1982) and (Gronseth & Kry 1983)) that further suggested that a strike-slip faulting environment predominates (see their Table 4 for locales).

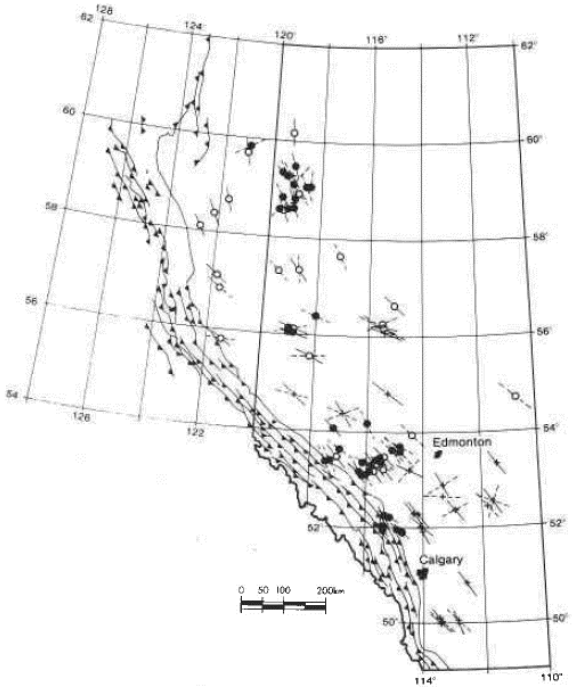

Figure 2.10: Summary of 94 breakout orientations compiled by Fjordor et al, (1983) from their work ●, from Gough and Bell (1981) ○, and from Babcock (1978) +. Note anomalous stress directions centred near 55°N. Reproduced from Figure 4 of Fjordor et al, (1983) © 2008 Canadian Science Publishing or its licensors. Reproduced with permission from NRC Research press

Bell's (Bell & Babcock 1986) analysis of the Western Canadian Basin suggests the stress regimes from surface to approximately 350m depth $S_H > S_h > S_v$, from 350m to 2500m $S_H > S_v > S_h$ and below 2500m $S_v > S_H > S_h$. They also conclude that the maximum horizontal stress is oriented NE-SW propagating perpendicular to the strike of the Rocky Mountain orogeny (Figure 2.10).

Bell et al (1994) provided a further updated summary of the knowledge of the state of stress in the WCSB. They were able to obtain additional quantitative measures of stress magnitudes from micro-fracturing measurements listed in their Table 29.1 as reported by Proskin et al, (1990a; 1990b), Settari and Rasibeck (1978), Leschcyshyn and Seyer (1990), Holzhausen et al (1980), Talebi et al (1991), and McLellan (1986a; 1986b). Care was taken to exclude hydraulic fracturing measurements that were carried out in producing reservoirs as the values are disturbed from the virgin state by changes in the pore pressure (Bell & Woodland, 1989). These data, too, appear to indicate that the WCSB is generally subject to strike slip conditions at least above 2.5 km depth (Figure 2.11). It must be noted, however, that estimates of S_H can be highly suspect (e.g., Schmitt and Zoback, (1989; 1993), Schmitt and Haimson (2016)) and it is not clear that $S_H < S_V$ from the sparse set of measurements shown in Figure 2.11 whether it is reasonable to assume that the faulting environment changes at depth.

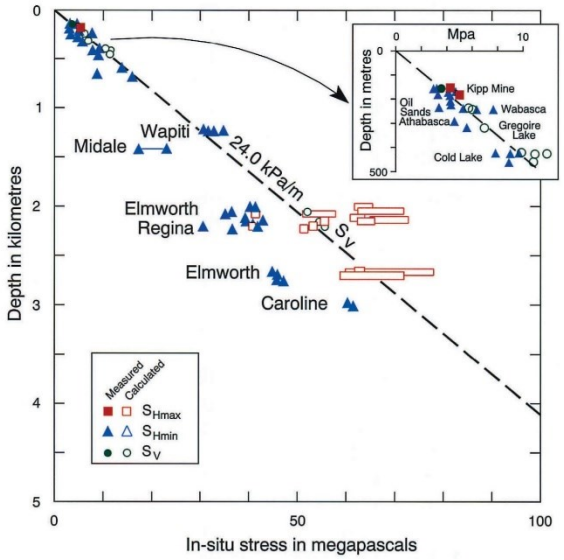

Figure 2.11: Summary of quantitative stress values obained from overcoring in the Kipp Mine and micro-fracing stress measurements in various reservoirs in the WCSB. Reproduced from Bell et al, 1994. Permission to reproduce for educational purposes given by Alberta Energy Regulator.

Subsequent to Bell et al (1994), Bell continued construction of a data base of information by including select pressures for leak off tests and from fracture breakdown pressures. It must be noted that the values of stress obtained from these can be highly suspect and must be carefully selected. A leak off test is generally required to ensure the competence of a cemented casing with open hole at the bottom. In this test the wellbore is pressurized to a set value to ensure that this pressure can be held, if a fracture is produced fluid is said to 'leak off' into the formation. The

pressure at which this leak off begins could in some cases be indicative of the magnitude of S_h. Fracture breakdown pressures are the peak pressures that are recorded during a massive hydraulic fracture stimulation.

After providing the known caveats as to the quality of a stress measurement from a leak off test or a massive hydraulic fracturing breakdown, care were taken to attempt to include some of these data in order to infer stresses in the WCSB and these results were first reported in Bell and Bachu (2003) with a recent update in Bell and Grasby (2012). These two studies focussed on coal bed methane and geothermal potentials, respectively. These contributions include maps of the estimated vertical stress magnitudes at the tops of select formations or of stress gradients. The use of stress gradients (in kPa/m) is common in the petroleum industry because 1) it allows workers to make a rapid assessment as to what the stress would be at their depth of interest, and 2) most often workers will have only 1 data point at 1 depth from which to base their extrapolation. Workers must remember however that this may not in fact be the case and variations in the mechanical properties could result in stress concentrations within stiffer formations that would make the use of a single number in a stress gradient questionable in some cases.

Using the relatively large data base of micro-fracture (the most reliable), mini-fracturing, and leak off testing, contour maps of S_h gradients were developed (e.g. Figure 2.12). There still remains a fair degree of scatter within this data set. Aside from the issue of incorporating lower quality leak off and breakdown pressures, other issues that can cause problems are the fact that certain geological intervals can concentrate stresses. This information is difficult to incorporate, however, and although there are potential issues with rapid changes in gradient this map does highlight that 1) the actual data available remains sparse, and 2) it would be important to attempt in a more systematic way to collect careful stress measurements around the basin.

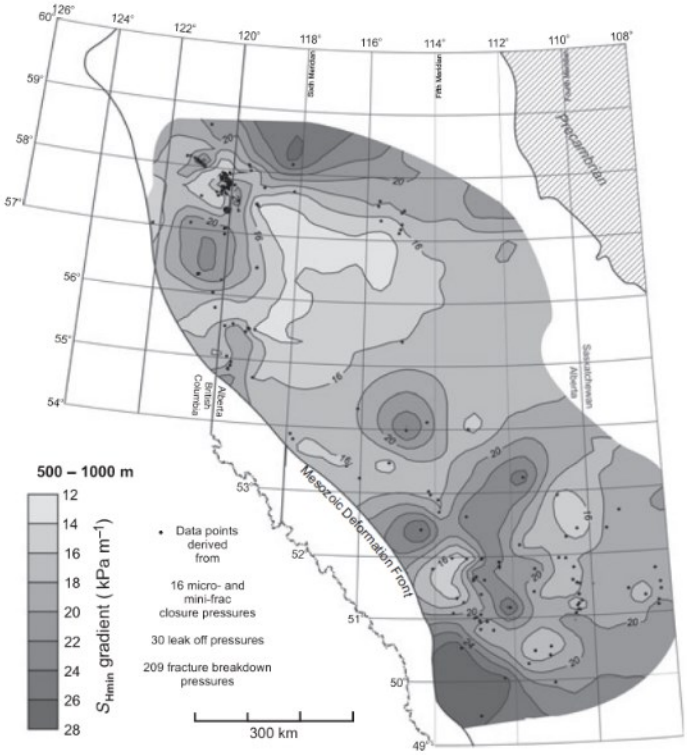

Figure 2.12: Bell and Grasby's (2012) inferred map of S_h gradients over the WCSB as determined by select hydraulic fracturing closure pressures and adjusted leak off tests and fracture breakdown pressures for tests from 1000 m to 500 m depth. Reproduction of Figure 12 of Bell and Grasby (2012) permission to use granted by John Wiley and Sons © 2011 Blackwell Blackwell Publishing Ltd, Geofluids,12,150-165.

There is a limited amount of additional data within the WCSB outside of Bell's compilations. Hamid (2008) focussed on issues related to coal bed methane production within Saskatchewan. He compiled a S_V map using over 250 density logs. They attempted to estimate S_h from analysis of confidential fracture stimulation pressure records of hydraulic fracture stimulations within the Viking Formation from a final set of 106 wells. They developed a post-fracture shut-in analysis to extract values of both fracture closure pressure and instantaneous shut in pressure, both of which provide estimates of S_h. They found that in all cases $S_h < S_V$ suggesting that in this area the state of stress is either in a strike slip or thrust fault environment.

Micheal and Buschkuehle (2007) carried out an assessment of the geological safety of the reinjection of acid-gas (i.e. containing poisonous H_2S) back into depleted or producing reservoirs in the Peace River region. A part of their study focussed on estimating the in situ stress. They

used mini-frac and hydraulic fracturing data within local Cretaceous and Jurassic formations to estimate the fracture gradient pressure (i.e. the gradient expected for S_h). The data points range in depth from nearly 2600 m to 880 m providing gradients between 12.1 to 20.5 kPa/m that was smaller than there estimated 23.5 kPa/m for the vertical stress gradient. Regrettably, they do not report how these values are obtained. They also provide the orientations of breakouts in 25 boreholes from which they suggest that S_h is directed between 102.7° and 146.8° with an average of 124.5°. Again, there is no discussion of what kinds of well log data were interpreted.

Hawkes et al (2005) attempt to analyze a large number of leak off tests and hydraulic fracturing records as part of an analysis for the safety of CO_2 sequestration. The analysis attempted to find lower bound envelopes for S_h from interpretation of the pressurization curves. They note that the leak off tests are usually carried out in the open hole beneath the casing shoe in non-reservoir rock that should retain is virgin pore pressure. Alternatively, the hydraulic fracture stimulations are often conducted to enhance production from older reservoirs in which the pore pressure has declined, it is expected that these lower pore pressures will affect the hydraulic fracturing breakdown process. At shallow depths they found that a gradient of 17 kPa/m provided a good lower bound to the leak off pressures. This gradient evolved to only 13 kPa/m in deeper reservoirs possibly because of prior production. They applied these analyses to the sites of acid-gas injection arriving at an average gradients of 16.6 kPa/m and 23.8 kPa/m for S_H and S_V, respectively. They further suggested that $S_h < S_H < S_V$ (normal faulting environment) but did not provide the rationale for this assumption. They did note, however, the weaknesses of this analysis and recommended that proper hydraulic transient testing be carried out.

There have been two additional studies provided and these are briefly noted. Teichrob et al. (2010) analyzed geophysical log data from two unidentified boreholes near 55°N and 118.5°W. Analysis of oriented caliper data gave mean breakout azimuths of 124.3° ± 8.1° in agreement with the earlier observations described above. Urban and Aguilera (2015) applied long-standing, but still untested, empirical petrophysical relationships to estimate in situ pore pressures and stresses.

Most recently, Reiter et al., (2014) combined the Bell's previously compiled but unpublished data (Bell and Bachu (2003), Bell and Grasby (2012)) as well as some other recent studies (e.g. Hamid (2008)) to update 78 records and add 142 records from Alberta to the World Stress Map. These new data confirm (Figure 2.13) a pattern of north-east directed horizontal stress orientation away

from the Rocky Mountain orogenic belt. The median S_H direction is noted as highly uniform with some subtle deviations of only a few degrees in the S_H azimuth in the south-west except for some in the vicinity of the Peace River Arch. Reiter el al (2014) further extended this analysis to show that the stress directions are not necessarily perpendicular to the Cordillera and suggested on this basis that deeper underlying mechanisms may control the stress field.

Returning to Fig. 2.13, it is important to note the paucity of data in the vicinity of the study area. As such, the current study will be able to add new stress information to the existing data bases.

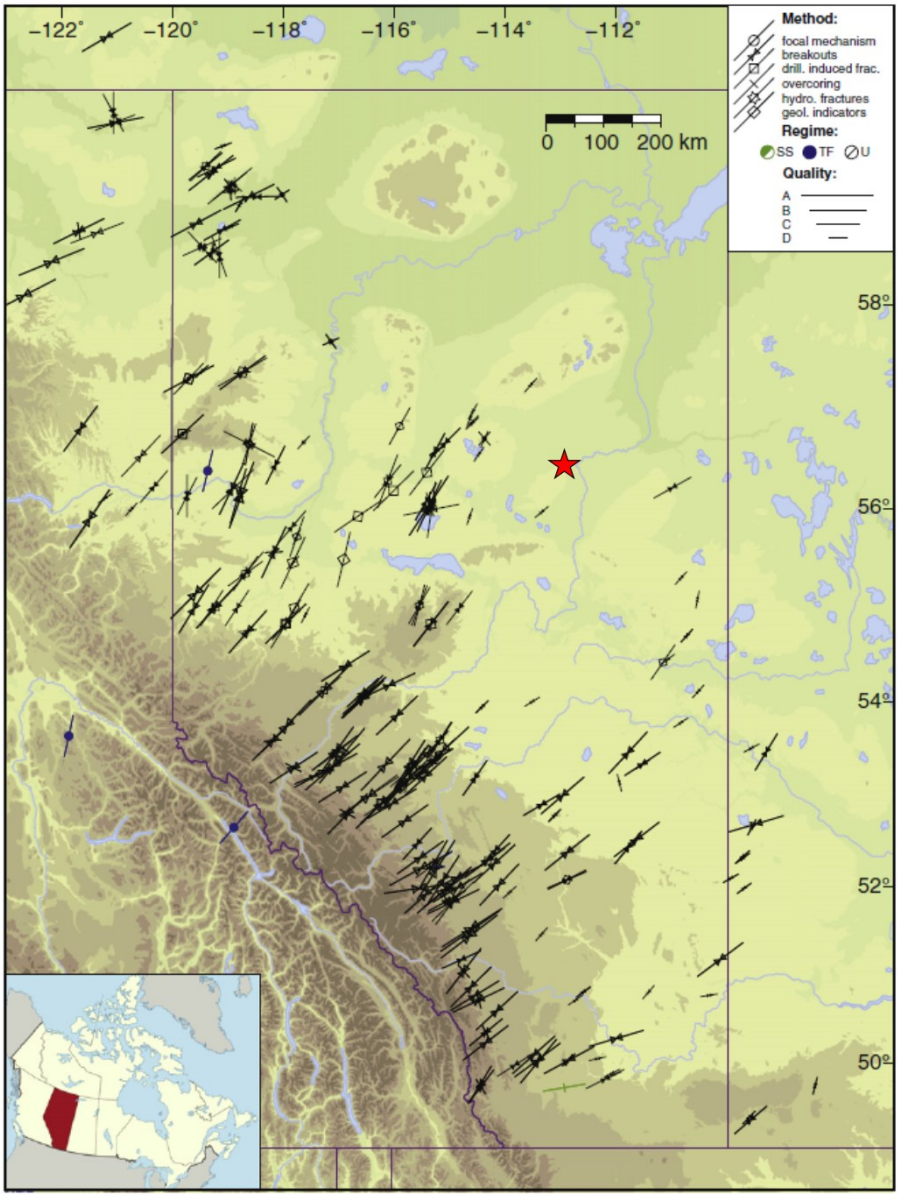

Figure 2.13: Recent stress map of Alberta adapted from Reiter et al. (2014). Lines indicate direction of maximum horizontal compression. Location of the Saleski pilot project indicated by red star. Permission to use granted by Elsevier.

2.4. Concentration of Stresses at the Borehole and Failure Mechanisms

At this point it's important to explore and focus on the stress components at the borehole wall because as the aforementioned Anderson Faulting regimes (Figure 2.9) can yield qualitative relative rankings of the principal stresses, similar results can be derived from stress features seen during borehole image logging.

Once a borehole cavity is created in the Earth, the pre-existing stresses are concentrated around the borehole. The rock surrounding the borehole must now support the stress that was previously held by the removed material. The stability of boreholes has been an important subject for producing and drilling boreholes. Numerous complications can arise during the drilling process such as enlargement of the borehole, borehole collapse, loss of circulation of borehole fluid and these can lead to other issues like poor cement displacement (Aadnoy & Chenevert 1987).

In a discussion of stresses it is important to consider rock strength. Usually there are two kinds of strengths that can be defined: tensile and compressive shear. The tensile strength is the point at which a rock fails when pulled in tension. Rocks are thought to have an unusually weak tensile strength compared to other materials because a portion of their pores are crack-like; consequently it is common for authors to assume that rocks have a zero tensile strength (Aadnoy & Bell 1998, Aadnoy & Chenevert 1987). In this thesis we assume that the tensile strength to be zero unless stated otherwise for comparison purposes. Another basic assumption is that the borehole materials are homogeneous and isotropic which behave in a linear elastic way. The reasoning behind this assumption is that once a rock has failed along a crack or flaw, failure will continue to propagate in that direction. Aadnoy and Chenevet (Aadnoy & Chenevert 1987) have shown that the main cause of wellbore failure is tensile failure axially along the borehole while the radial and hoop stresses persist in a state of compression. However, shear effects and failure arise from the large stress differences between the circumferential and radial stresses.

Local borehole stress concentrations can cause the borehole to fail. Kirsch (1898) described the plain strain case for stresses acting around a circular hole in an infinite plate with a principal stress, S_H, acting on it. Considering a borehole of radius a for a point at distance of r to the borehole center axis and at azimuth θ measured relative to the maximum principal stress and therefore x-axis, the hoop stress $\sigma_{\theta\theta}$, radial stress σ_{rr} and shear stress $\tau_{\mathrm{r}\theta}$ take the solution in the polar coordinate form (r,θ):

$$\sigma_{\theta\theta} = \frac{S_H}{2}\left(1 + \frac{a^2}{r^2}\right) - \frac{S_H}{2}\left(1 + \frac{3a^4}{r^4}\right)\cos(2\theta) \qquad (2.5)$$

$$\sigma_{\mathrm{rr}} = \frac{S_H}{2}\left(1 - \frac{a^2}{r^2}\right) + \frac{S_H}{2}\left(1 + \frac{3a^4}{r^4} - \frac{4a^2}{r^2}\right)\cos(2\theta) \qquad (2.6)$$

$$\tau_{\theta\mathrm{r}} = -\frac{S_H}{2}\left(1 - \frac{3a^4}{r^4} + \frac{2a^2}{r^2}\right)\sin(2\theta). \qquad (2.7)$$

If we consider S_H being a compressional stress, as is mainly the case in the Earth, a number of interesting cases arise. At a point on the borehole wall in the direction of S_H (ie: $\theta = 0$ and $180°$), the hoop stress will be in a state of tension: $\sigma_{\theta\theta} = -S_{\mathrm{H}}$. However, perpendicular to the direction of S_H (ie: $\theta = 90°$ and $270°$), the hoop stress is amplified in compression: $\sigma_{\theta\theta} = 3S_{\mathrm{H}}$.

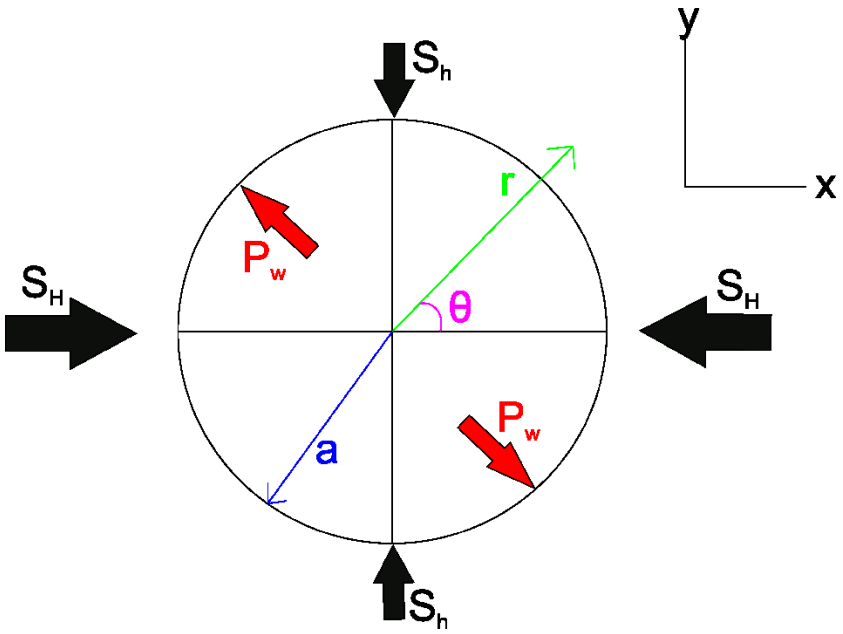

Figure 2.14: Diagram of borehole geometry for stress concentrations. Diagram is oriented along axis of the borehole. S_H and S_h are the maximum and minimum horizontal stresses respectively. P_w is the wellbore pressure caused by the mud weight.

As we will be dealing with rock failure, we must also consider the effects of pore pressure and the concept of effective pressure. The differential, or Terzhaghi, effective stress law states that the effective stress

$$\sigma_{ij}^{eff} = \sigma_{ij} - \delta_{ij} P_p \qquad (2.8)$$

where δ_{ij} is here a total stress, P_P is the pore pressure, and δ_{ij} is the Kronecker's delta with $\delta_{ij} = 1$ if $i = j$ (i.e. for normal stresses) and $\delta_{ij} = 0$ if $i \neq j$ (i.e., for shear stresses). The importance of this is that a physical property (e.g. seismic wave speed or electrical conductivity) will remain constant if the effective stress σ_{ij}^{eff} does not change. That is, if both P_P and σ_{ij} increase or decrease by the same amount then σ_{ij}^{eff} remains constant and the physical properties will not change. This will become important for dealing with rock failure.

There are two main modes of brittle failure: compressive shear and tensile. With regards to the latter, tensile failure occurs when the rock is pulled apart by tensile stresses (that here would have negative sign). Tensile stresses are actually difficult to generate within the earth where we expect all of the stresses to be compressive. However, they can exist as part of the stress concentration around a cavity as indicated above. The tensile failure criteria essentially states that a rock failures in tension once the normal stress exceeds a critical value T (>0) called the tensile strength according to:

$$\sigma - P_p < -T \qquad (2.9)$$

which incorporates the effective stress law. This shows that the existence of a pore pressure promotes failure of the rock, and the pore pressure cannot be ignored. Rock is very weak in tension primarily due to the nearly pervasive existence of microcracks. Perras and Diedeichs (2014) have recently provided a comprehensive review of the measurement of rock tensile strength including an extensive compilation of strength values from the literature. They provide a value from a direct tensile test on a dolomite of T = 5.7 MPa and a limestone of T = 7.1 MPa. One must take great care, however, in applying such values generally. Knowing what value of T to use will be important in later Chapters as it will influence the estimates of the magnitudes of the in situ stresses.

The other major brittle failure mode is compressional shear failure. Shear failure can occur if the borehole is under-pressured and can spall and collapse. Compressive shear failure is usually described with the rock failure criteria developed from the Mohr-Coloumb frictional failure theory. Its most easily represented as a diagram with the normal stress along the horizontal axis and shear stress along the vertical axis, it is a graphical illustration of the state of stress leading to failure (Figure 2.15). In laboratory testing, multiple samples are put under varying principal stresses until failure and combining these data forms a series of circles describing the conditions in which caused the rock to fail. Combining these data points forms an envelope of failure essentially describing the allowable stress states for the sample type. What is commonly used is a linearized version of this envelope. With reference to Figure 2.15, the Mohr-Coulomb linearized frictional failure criteria states that shear failure occurs if the state of stress, here given as the maximum and minimum compressions σ_1 and σ_3, respectively,

$$\tau = \sigma\mu + C\ . \qquad (2.10)$$

Where above, τ and σ are respectively the shear and normal stresses acting on a plane whose normal is at an angle β from the direction of σ_1; and consequently this shear failure plane will be oriented at an angle $\pi/2 - \beta$ from σ_1. The angle ϕ is called the friction angle and the coefficient of internal friction is $\mu = tan(\phi)$. The two angles are related to one another through $\beta = \pi/4 + \phi/2$. C is the cohesion (i.e. the inherent shear strength of the material) that is not easily determined experimentally. The coefficient of internal friction, by defining the slope in equation *(2.10)*, controls the strength (i.e. the value of σ_1 at which the rock will fail in shear) with lateral confining stress σ_3. It is this type of rock failure that Bell and Gough (1979) first hypothesized was responsible for the formation of borehole breakouts.

As just indicated, the cohesion C is not so easily found in the laboratory. Instead, workers often measure the unconfined compressive strength (UCS) by simply applying an axial load σ_1 to the sample with no lateral load being applied (i.e., $\sigma_3 = 0$). It can be shown from the geometry of Figure 2.15 that $UCS = 2C[(\mu^2 + 1)^{1/2} + \mu]$.

It will turn out convenient later to rewrite the failure criteria (see section 4.6 of Jaeger and Cook (Jaeger & Cook 1976)) in terms of σ_i and σ_3,

$$\sigma_1 = UCS + \sigma_3\left[\left(\mu^2 + 1\right)^{1/2} + \mu\right]^2 \qquad (2.11)$$

that may also be rewritten as ((Walton et al. 2014))

$$\sigma_1 = \frac{2C\cos(\phi)}{1-\sin(\phi)} + \sigma_3\frac{1+\sin(\phi)}{1-\sin(\phi)} \qquad (2.12)$$

that is the form applied later in Chapter 4.

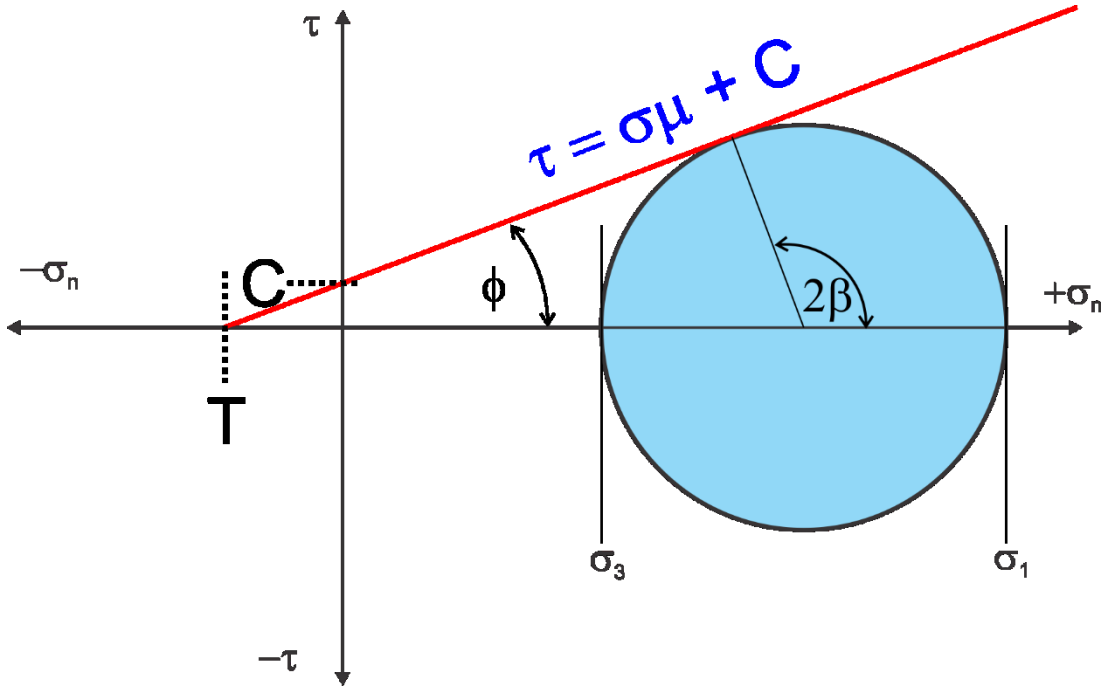

Figure 2.15: An empirically derived linearized Mohr-Coloumb diagram from lab measurements using a tri-axial test in which 2 of the principal stresses are controlled and the uniaxial normal stress is raised until rock failure. The Mohr-Coloumb envelop is shown in red and each of the circles is derived from a sample. The cohesion, C, is given by the vertical intercept and the coefficient of internal friction, μ, is given by the slope of the envelope.

Natural fractures have already been discussed above; they existed in the earth before the borehole was drilled. However, fractures can also be introduced to the borehole by the pressurization of the borehole wall during the drilling process. This puts the hoop stress in a state of tension.

The stress concentrations present at the borehole are functions of the borehole pressure produced by the drilling mud pushing outward on the borehole wall and the far field principal stresses in the crust. The borehole pressure is always a principal stress as it acts perpendicularly to the borehole wall in all cases. In the case of deviated boreholes, directional transformations are used to remedy the coordinate discrepancy between the in-situ stresses and borehole direction (see the analytic solutions in Schmitt et al. 2012). In this thesis the boreholes are vertical and we assume their axis is aligned with the principal vertical stress S_V; consequently the equations above will suffice for our analysis.

The 2D Kirsch equations (*2.5)-(2.7*) are derived from plane strain conditions and describe stress. If there are two orthogonal principal stresses S_H and S_h, superposing their stress concentrations gives:

$$\sigma_{\theta\theta} = \frac{S_H + S_h}{2}\left(1 + \frac{a^2}{r^2}\right) - \frac{S_H - S_h}{2}\left(1 + \frac{3a^4}{r^4}\right)\cos(2\theta) - P_w\frac{a^2}{r^2} \quad (2.13)$$

$$\sigma_{rr} = \frac{S_H + S_h}{2}\left(1 - \frac{a^2}{r^2}\right) + \frac{S_H - S_h}{2}\left(1 + \frac{3a^4}{r^4} - \frac{4a^2}{r^2}\right)\cos(2\theta) + P_w\frac{a^2}{r^2} \quad (2.14)$$

$$\tau_{\theta r} = -\frac{S_H - S_h}{2}\left(1 - \frac{3a^4}{r^4} + \frac{2a^2}{r^2}\right)\sin(2\theta) \quad (2.15)$$

Where above $\sigma_{\theta\theta}$ is the tangential hoop normal stress, σ_{rr} is the radial normal stress, τ_{xy} is the shear stress, a is the borehole radius, r is the distance from the borehole axis, θ is the azimuth measured from the x-axis. By definition the magnitudes of $S_H > S_h$. To investigate compressive and tensile concentrations and failure at the borehole wall in a stressed rock mass, we examine where the hoop stress is at maximum and at minimum. These occur at the azimuthal angles $\theta = 0°$ and $90°$ with a = r (i.e. at the borehole wall). These simplify the borehole centric stress equations into 2 cases:

$$\sigma_{\theta\theta,0} = 3S_h - S_H - P_w \quad (2.16)$$

and

$$\sigma_{\theta\theta,90} = 3S_H - S_h - P_w\,, \quad (2.17)$$

with

$$\sigma_{rr} = P_w\,. \quad (2.18)$$

The radial stress is a result of the drilling mud weight P_w pushing outwards on the borehole wall. At $\theta = 0°$, if the tangential stress $\sigma_{\theta\theta}$ is less than the rock tensile strength the rock will fail in tension and a sharply defined tensile fracture will be created in the azimuth of S_H. These fractures parallel to the borehole axis are not natural but are created by the concentration of the far field tectonic stresses and as such are referred to as drilling induced tensile fractures (DITF). DITFs are located at azimuths separated by 180° around the wellbore in the direction of the principal horizontal stress S_H (see Figure 4.11).

A different state of stress exists at $\theta = 90°$ where the tangential compression reaches its maximum. At this azimuth compressive shear failure will occur if the state of stress is such that the Mohr-Coulomb friction line is reached. This enlarges the borehole in the direction of the least principal compression S_h and causes Borehole Breakouts (BB). DITFs and BBs are induced into the virgin rock and occur at perpendicular locations on the borehole and so by identifying them, it's possible to diagnose stress orientations of maximum and minimum horizontal stresses.

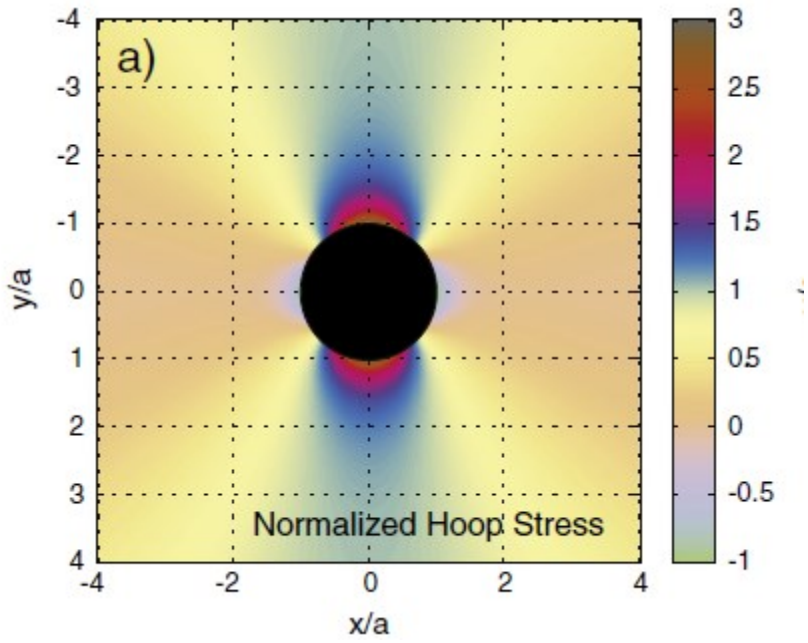

Figure 2.16: Visualization of normalized hoop stress concentrations at the borehole. The maximum horizontal stress is oriented horizontally along the x-axis of this image. The hoop stress reaches its maximum at 90 degrees to this stress at the top of the image and is magnified up to 3 times. The concentration of stresses causes a tensile stress (negative values) to be formed in the direction of the maximum horizontal stress on the side of the borehole. Figure 4a) reproduced from Crustal stress determination from boreholes and rock cores: Fundamental principles by Schmitt et al., 2012 with permission to reprint granted from Elsevier.

The most common and practical method for directly measuring in-situ magnitudes of the horizontal stresses is by carrying out small hydraulic fractures. In these tests a short interval of the borehole is isolated and the pressure within this interval is increased until a hydraulic fracture is initiated. Once a fracture is initiated the borehole pump is shut off and the stress is interpreted from a borehole pressure versus time plot; after a steep decrease in pressure the fracture is interpreted to have closed (stopped being propped open by borehole pressure). This practice will fracture the rock in the direction of maximum horizontal stress and the fracture closing pressure is a measure of the minimum horizontal stress (Schmitt & Haimson 2016).

Another method of measuring stress inside the borehole is to perform a leak-off test. Similar to the hydraulic fracturing method, after the borehole has been cemented and cased, another several metres are drilled into the rock and the drilling mud pressure is increased until a fracture is initiated. The fracturing of the rock causes the borehole pressure to "leak-off" and the moment during which the decline of pressure ceases corresponds to the closing of the fractures. This method is not considered to be at all reliable however.

3. Computed Tomography (CT)

3.1. Introduction

Generally cores are obtained from reservoirs to help solve exploration and production issues. The orientation of features on cores such as fractures and bedding are critical for the understanding of stress, reservoir productivity and structural history of the area. Although orienting core is valuable for modeling and reservoir description, it is expensive. Initially core was oriented using a core barrel that scores the rock with 'knives' to create a reference groove and other non-reference grooves. Images are taken of the grooves during the pause of vibration caused by drilling and a template is created such that the top and bottom of the core may be oriented. For more information see Nelson et al (1987). Nelson (1987) also states the error of orientation from this method is quite large caused by: 1) error in the coring and surveying tool as well as the coring process, 2) error logging data from the core, and 3) error in applying the data. This method has a 'rule of thumb' error of approximately ±11°.

Further efforts have been made to create orientation techniques that are more efficient in time, cost and less dependent on the drill operator. Paulsen et al (2002) describe an orientation technique based on whole surface core scanning of 1m segments of core to obtain digital images and joining the segments into unwrapped segments (Figure 3.1). The images are then loaded into software and single distinguishable points such as fractures or clast centers are oriented with image logs that have been magnetically oriented during acquisition.

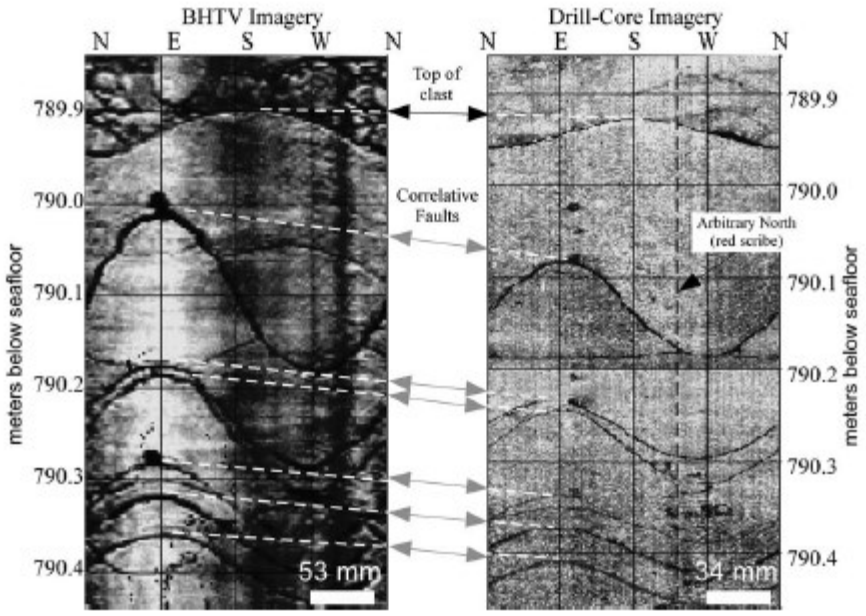

Figure 3.1: Paulsen et al., (2002) core orientation technique using unwrapped full core scanning and borehole televiewer image log. Reprinted from Journal of Structural geology, Vol 24, Paulsen T., Jarrard R.,Wilcon T., A simple method for orienting drill core by correlating features in whole-core scans and oriented borehole-wall imagery, 1233-1238, 2002, with permission from Elsevier

3.2. Computed Tomography Grosmont Scans

In this thesis we discuss an attempt to provide a similar procedure for correlating whole core scans with borehole image logs using computed tomography (CT) a few examples of which are given in Figure 3.2.

CT scan data are x-ray scans of the rock core which allow for non-destructive 3D visualization of the rock. The x-rays emitted from the source pass through the core sections and are attenuated by scattering and absorption. The controlling properties on the x-ray scan are the rock density and atomic numbers and therefore low density areas attenuate the radiation less and show up brighter in the scan. Visual contrast of the greyscale may be adjusted to highlight details of the rock structure. Core CT data have high resolution of imaging and have been used for the study of gas hydrate structure (Rees et al. 2011). Gas hydrate pores may be on the order of μm's and although Rees (2011) concedes this may be on the limit of the ~5μm scale of their CT pixel resolution nonetheless he notes the usefulness of the technique to determine geometry, fabric and volumes. Since our motivation is 3D visualization of the core orientation and rock fractures, the data provides enough planar spatial resolution. Indeed CT data has been noted earlier in the literature to be able to visualize fracture detection with a realistic lower limit for measurement being 0.5 mm

(Hunt et al. 1988). Additionally, the micro-CT scanning of cores is still a relatively emerging field of petrophysical analysis allowing for reliable analysis of high image quality useful for digital core analysis, fluid properties and pore analysis (Katsevich et al. 2015).

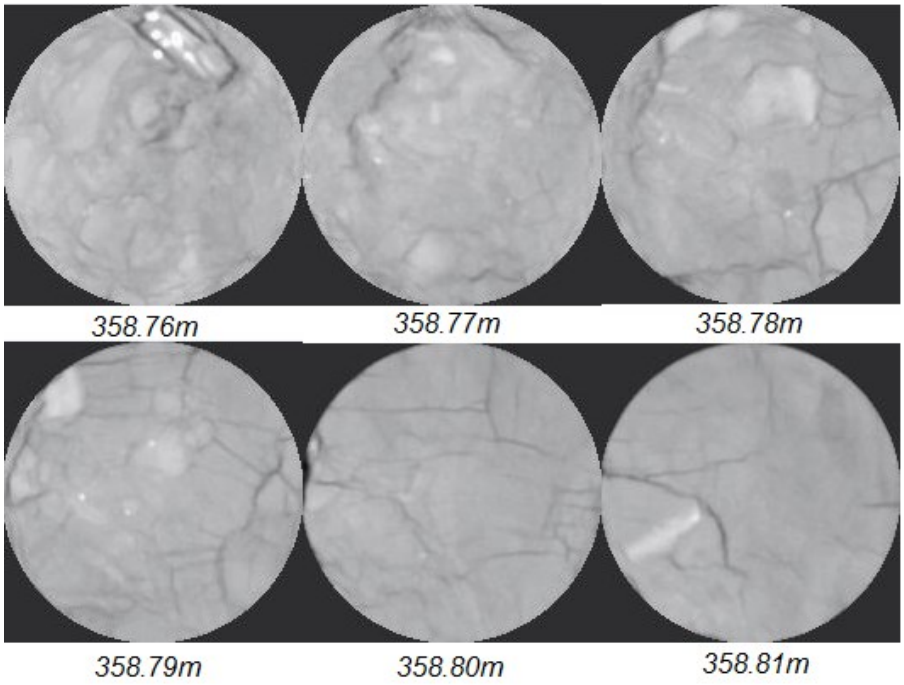

Figure 3.2: A CT slices of rock core spaced vertically 1 cm apart 10cm in diameter. Although the CT dicom images have high lateral resolution the limited vertical resolution results in lack of cohesion between slices where often features in the core change drastically. (Well 11-15-19W4)

The CT data in this thesis was measured over the length of 60m of core in slices taken with 1 cm spacing of the well 11-15-19W4. In order to compare the CT data with the image log data the CT was reordered to appear as an unwrapped core scan. A Matlab code was written to extract the outer pixel of each CT slice and reorder them azimuthally from an arbitrary north position located at the top of the core. Once all the images were reordered, they were then stacked to form a whole core scan shown in Figure 3.3. Regrettably, there does not appear to be sufficient resolution axially to allow this resulting image to display features continuously along the borehole.

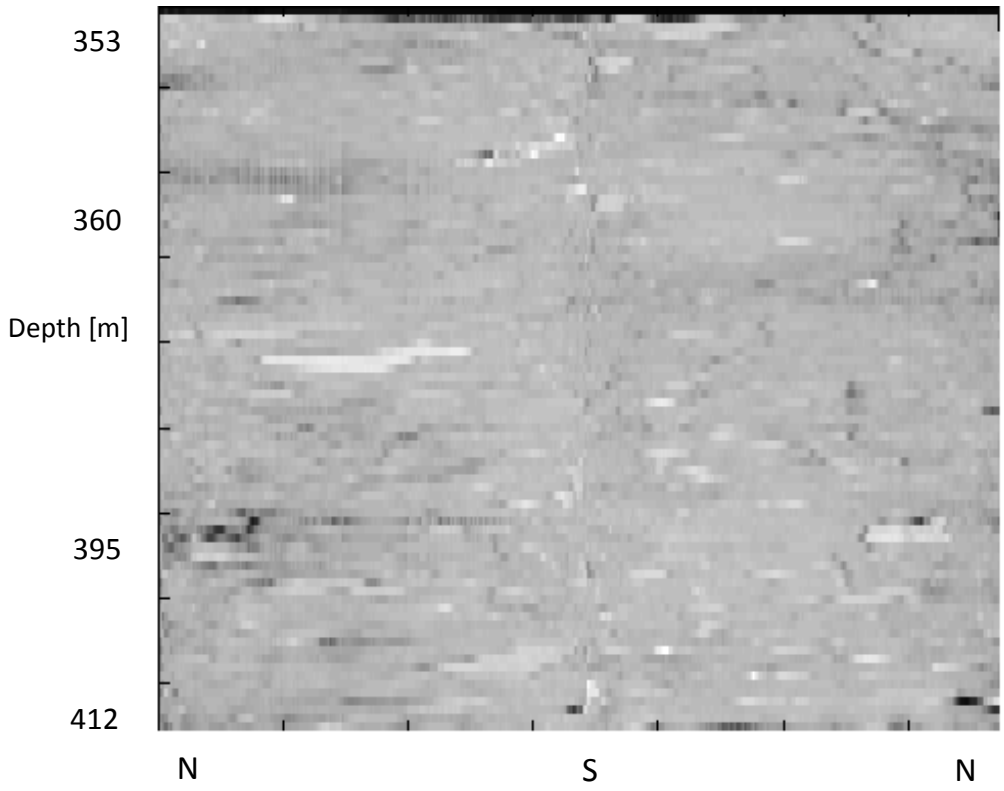

Figure 3.3: The resulting unwrapped CT whole core scan of 60m of core (Well 11-15-19W4)

3.3. Future Recommendations

Although the pixel resolution is quite high along each slice the 1cm separation between the slices is a factor that severely limits the vertical resolution of the whole core scan. While we believe there are promising benefits from the results of the CT whole core scanning procedure, for this case, the sparse sampling limits the output image quality for this application. We would recommend denser CT sampling along the axis of the core so that high resolution core scans could be obtained for core orientation, core fracture visualization and analyses. At the least to aid in fracture and fluid characterization of a target zone, specific small scale scans could be done on reservoir areas across the study area. (There are algorithms in literature seeking to improve reconstructions of helically scanned data in 'quasi real-time' (a few minutes with one GPU) without the introduction of artifacts that can drastically decrease scan times (Katsevich et al. 2015)).

4. Fractures

4.1. Introduction

As already noted in earlier chapters the structure within the Grosmont Formation is particularly complex due to its karsted nature. One aspect of this karsting is that the rock mass also contains numerous fractures, and these can be very important for the production of hydrocarbons as they serve as a primary permeable pathway for fluid flow. In this chapter we characterize the fracture systems at the study site by counting such features observed in oriented image logs. The chapter begins with a description of the geophysical logging instrument used to collect oriented image of the borehole wall, presents the results of the analysis for both natural and drilling induced fractures from the unique set of images from the study site, and concludes with an analysis related to the stress state.

There are now numerous examples of the use of image logs to characterize fractures in geological formations. There are three primary types of image logs: optical, ultrasonic, and electrical. All of these logs provide an unwrapped image of the borehole wall that is oriented with respect to the geographic coordinates. This is usually accomplished using magnetometers on-board the logging tool. A few case studies worth mentioning include data obtained using the optical televiewer or video logging (Lau, 1987), the ultrasonic televiewer (e.g., (Seeburger & Zoback 1982), (Plumb & Hickman S. 1985); (Zoback & Schmitt 1993)), and high resolution oriented electrical resistivity image logs (e.g. Major & Holtz 1997).

4.2. Formation Micro-Imaging Method and Uncertainty

A Formation Micro-Imaging (FMI) tool is a resistivity borehole imaging tool consisting of 4 to 6 caliper arms with attached pads. An extension of dipmeter technology, the FMI resistivity pads are kept pressed against the borehole wall while logging and return high resolution imaging of the borehole rock (Ekstroml et al. 1987). The FMI tool returns an image of the borehole wall in terms of the electrical resistivity at a spatial resolution of a few mm both laterally and vertically. The images are oriented with respect to the geographic coordinates and this is typically accomplished by sets of vector magnetometers that sense direction to magnetic north carried within the logging tool.

The tool operation is described in many texts (e.g. Luthi 2001). Essentially a pad carrying an array of small button electrodes is pushed against the borehole wall. Each of the electrodes is maintained at a constant electrical potential relative to a reference or a return electrode that is housed higher up within the tool. The current passing through each of the electrodes is measured to provide an apparent resistivity that can be used to create a map of the conductance at various points along the borehole wall.

The resulting data allows for core-like characterization of fractures, facies identification and evaluation of stratigraphy. Fractures and other stress features such as borehole breakouts (see Chapter 2) are readily recognizable because the drilling mud will enter the formation fracture and the tool will record an image of the dark identifiable trace of the fracture (Pezard & Luthi 1988). The FMI and other similar electrical imaging tools can only be used in non-oil-based muds such as water, due the low resistivity of the drilling mud. FMI logs provide high spatial resolution (mm scale) in both depth and borehole azimuthal directions and borehole microresistivity variations have long been used for depicting and identifying small scale rock structures (Brudy & Kjørholt 2001) and, as in later in Chapter 4, may be used to infer crustal stress states (Rajabi et al. 2010).

The logs are displayed by having the tool pad readings "unwrapped" along the borehole azimuth and displayed vertically in depth and horizontally in borehole azimuth from 0-360°N (Figure 4.1). In such images, darker colors represent areas of lower resistivity and lighter colors represent areas of higher resistivity. Image logs remain relatively rare and are not used in the standard suite of well logging due to their higher cost and the slow logging speed necessary for the good spatial resolution of the images.

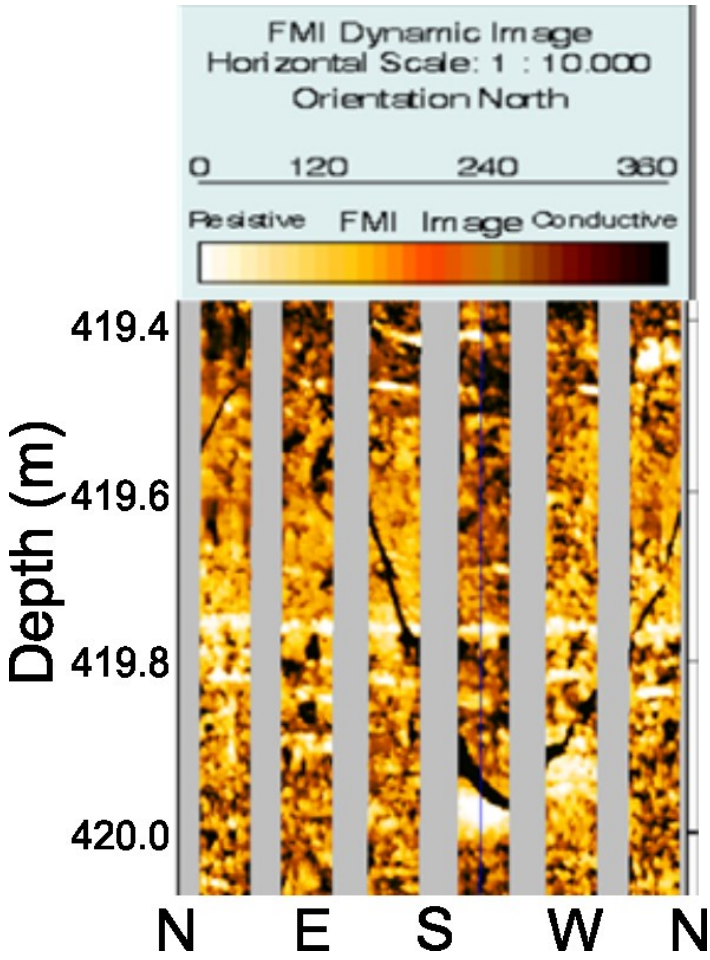

Figure 4.1: An FMI log with a natural fracture cross cutting the borehole. Natural fractures appear sinusoidal in image logs. Image is of well 1-10-85-19W4 from depths 419.40-420.00m. Gray areas represent zones where no data was obtained by the logging tool because the resistivity pads could not cover the entire circumference of the borehole

It is important to comment on the expected appearance of fractures within the images and Figures 4.1 and 4.12 provide good examples of natural and drilling induced tensile fractures respectively. The orientation of a natural fracture is given by a dip-direction (as measured from geographic North) and a dip (as measured from the horizontal). If a 2D plane is considered to appropriately model such a fracture then the line of intersection of this plane with the 3D borehole will appear in the unwrapped 2D image of the borehole wall as a sinusoid (Figure 4.1). With knowledge of the real borehole borehole's diameter, the dip $\emptyset$ is given from the height (i.e. peak to peak amplitude) of the sinusoid by simple trigonometry ($\emptyset = \tan^{-1}\frac{height}{Diameter}$). The dip direction is the azimuth where the minimum of the sinusoid is found.

In contrast drilling induced tensile fractures (DITF) open at the azimuths around the borehole that point in the direction of S_H as discussed in Chapter 2. Ideally these are distinguishable as two parallel lines separated by approximately 180°; although they can have complicated structure where the fracture commences and ends as they may have a sinusoidal-like appearance and could be misinterpreted as natural fractures.

The natural fractures data were picked in the FMI logs using a Matlab code written to pick and orient the fractures' dip angle and dip direction (see Appendix) from the images directly. First the fractures were identified and logged into an excel worksheet. Next the image log files were exported into the Matlab workspace and picked using a graphical mouse input function relating the pixels chosen by the user's mouse to the log depth and azimuth data. Because the log images are 'unwrapped' mappings from the inside cylindrical surface of the borehole to a 2D plane, the planar fractures that are cross cut by the borehole appear as black sinusoidal curves in the images (Figure 4.1) as noted earlier. Hence, the mouse was used to pick the maximum and minimum points of the sinusoid to give the fracture sinusoid height and dip direction. An earlier discussion of this procedure may be found in Lau et al, (Lau 1987).

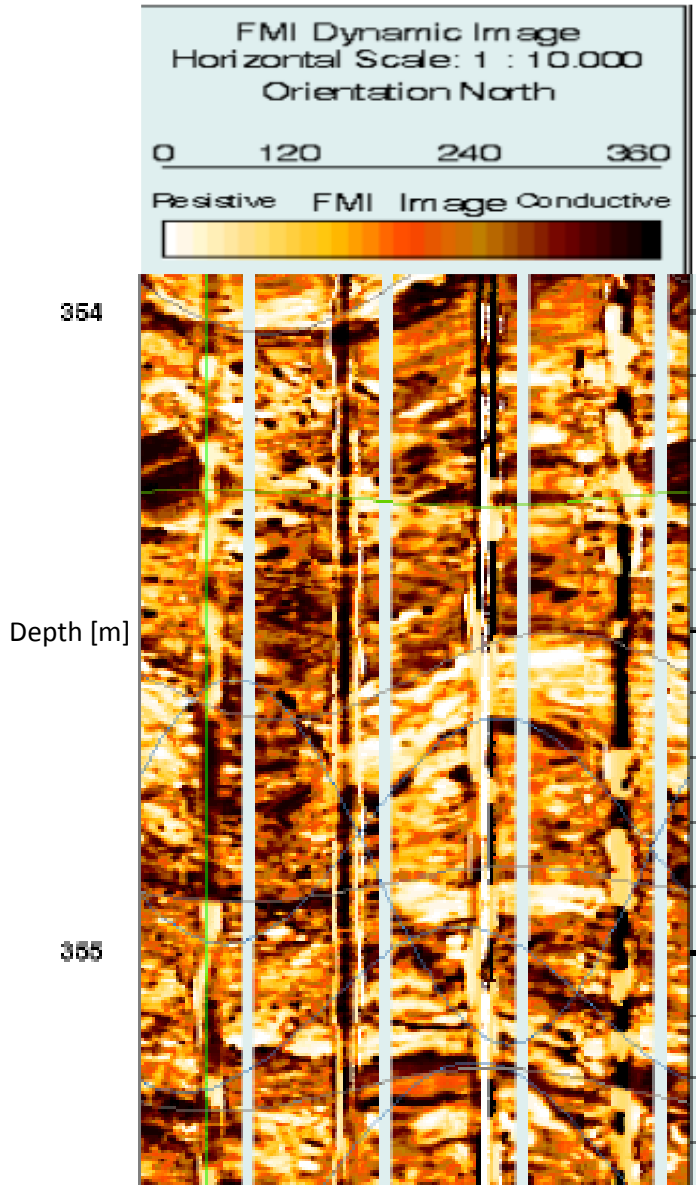

Figure 4.2: Image shows area of vertical distortions of bitumen smearing distorting image log and could be confused as drilling induced tensile fractures (Well 10-15-85-19W4).

Interpreting fractures in a carbonate heavy oil reservoir may contain inherent difficulties. As described by Russel-Houston and Gray (2014), fracture characterization in the Grosmont can be misleading because: 1) large scale fractures could appear discontinuous on well-bore scale due to sudden rheological contrasts in breccias, vugs or beds; 2) clast boundaries in zones of breccia can be misidentified as fractures (Figure 4.3); 3) smearing of the highly resistive bitumen on the FMI pads can severely reduce the resolution of the image logs (Figure 4.2), and 4) near vertical fractures being misidentified as induced (Figure 4.4) or completely missed by the tool should its pads provide inadequate azimuthal coverage (i.e. in the gray area of Figure 4.1). In light of this, fracture

logging was done while consulting core images provided in order to reduce mischaracterization from bed boundaries or abrupt changes in lithology (Figure 4.3). We should note that much of the slabbed core image data is broken and missing many intervals at depth. Additionally, no fractures were logged in or directly near areas of extremely vuggy stratigraphy (e.g., Figure 4.3).

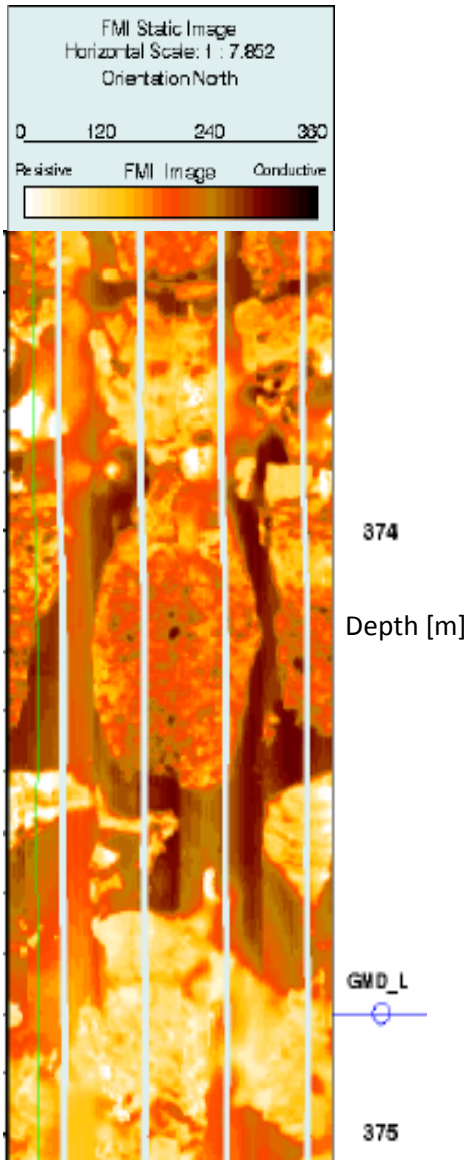

Figure 4.3: Image shows area of breccia and complex lithology making it difficult to distinguish fractures. (Data taken from well 10-15-85-19W4)

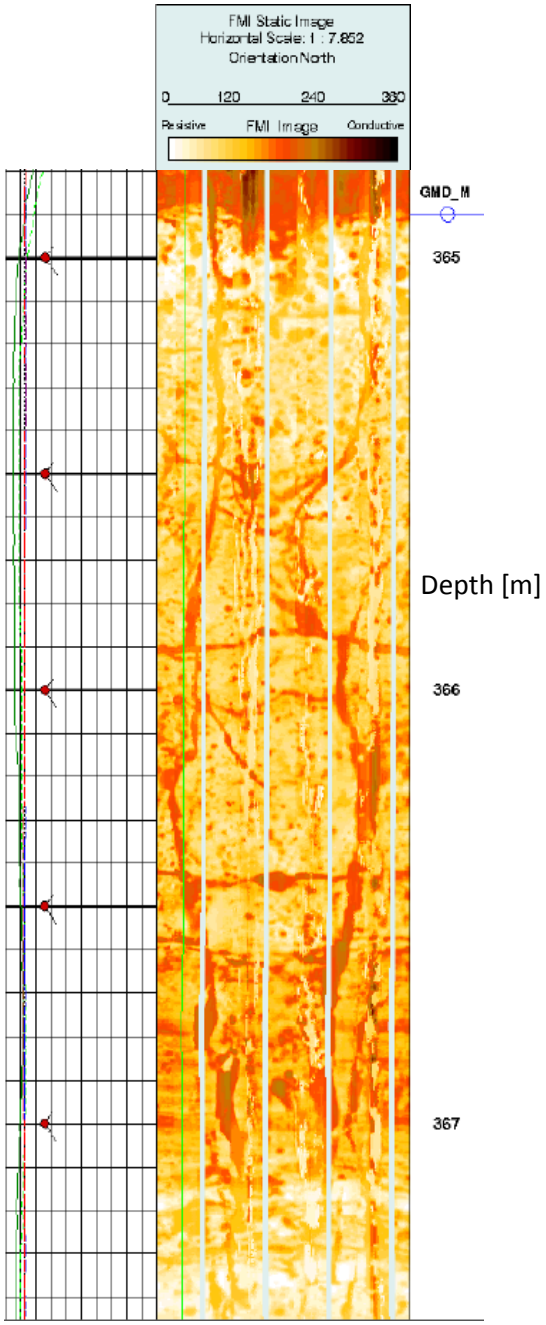

Figure 4.4: Image showing high angle natural fractures that could be misidentified as DITF. (Data taken from well 10-15-84-19W4)

Another phenomenon that can obscure natural fracture interpretation are induced features such as DITF`s, or other induced features such as petal fractures. Petal fractures (Figure 4.5) initiate at the edge of the borehole and curve parallel downwards to the drill stem thus obscuring the interpretation of natural fractures present.

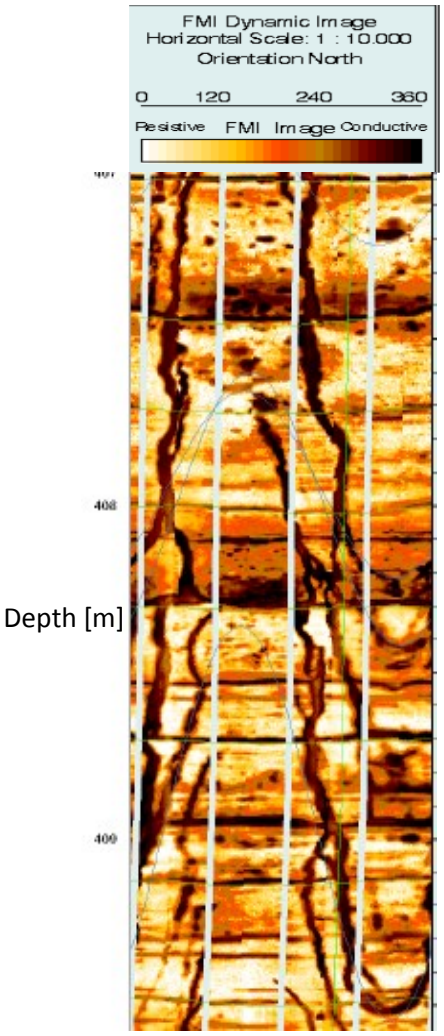

Figure 4.5: Petal fractures adding uncertainty in natural fracture interpretation. (Data from well 4-16-85-19W4)

4.3. Natural Fracture Data

This section will present the results of the interpreted fractures as well as statistics of the data. As noted earlier, this is an exceptionally unique data set that includes data from 22 wells all contained within a rather small area of about 10 km by 10 km (Figure 4.6a) although most of the wells come from a smaller area. From the 22 image logs: depth of fracture, fracture count, mean fracture azimuth, fracture dip and fracture count were collected. From these fracture dips and dip directions, rose diagrams and density contouring were calculated and plotted. Detailed information about the locations and geometries of the wells is given in Table 1.

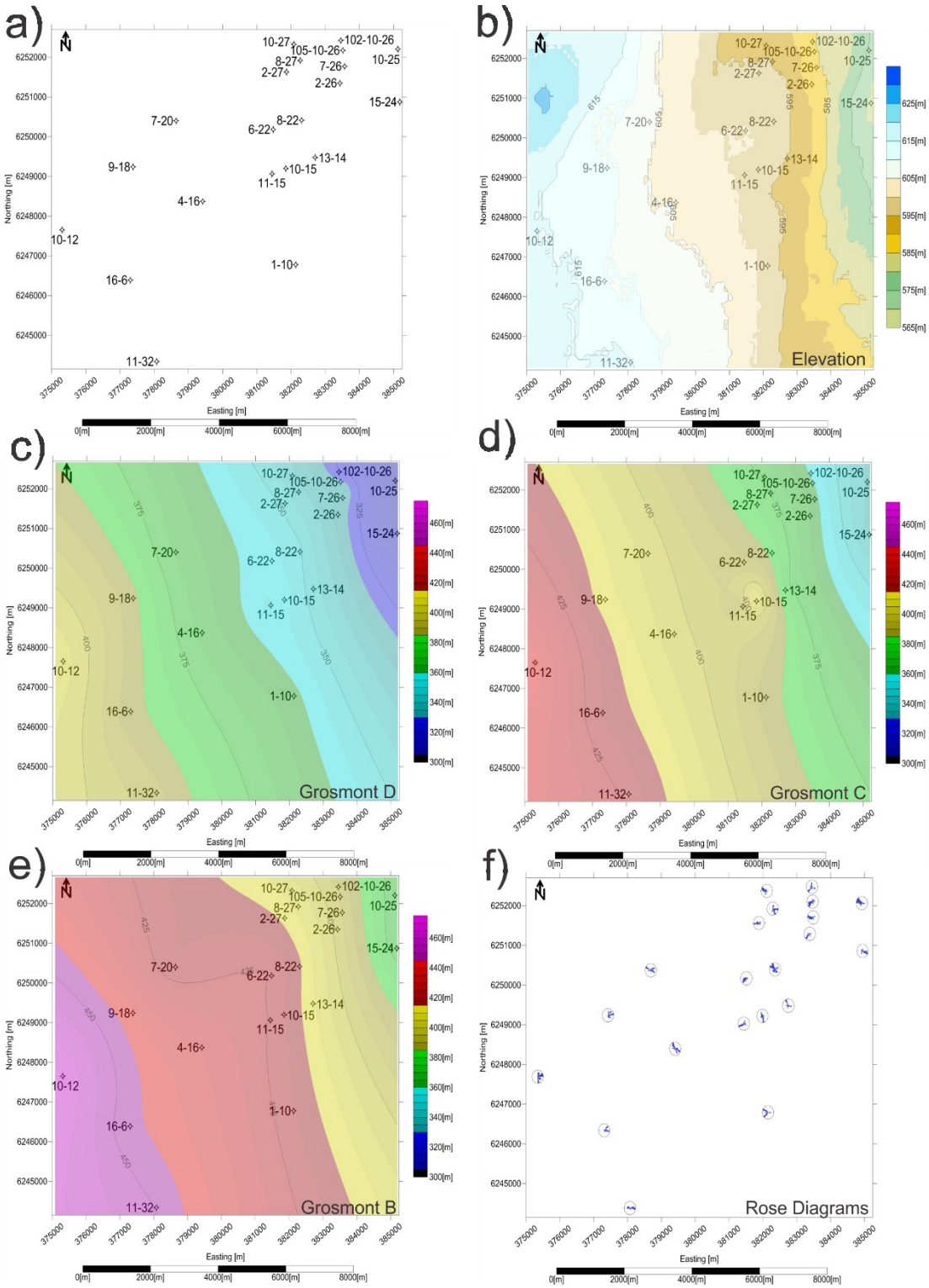

Figure 4.6: a) Plan map of the positions of the 22 boreholes from which image logs were obtained for this study. Projection is in UTM Zone 12N. b) Topography over the area as derived from Geological Survey of Canada data bases. c) The Grosmont D horizon over the study area. d) The Grosmont C horizon over the study area. e) The Grosmont B horizon over the study area. Note there was insufficient well data for the Grosmont A as most wells did not intersect it. f) Rose diagrams of natural fractures at well location.

In the fracture picking program each fracture is referenced with respect to the measured log depth. The blind results of this picking, without regards to any additional corrections (Figure 4.7a) displays an apparent distribution peak centred at a depth of just below 360 m. However, analysis of this plot at face value is misleading because the log depth is usually measured from a reference point on the drill rig called the 'kelly-bushing' which in turn is located a variable distance above the ground surface which, as shown in Figure 4.6b, rises by nearly 50 m from east to west. The proper elevation corrected frequency plot in Figure 4.7b shows a much more localized distribution of the fractures at an elevation of about 240 m. The data was then separated into two zones above and below the Grosmont C interval by hanging the depths on the Grosmont C top in all wells. The majority of the fractures correspond to the Grosmont D member which as discussed in Chapter 2 is the primary fractured interval and contains vugular porosities cause by leaching but is also highly brecciated which may have caused a biasing in fracture picking.

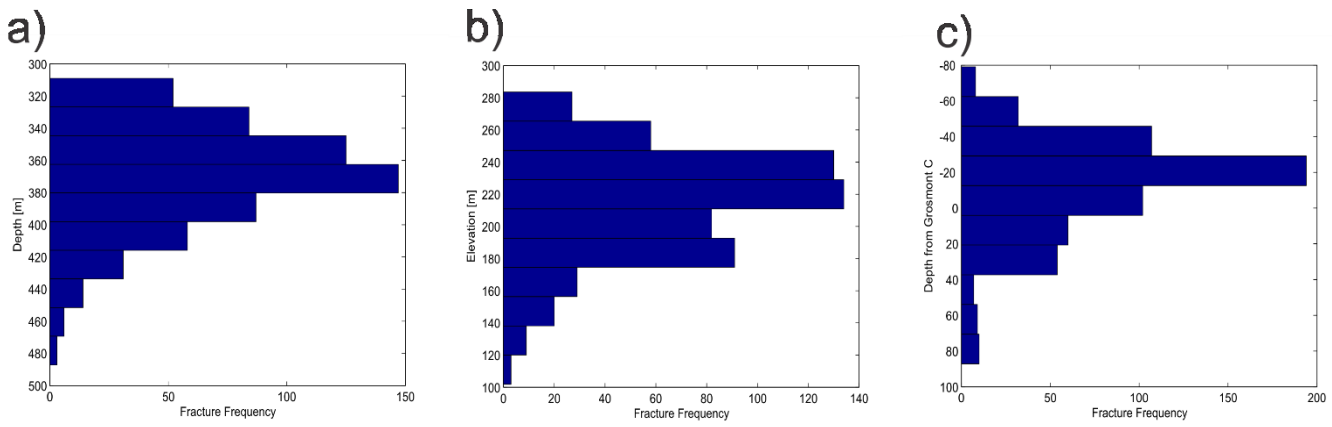

Figure 4.7: Frequency of natural fractures logged with depth from all wells. a) face-value plot of fracture frequency versus depth. b) Fracture frequency versus elevation corrected depth using reference elevation given by the Canadian Digital Surface Model c) Fracture frequency hung on depth of Grosmont C formation per well.

The additional fracture characteristics of dip angle and dip direction are provided in Figure 4.8 with the symbols coded to represent the Grosmont unit from which the fractures were interpreted. These plots show the concentration of the fractures at the depths as given already in Figure 4.7. In this kind of plot, however, there is no clear preferential dip or strikes that are readily apparent, and a more involved statistical analysis was carried out using circular statistics both on the data set as a whole and on each borehole individually.

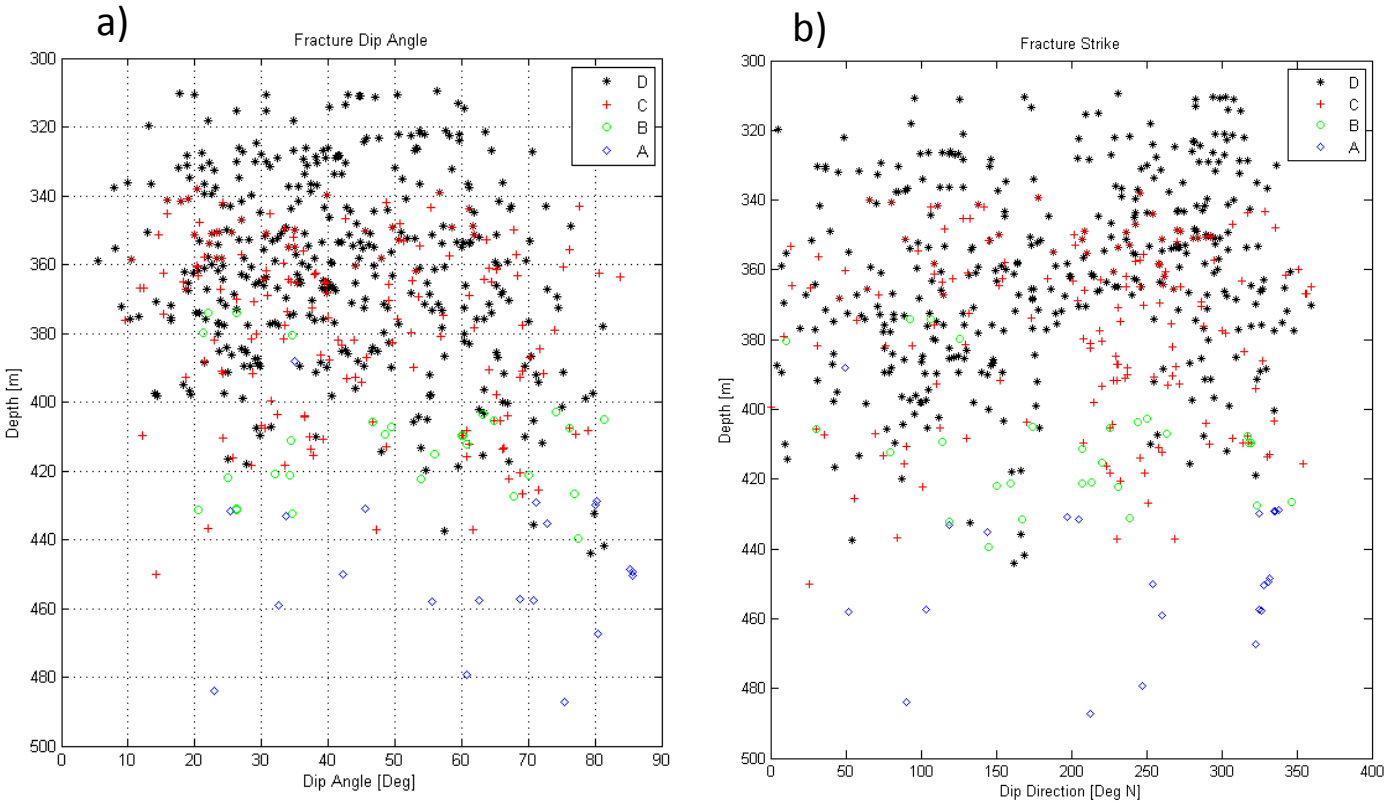

Figure 4.8: Measured fracture characteristics of a) dip angle and b) dip direction for the entire data set plotted versus depth. Data is color separated by Grosmont Formation units A, B, C, and D.

Well ID	Easting [m]	Northing [m]	Elevation [m]	Depth Grosmont D [m]	Depth Grosmont C [m]	Depth Grosmont B [m]	Depth Grosmont A [m]	Fracture Count	Resultant	Critical Value (5%)	Preferred Orientation	Mean Direction [deg N]
1-10-85-19W4	382136	6246776	580	362	388	421	N/A	8	0.589	0.602	No	257
2-26-85-19W4	383431	6251350	580	333	365	398	N/A	19	0.356	0.394	No	227
4-16-85-19W4	379419	6248372	589	369	403	435	448	25	0.074	0.344	No	33
7-20-085-19W4	378639	6250397	600	370	404	N/A	N/A	22	0.208	0.367	No	76
8-27-85-19W4	382271	6251922	607	340	374	408	N/A	9	0.454	0.569	No	116
9-18-85-19W4	377385	6249238	595	388	413	442	N/A	23	0.253	0.359	No	94
10-12-85-20W4	375304	6247654	598	410	445	467	N/A	19	0.099	0.394	No	86
10-15-85-19W4	381848	6249200	603	389	414	421	N/A	61	0.215	0.244	No	214
10-25-85-19W4	385124	6252203	593	308	339	371	384	39	0.447	0.273	Yes	284
11-15-85-19W4	381450	6249065	568	354	393	425	434	39	0.211	0.273	No	194
11-32-84-19W4	378076	6244337	594	393	425	451	469	19	0.135	0.394	No	163
13-14-85-19W4	382705	6249479	588	347	377	411	425	22	0.181	0.367	No	314
15-24-85-19W4	385183	6250874	589	307	338	370	383	31	0.193	0.315	No	110
16-6-85-19W4	377304	6246387	567	388	421	447	N/A	31	0.647	0.315	Yes	88
10-32-85-19W4	378750	6254036	608	369	400	435	N/A	N/A	N/A	N/A	N/A	N/A
100-2-27-85-19W4	381868	6251633	597	348	379	413	N/A	50	0.269	0.244	Yes	237
100-6-22-85-19W4	381481	6250179	571	357	390	425	438	50	0.438	0.244	Yes	238
100-8-22-85-19W4	382308	6250412	590	351	383	416	N/A	48	0.176	0.257	No	272
100-10-27-85-19W4	382087	6252326	584	341	372	406	417	40	0.613	0.273	Yes	267
120-7-26-85-19W4	383569	6251772	584	336	361	394	N/A	24	0.474	0.351	Yes	245
102-10-26-85-19W4	383458	6252422	569	324	358	392	N/A	13	0.344	0.475	No	243
105-10-26-85-19W4	383513	6252172	584	325	359	394	N/A	30	0.287	0.315	No	255
Averages			587	353	386	415	425*	*Total:*622				

Table 1: Table of well data with log depths of Grosmont Formation units, elevation, logged fracture counts, the calculated resultant of natural fracture data, Rayleigh test critical values (from Mardia (1972) appendix 2.5) and preferred orientation test results.

To calculate statistics of circular data it's useful to regard angular observations as points on a circle of unit radius (Mardia 1972). Since the azimuthal data measurements are in a range of $0° \leq \theta \leq 360°$ there is a contrast between the statistics of a linear distribution rather than a circular one. An illustration of this is to consider the mean of two data points 345° and 5°. A naïve approach would be the usual summation of the values and dividing by 2 to obtain an incorrect mean angle of 175°. However, the correct mean angle is 355°. Following Mardia (1972), the mean direction of the data can be calculated as defining the resultant of unit vectors from the origin to the points on the circumference of a unit circle. In Cartesian coordinates the resultant vector, *r*, can be calculated by the set of equations

$$C = \frac{1}{n}\sum_{i=1}^{n} cos\theta_i \,, \tag{4.1}$$

$$S = \frac{1}{n}\sum_{i=1}^{n} sin\,\theta_i \,, \tag{4.2}$$

and

$$r = (C^2 + S^2)^{\frac{1}{2}}. \tag{4.3}$$

Above, n is the number of points and θ are the measurement angles. $R = nr$ is therefore the length of the resultant. The mean of the data, x_o, is calculated from

$$x_o = \arctan\left(\frac{S}{C}\right). \tag{4.4}$$

Further, the circular variance, S_o, is defined by

$$S_o = 1 - \frac{R}{n}. \tag{4.5}$$

The circular standard deviation, S_{std}, is defined by

$$S_{std} = \frac{1}{l}\sqrt{-2\ln(1 - S_o)} \tag{4.6}$$

Where *l* in equation *(4.6)* is given by the range of angular data on $(0,2\pi/l)$. The mean direction of the data is directly analogous to that of a set of scalar measurements. It follows that when observed

points are more tightly clustered about the mean, the resultant length will be high and approach the number of observations n, causing S_o to decrease. The resultant provides information on the spread (variance) of the data and the average direction. The circular variance takes values from (0,1) while the circular standard deviation, S_{std}, is a transformation of S_o to the range (0,∞) and is analogous to a standard deviation on the line. For bimodal data such as drilling induced tensile fractures one can use an angle doubling procedure that will be discussed in Chapter 4.4. It is also possible to test the uniformity of the distribution using the Rayleigh test. The Rayleigh test is an extremely simple calculation of the resultant given in equation *(4.3)*; the resultant is then compared to critical values based on a chosen level of significance (see Table 1). The Rayleigh test tests a hypothesis of uniformity in the data and therefore the significance of a mean direction. The Rayleigh test assumes that the data satisfies a von Mises distribution otherwise known as a circular normal distribution. The critical values are a comparison against how strongly the data contradicts the null hypothesis (uniformity). Essentially, if the resultant is sufficiently large, the hypothesis of randomness of the data can be rejected. A full derivation of the Rayleigh uniformity test can be found in Mardia (1972). By using the value of the resultant, the number of measurement angles and the critical values given from Mardia Appendix 2.5 (Mardia 1972, pg 300), the hypothesis of uniformity can be rejected or affirmed.

With this in mind, here the fracture azimuthal statistics as a whole tested negative for a preferred orientation; that is, when all the fracture azimuths from all the wells are analyzed together the fractures appear to be randomly oriented. However, this general observation does not hold for all of the boreholes if they are analyzed individually as is seen for 6 of the boreholes in Table 1. It is interesting to note that for these 6 wells, their average preferred fracture azimuths are oriented approximately East or West-South-West (Figure 4.9). Shortly, it will be seen that this directions is intermediate to that for the horizontal principal stresses. Conversely, this means there does not appear to be any relationship between the modern in situ stress state and the orientations of the observed natural fractures. This contrasts somewhat with Babcock's (1973;1974;1978) interpretations of near surface joint sets to the northwest of Saleski.

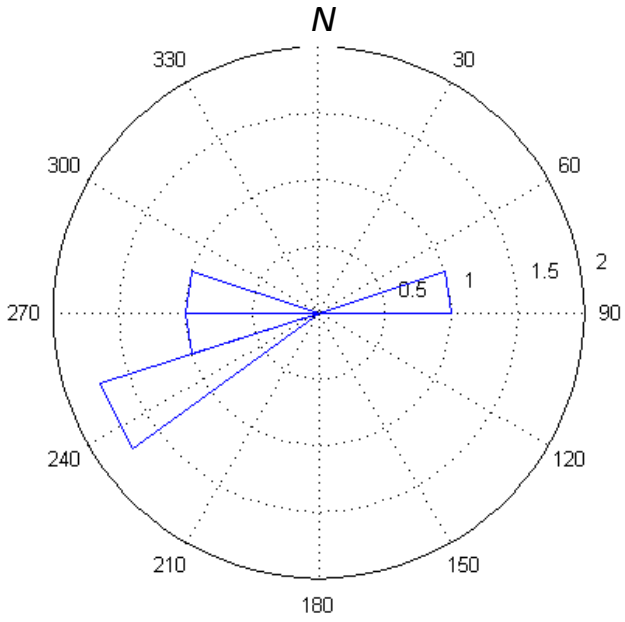

Figure 4.9: Rose plot diagram of mean direction of 6 well fracture dip-vector azimuths that tested positive for preferred orientation. Mean fracture azimuths trend East to West South-West.

An additional way to view and analyze the dip azimuth and dip angle of the fracture data is by plotting it using an equal area Schmidt net stereographic projection (Figure 4.10). The data can be contoured by the density of the points. By selecting specific parameters while contouring the data, we can extract significant orientation information from the data (Kamb, 1959). For a total of N data points, a density contour counting circle area A is chosen such that the expected number of points $E = NA$ that lie within the counting area A is three times the standard deviation, σ, of points n that actually fall within the counting area (Kamb 1959). This means that the observed orientation density could not have resulted from random sampling of a population that lacks preferred orientation. Following Kamb (1959), within a given area A the distribution of n values is binomial and the standard deviation may be represented by

$$\frac{\sigma}{E} = \sqrt{\frac{(1-A)}{N}\,A}. \qquad (4.7)$$

Therefore setting $\sigma/E = 1/3$ we calculate the appropriate counting circle radius r for N points.

$$r = \frac{3}{\sqrt{\pi(N+9)}}. \qquad (4.8)$$

Once the optimum radius of the counting circle was determined, the fracture orientation density was contoured (see Appendix). The code counts all point within the counting circle given by the optimal radius and the observed densities are contoured by multiples of σ. Since the expected density for the number of points expected to fall within the given area is three times the standard deviation, the contours above this are considered statistically significant. The final Kamb contour plot is giving in Figure 4.11.

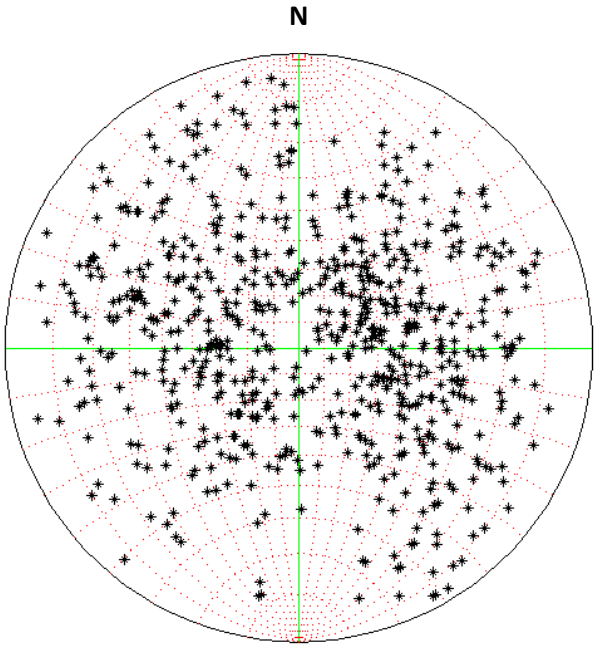

Figure 4.10: Equal area hemispherical projection plot of all the poles to natural fracture and azimuths on a lower hemisphere. Each point here represents a pole to fracture plane at an angle counting upward inward from the radius of the circle (ie; a point on the edge of the circle is 0° dip angle and a point at the center is 90° dip angle). The dip azimuthal directions are counted as on a compass with North being 0°

The width, or aperture, of a fracture is critical to estimation of in situ permeabilities. Ideally, we would seek to make some estimate of the fracture aperture from the images. However, the FMI images of electrical resistivity are essentially the end product of an inversion procedure that employs a pattern of closely spaced electrodes. As a result the final image contains significant smearing of features. We do note that there have been attempts in the past to estimate fracture apertures from FMI image data in crystalline rocks (e.g. (Henriksen 2001), Sausse & Genter

2005)). Genter et al (1997) provided an extensive comparison of borehole image to core data that, too, appears to indicate that many of the smaller aperture fractures are not properly detected in the image logs. Luthi & Souhaite 1990 and Ponziani et al. (2015) do provide a discussion of how data from an FMI device can be used to estimate fracture apertures but this is a somewhat involved process that requires data from individual electrode buttons, access to the appropriate tool calibration constants, and accurate measurements of the in situ rock and borehole fluid resistivities. As most of this information is not accessible to us, and because of the added problem of the image smearing due to the existence of highly resistive bitumen we did not attempt to make estimates of fracture apertures from the image logs. It could be that better measures of this could be obtained from ultrasonic image logs in this kind of environment instead. This is a potential project for future study.

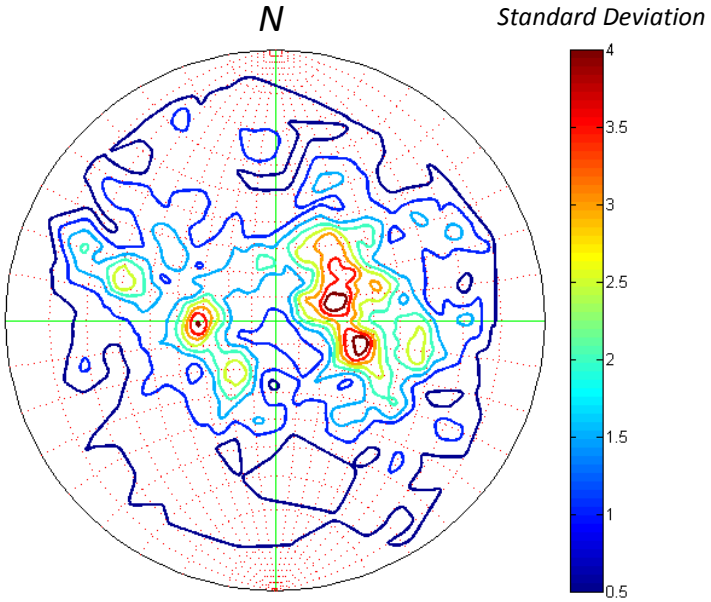

Figure 4.11: Density contours of the poles to natural fracture dips using Kamb's method. Colorbar is in standard deviations. Areas with hotter colors indicate probable preferred orientation of fractures at 50-70° angled poles to the East North-East, East South-East and West with respect to the average random distributed natural fractures. These hotspots suggest that the higher (>30°) dip angle fractures are preferably oriented East and that lower (<30°). The results of the Kamb contouring seem to match the mean fracture azimuths of the wells that tested positive for preferred direction showing strong East-West trending (Figure 4.9).

To summarize this section, 622 fractures were interpreted from 22 sets of image logs through the Grosmont formation at the study site. The fracture strikes and dips were obtained using a Matlab based code designed to pick the fracture height as well as the dip-direction azimuth. The highest fracture frequency was found in the D unit of the Grosmont formation however the C unit was also heavily fractured. The reasons why the fractures congregate at this depth are most likely due to the karsted features and the crackled breccias. There do not appear to be any strong preferences for the fracture orientations in the overall data set. However, in a limited number of the boreholes the fractures do have a preferential mean direction and the Kamb contouring displays an East-West direction that may be related to Babcock's System II joint set fracture orientation studies carried out in the 1980's. However his joint set data was prevalently vertical while our data has a multitude of dips.

4.4. Directions of Drilling Induced Tensile Fractures

Drilling induced tensile fractures were introduced in Chapter 2. To reiterate, we assume here that the boreholes in the study area are vertical and that their axis aligns with the vertical principal stress S_V. Further presupposing that Kirsch's equations provided Chapter 2 these tell us that drilling induced tensile fractures will first occur at those azimuths along the borehole wall pointing in the direction of the greatest horizontal compression S_H. Consequently, if drilling induced tensile fractures exist they will appear as two vertical fractures separated by 180° from each other in the image as shown in Figure 4.12.

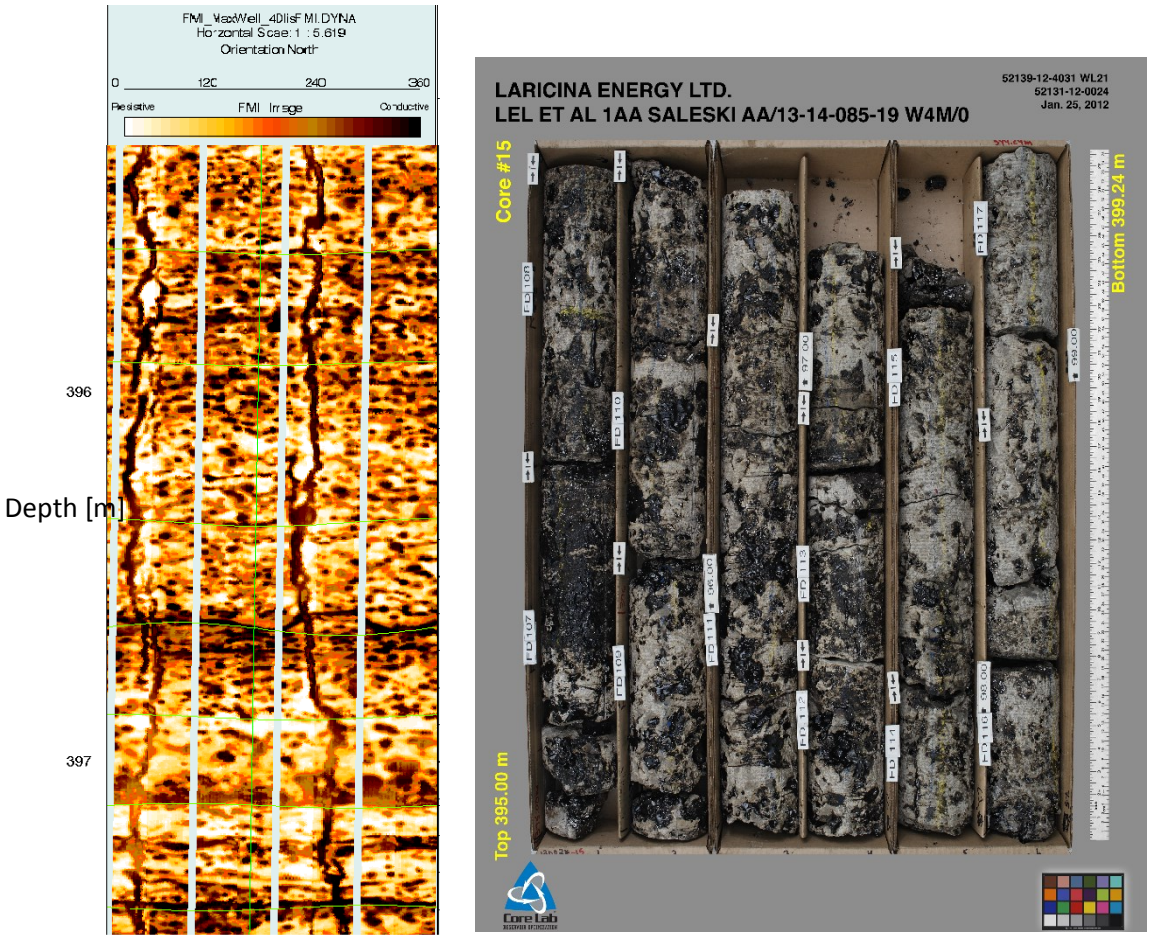

Figure 4.12: Example of drilling induced tensile fracture in FMI log data. Data taken from well 13-14-85-19W4.

In this section, results from the measurement of the azimuths of drilling induced tensile fractures in the image logs are presented. Details of the wells, depth of tensile fractures recorded, tensile fracture count, rose diagrams and maximum horizontal stress is presented in Tables 2, 3, 4 and Figure 4.13. The program (see Appendix) written to pick the fracture strike and dip was also applied here to determining the strike directions of the drilling induced fractures.

It is important to indicate some of the criteria used in picking such fractures. Typically, only those that appear as a pair directly opposite of one another are chosen. Care was taken to avoid any vertical natural fractures as was already shown above in Figure 4.4. Admittedly, only 1 case of this is found as confirmed by examination of the rock core as pointed out by our industrial collaborators. The core photographs were consulted if there was any doubt as to whether the observed fractures were natural or induced, existence of fracture in the image log (i.e. on the

borehole wall) but not within the core is taken as a good indicator that the fracture was drilling induced.

Well	Grosmont D	Grosmont C	Grosmont B	Grosmont A
1-10-85-19	**0**	**1**	**0**	**0**
2-26-85-19	**0**	**4**	**2**	**0**
4-16-85-19	**1**	**3**	**3**	**4**
7-20-85-19	**0**	**1**	**0**	**0**
9-18-85-19	**1**	**6**	**0**	**0**
10-12-85-20	**6**	**2**	**0**	**0**
10-15-85-19	**1**	**2**	**0**	**0**
10-25-85-19	**3**	**0**	**1**	**1**
11-15-85-19	**1**	**1**	**0**	**0**
11-32-84-19	**1**	**1**	**1**	**0**
13-14-85-19	**0**	**4**	**0**	**3**
15-24-85-19	**2**	**3**	**2**	**0**
16-6-85-19	**1**	**1**	**1**	**0**
100-2-27-85-19	**1**	**3**	**0**	**0**
100-6-22-85-19	**1**	**0**	**0**	**0**
100-8-22-85-19	**2**	**0**	**0**	**0**
100-10-27-85-19	**0**	**2**	**3**	**0**
102-7-26-85-19	**0**	**3**	**0**	**0**
102-10-26-85-19	**4**	**0**	**0**	**0**

Table 2: Table containing the drilling induced tensile fractures logged per formation in each well.

Interval	DITF Count
Grosmont A	8
Grosmont B	14
Grosmont C	39
Grosmont D	27
Total	**88**

Table 3: Table containing the total number of drilling induced tensile fractures per interval.

Well ID	*Natural Fracture Rose Plot*	*DITF Rose Plot*
1-10-85-19W4	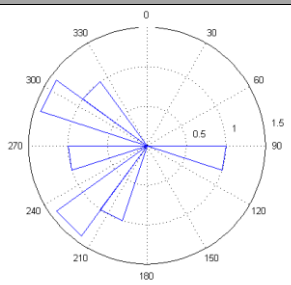	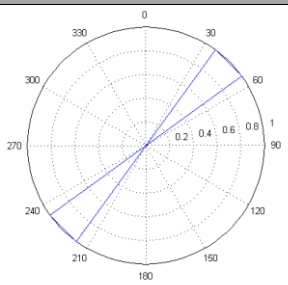
2-26-85-19W4	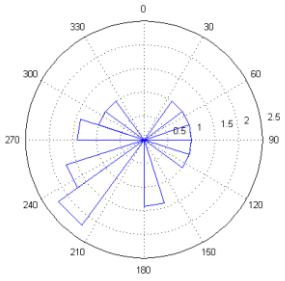	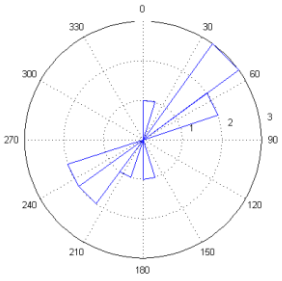
4-16-85-19W4	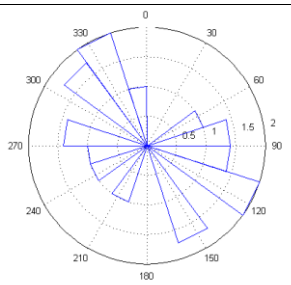	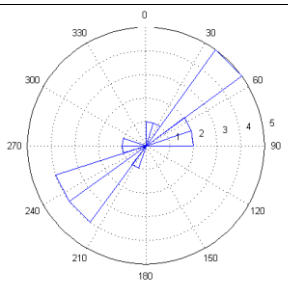
7-20-085-19W4	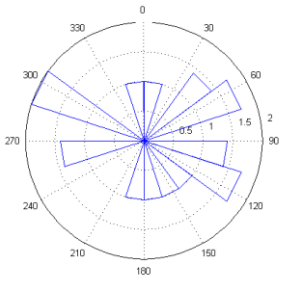	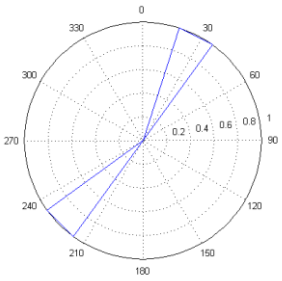
8-27-85-19W4	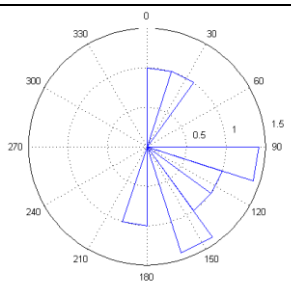	

9-18-85-19W4	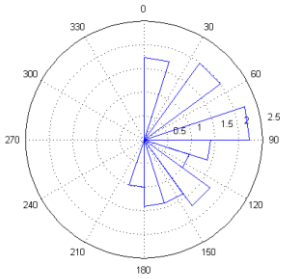	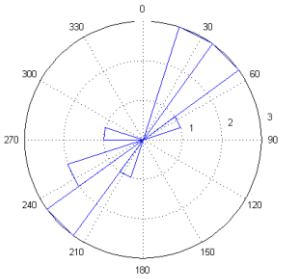
10-12-85-20W4	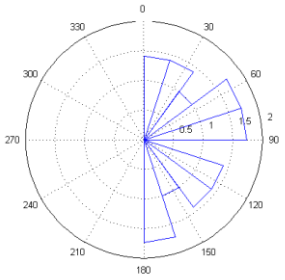	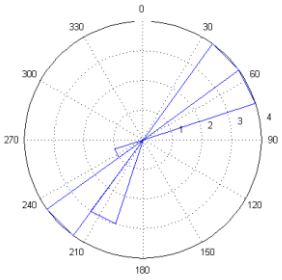
10-15-85-19W4	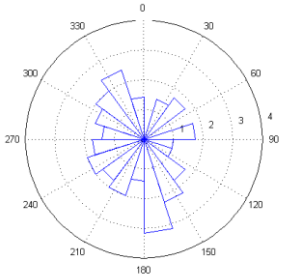	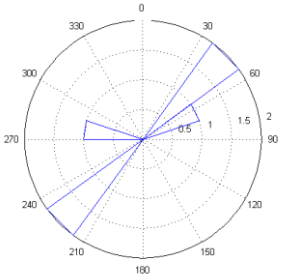
10-25-85-19W4	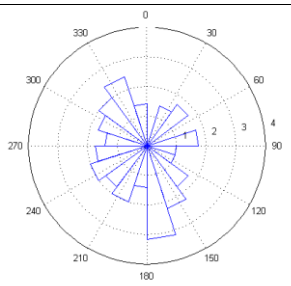	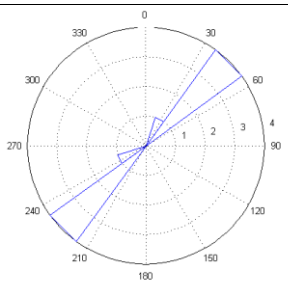
11-15-85-19W4	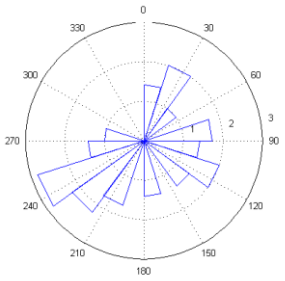	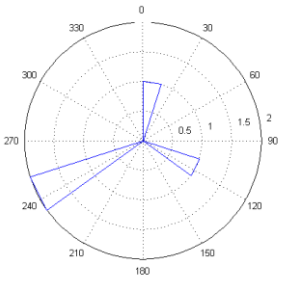

11-32-84-19W4	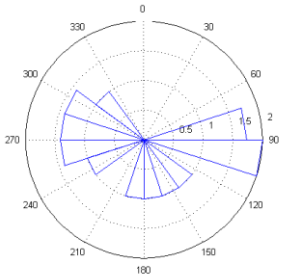	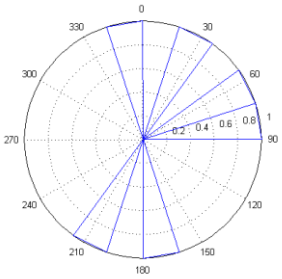
13-14-85-19W4	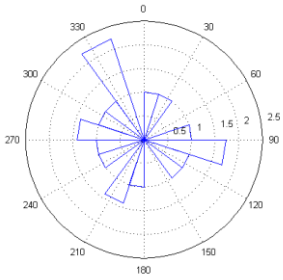	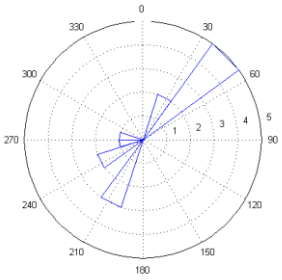
15-24-85-19W4	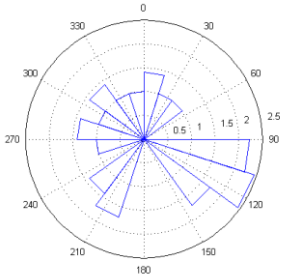	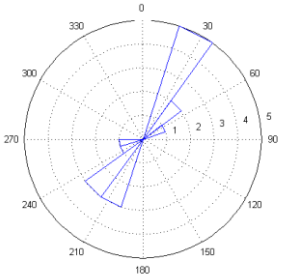
16-6-85-19W4	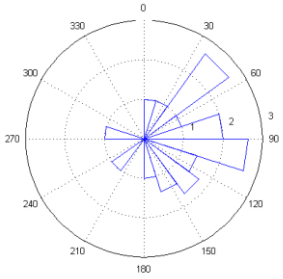	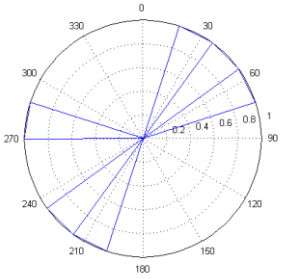
100-2-27-85-19W4	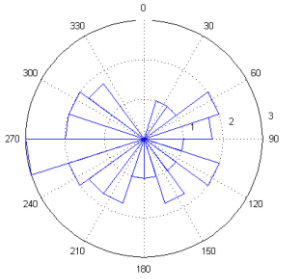	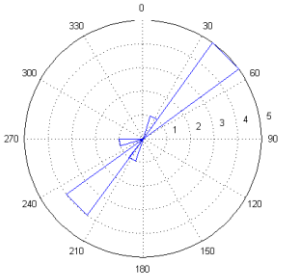

100-6-22-85-19W4	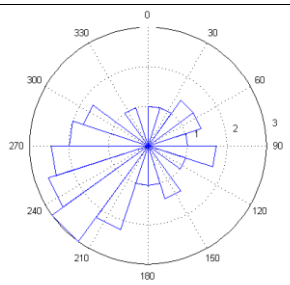	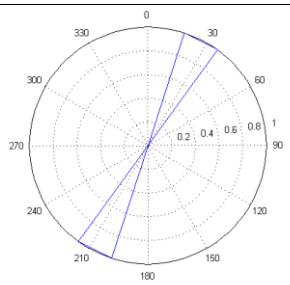
100-8-22-85-19W4	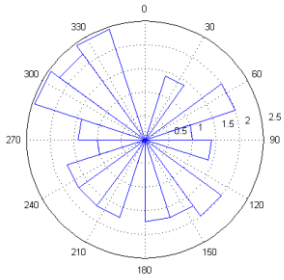	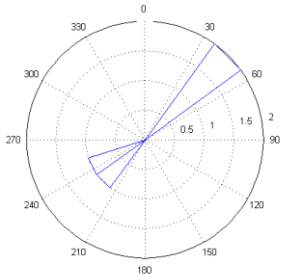
100-10-27-85-19W4	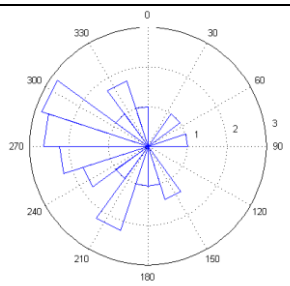	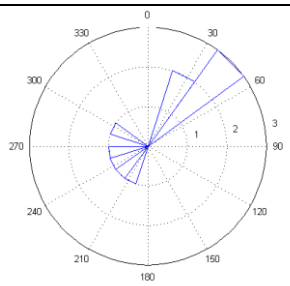
102-7-26-85-19W4	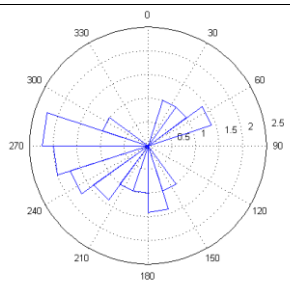	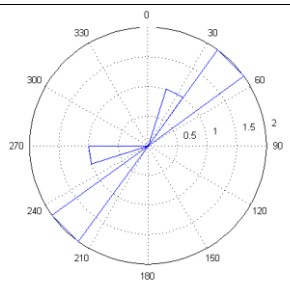
102-10-26-85-19W4	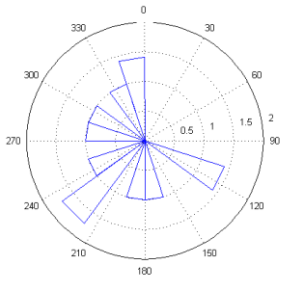	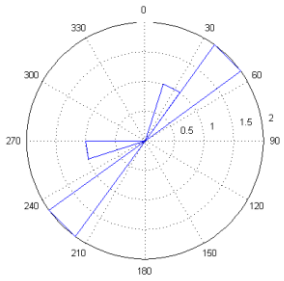

105-10-26-85-19W4	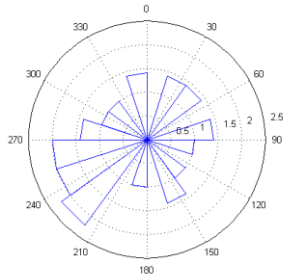	

Table 4: Table listing all the natural fracture rose diagrams and DITF rose diagrams. Wells without DITF are greyed out.

The azimuthal directions of the DITF are indicative of the maximum horizontal stress direction in the region. The data is bimodal and data between 180° and 360° are equivalent to those on the interval 0-180°. Again, following Mardia (1972) we employ an angle doubling procedure where θ_i now becomes:

$$\theta_i^* = 2\theta_i \, . \tag{4.9}$$

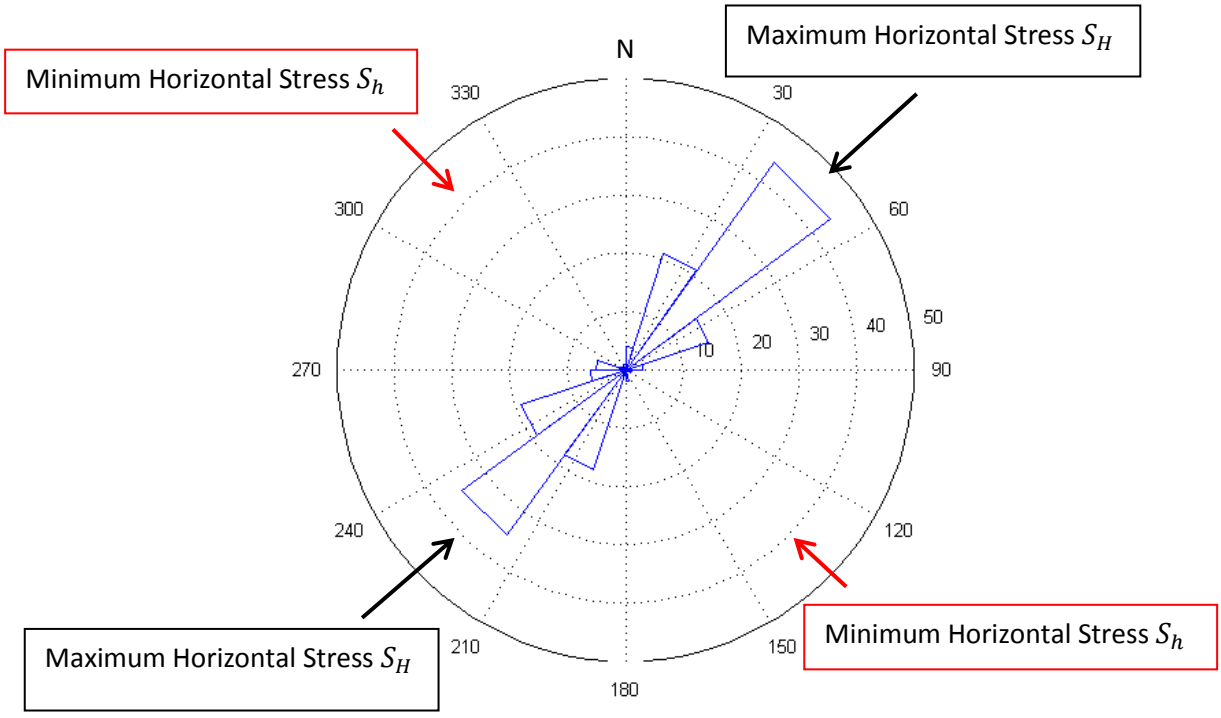

Figure 4.13: Statistical Rose diagram of the all the azimuths of the DITF. The black lines are the direction of maximum horizontal stress and orthogonal to this is the inferred minimum horizontal stress

The mean azimuth calculations are preformed the same but the mean azimuth, equation (*4.4)* is scaled down by a factor of 2 becoming:

$$x_o = \frac{1}{2}\arctan\left(\frac{S}{C}\right). \qquad (4.10)$$

The appropriate measure for the circular variance, $\tilde{S}_o$, then becomes:

$$\tilde{S}_o = 1 - (1 - \grave{S}_o)^{\frac{1}{4}}. \qquad (4.11)$$

Where above $\grave{S}_o$ is the circular variance of the double angled data θ_i^*. Then by using equation *(4.6)* setting *l=2* we calculate the standard deviation S_{std} of the DITF data. From the azimuths of the DITF it was determined that the direction of maximum horizontal stress is directed towards the NE-SW direction at 50°NE (with circular standard deviation 9°). It can be seen from the well specific rose diagrams in Table 4 and the composite rose diagram using all of these orientations together (Figure 4.13) that there is a strong NE-SW trend of the fractures in the study area. Furthermore, since the maximum and minimum horizontal stresses are orthogonal to each other, the minimum horizontal stress, S_h, is oriented in the NW-SE direction at 140°SE.

4.5. Quantitative Constraint on Stress Magnitudes

Knowledge of the stress directions is a first step in understanding the underground state of stress, but a fuller appreciation can only be gained if the stress magnitudes and fluid pressures can be found. Having such information allows practitioners to maximize development of the resources and to assess geological hazards. A good example of such an application was the analysis by Horner et al, (1994) of a series of induced earthquakes in the Fort St. John locale of NE British Columbia. In some cases, for example, slip on pre-existing planes of weakness have resulted in catastrophic release from a steam zone at the Jocelyn Creek SAGD Thermal Operation (ERCB 2010), casing failures at Imperial Oil's Cold Lake thermal operations (Smith, 2010) and flow of bitumen to the surface at the CNRL Primrose thermal project (Alberta Energy Regulator, 2016). All of these events have substantial economic and social license costs; consequently, it is important that the stress state be evaluated as completely as possible in order to reduce the risks associated with production of bitumen by in situ processes.

Unfortunately, no direct stress measurements were made at the Saleski project. However, as just noted there are abundant drilling induced tensile fractures. Just as importantly, there were no

observable borehole breakouts. Here, we use this information to constrain the magnitudes of the horizontal stresses. To do this we will return to the equations for stress concentration by the borehole as introduced in Chapter 2.

This section focuses on constraining stress magnitude ranges based off of the well logs, fracture analyses and the characterization of fractures in the image logs. The pore pressures P_P within the formation are estimated from a number of drill stem tests carried out at the site. The vertical stress magnitude is calculated from density logs. We then use the fact that there are extensive drilling induced tensile fractures but an absence of borehole breakouts to quantitatively constrain the ranges of allowable minimum S_h and maximum S_H horizontal stresses.

4.5.1. Estimation of Pore Fluid Pressure and Vertical Stress

Another important aspect of the stress of the formation is the formation fluid pressure or pore-pressure. As discussed in Chapter 2, this is the pressure of the fluid inside the pores of the rock acting outwards and actively lowers the normal stresses affecting the rock.

The most common method in which to measure pore-pressure is preforming a drill-stem test (DST). A DST is performed in three major periods and pressure is measured against time (as seen in Figure 4.14). These consist of:

1. Run-in Period: the tool is run into the hole to the depth of interest. The borehole fluid (drilling mud) is allowed to flow through the tool and the pressure allowed to equilibrate. This provides a measure of the pressure of the mud column P_w at that depth (point 1, Figure 4.14).
2. Interval Isolation: The tool's packers are then inflated against the borehole wall to isolate an interval along the borehole. Fluid is then pumped out of this interval to lower the pressure and allow formation fluids to flow from the formation into the interval. (points 2-3, Figure 4.14).
3. Shut In: Next the shut-in period occurs where a valve to the interval is then closed while the formation fluids continue to flow into the interval. This continues with the interval pressure building gradually until it reaches an equilibrium (points 3-4, Figure 4.14). This provides a measure of the formation pore pressure P_p.

4. The subsequent processes of flow periods and shut-in periods are repeated over a longer period of time in order to check reservoir productivity (points 5-7, Figure 4.14). The final pressure of the mud column (point 8, Figure 4.14) is checked to match the initial pressure (point 1, Figure 4.14) to check the tools accuracy or if there was leaking through the packers. Thus the pore-pressure of the formation is measured at the equilibrium points during the shut in pressure (points 4 and 7, Figure 4.14).

Our dataset included one DST in well 10-32-085-19W4 north of the study area and from the pore pressures at both points 4 and 7 were 1034 kPa and 1093 kPa respectively. Therefore, we infer the pore pressure to be 1063 kPa. Unfortunately no FMI data was included at this well.

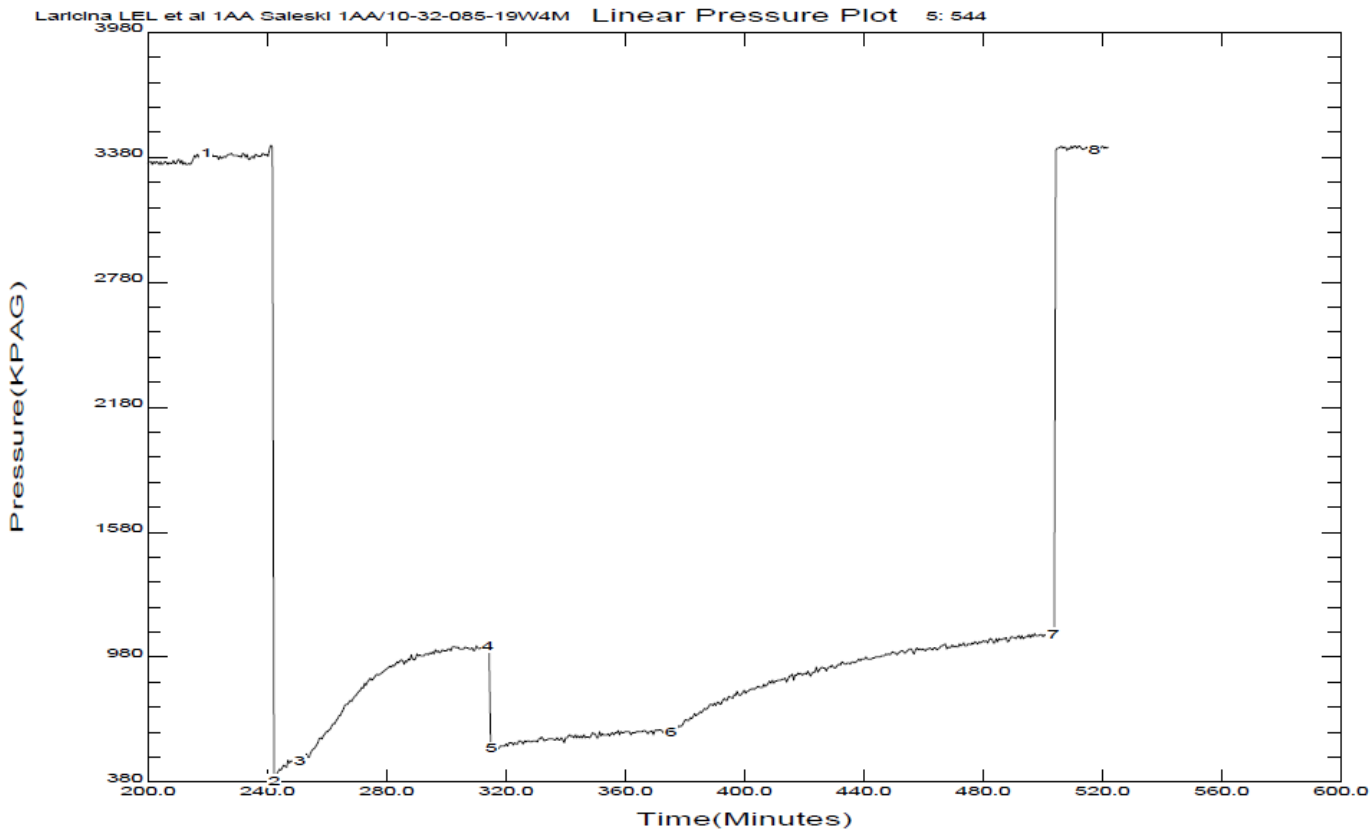

Figure 4.14: Drill Stem Test ran at depth of 350m initially corresponding to 3m above the prognosis of Grosmont D top. But is actually 20m above the 369m Grosmont D top picked from well logs. The pore pressure is estimated to be 1063KPa from the shut-in periods shown at points 4 and 7. Values are listed in Table 5 below.

Point	Description	Pressure [KPa]	Time [min]
1	Initial Mud Column Pressure	3399	242
2	Flow Period	388	242
3	Initial Shut-in 1	481	255
4	Final Shut-in 1	**1034**	315
5	Flow Period	544	315
6	Initial Shut-in 2	622	380
7	Final Shut-in 2	**1093**	505
8	Final Mud Column Pressure	3419	505

Table 5: DST data of Figure 4.14 displaying time each period commenced and the corresponding pressure measured from tool. The pore pressure is measured to be 1063KPa from final shut-in periods 4 and 7.

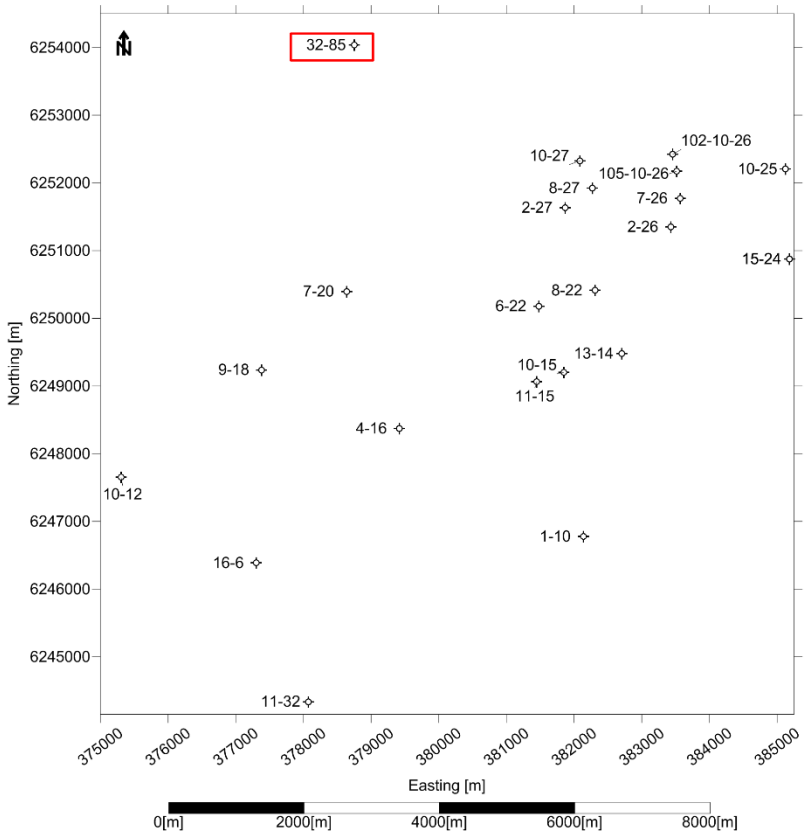

Figure 4.15: Modified map of wells in study area. Well 10-32-085-19W4 shown in red box slightly North of study area. The well contained no FMI data.

4.5.2. Estimation of the Vertical Stress S_V and Wellbore Pressure

As discussed earlier in Chapter 2, the magnitude of the vertical stress is generally assumed to be equal a pressure induced by the weight of the overlying sediments according to

$$S_v(z) = \int_0^z \rho(z) g \, dz \qquad (4.12)$$

and that it is also a principal stress. This is done by iteratively summing the density values given by the density logs multiplied by gravity and by the depth step at which the different logs recorded each sample at. Density logs and vertical stress curves can be seen below in Figure 4.16.

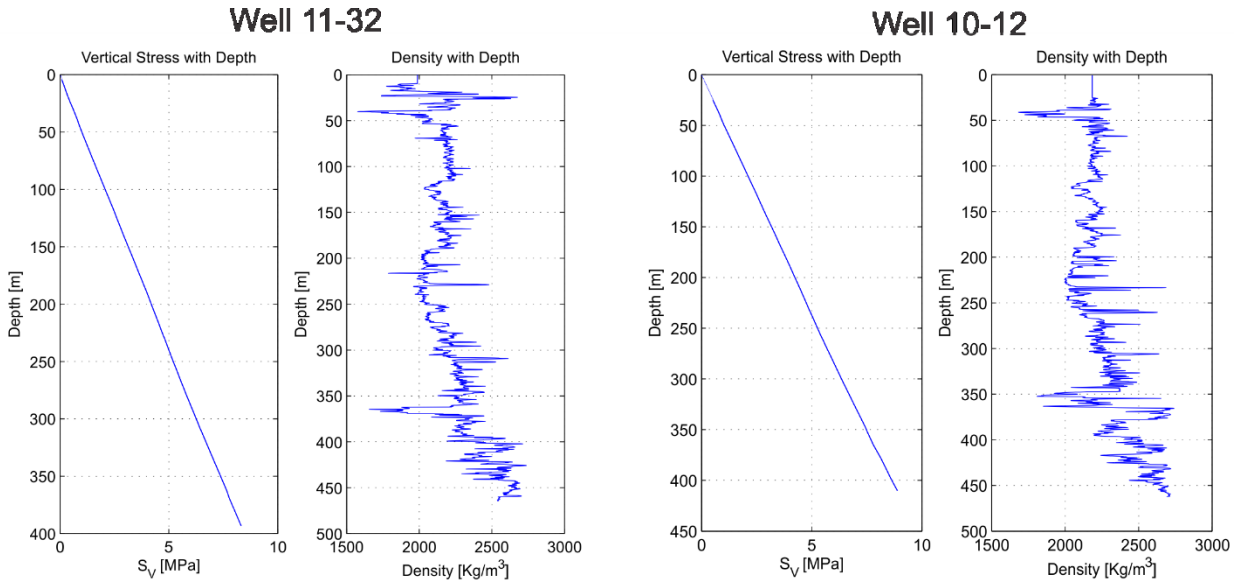

Figure 4.16: Vertical stresses and density logs with depth of wells 11-32 and 10-12. Image shows vertical stresses at tops of Grosmont D units located at 393m and 410m with values of vertical stress of 8.80 MPa and 9.79 MPa respectively. The first density data point was backward continued until surface.

The density curves were backward continued from the first density data point until surface. This will add some error to the vertical stress calculations as near surface sediments tend to be lower density, however, we feel this won't significantly affect the values of stress values. Additionally, we are fortunate that the dataset contains such near surface measurements of density as most logs will be more targeted to zones of interest. The average S_V gradients in the study area to the Grosmont C and D formations was 21 KPa/m. The results the S_V calculations are given at the tops to the Grosmont C and D units in Table 6.

Wellbore pressure P_w is calculated the same way except the density of the drilling mud is constant with depth simplifying equation *(4.9)* to:

$$P_w = \rho_{mud} g \Delta z, \qquad (4.13)$$

where ρ_{mud} was most commonly a 'kim mud' of density 1140 kg/m^3 and Δz is the depth to the formation. For a well at the average Grosmont D depth of 353m the wellbore pressure was $P_w =$ 3.9 MPa. We use this value in Chapter 4.8 for bounding stresses.

Well ID	Elevation [m]	Depth Grosmont D [m]	Depth Grosmont C [m]	Vertical Stress Grosmont D [MPa]	Vertical Stress Grosmont C [MPa]
1-10-85-19W4	580	362	388	7.50	8.12
2-26-85-19W4	580	333	365	7.19	7.96
4-16-85-19W4	589	369	403	7.94	8.77
7-20-085-19W4	600	370	404	7.97	8.79
8-27-85-19W4	607	340	374	7.02	7.83
9-18-85-19W4	595	388	413	8.20	8.81
10-12-85-20W4	598	410	445	8.91	9.78
10-15-85-19W4	603	358	413	7.93	9.20
10-25-85-19W4	593	308	339	6.41	7.16
11-15-85-19W4	568	354	393	7.48	8.41
11-32-84-19W4	594	393	425	8.32	9.09
13-14-85-19W4	588	347	377	7.63	8.34
15-24-85-19W4	589	307	338	6.69	7.44
16-6-85-19W4	567	388	421	8.20	9.01
10-32-085-19W4	608	369	400	8.33	8.84
100-2-27-85-19W4	597	348	379	7.61	8.36
100-6-22-85-19W4	571	357	390	7.78	8.43
100-8-22-85-19W4	590	351	383	7.29	8.07
100-10-27-85-19W4	584	341	372	7.42	8.16
102-7-26-85-19W4	584	336	361	6.86	7.45
102-10-26-85-19W4	569	324	358	6.75	7.57
105-10-26-85-19W4	584	325	359	6.97	7.79

Table 6: The well depth with vertical stresses resulting from the density integration from equation (4.12). The vertical stresses are calculated to the tops of reservoir formations Grosmont C and D. All the wells are vertical so no corrections needed to be applied as the well deviation surveys for all wells are under 1°. The average vertical stresses are 7.53 and 8.31 MPa at the Grosmont D and C formations respectively.

4.6. Constraints on Horizontal Stress Magnitudes

In this section, we place constraints on the allowable values of the allowable range of the magnitudes of the horizontal principal stresses based on the existence of DITF and the lack of borehole breakouts. The borehole cavity concentrates pre-existing stresses around the borehole as

already discussed in Chapter 2. Assuming that the borehole is vertical, that the vertical stress is principal, and that the maximum and minimum horizontal principal compressions are respectively S_H and S_h, the 2-D expressions for the concentrated azimuthal and radial stresses can be expressed as (Schmitt et al. 2012):

$$\sigma_{\theta\theta} = \frac{S_H + S_h}{2}\left(1 + \frac{a^2}{r^2}\right) - \frac{S_H - S_h}{2}\left(1 + \frac{3a^4}{r^4}\right)\cos(2\theta) \quad (4.14)$$

$$\sigma_{rr} = \frac{S_H + S_h}{2}\left(1 - \frac{a^2}{r^2}\right) + \frac{S_H - S_h}{2}\left(1 + \frac{3a^4}{r^4} - \frac{4a^2}{r^2}\right)\cos(2\theta), \quad (4.15)$$

where $\sigma_{\theta\theta}$ is the azimuthal hoop stress, σ_{rr} is the radial stress, a is the borehole radius, r is the distance from the borehole axis θ is the azimuth measured from the x-axis that is parallel to the direction of S_H. For the purpose of studying stress features occurring on the borehole wall (setting $r = a$), the azimuthal stress (equation (*4.14)*) reduces to simply:

$$\sigma_{\theta\theta,0} = 3S_h - S_H \quad (4.16)$$

in the direction of maximum principal horizontal stress S_H at $\theta =$ 0° and 180° and

$$\sigma_{\theta\theta,90} = 3S_H - S_h \quad (4.17)$$

in the direction of minimum principal horizontal stress S_h at $\theta =$ 90° and 270° Further, at the borehole wall it's easily seen that the radial stress vanishes ($a=r$ equation *(4.15)*).

$$\sigma_{rr} = 0 \quad (4.18)$$

However, in a real borehole we must also consider the effects of the pressure of the drilling mud in the borehole during drilling. The drilling mud pressure, P_w, can be calculated by simply integrating the borehole drilling mud density with depth. The drilling mud pressure acting on the borehole wall adds a tensile hoop stress and compressive radial stress. Adding the effect of the drilling mud pressure, P_w, equations *(4.16)-(4.18)* at the borehole wall reduce to

$$\sigma_{rr} = P_w\,, \quad (4.19)$$

$$\sigma_{\theta\theta,0} = 3S_h - S_H - P_w \quad (4.20)$$

and

$$\sigma_{\theta\theta,90} = 3S_H - S_h - P_w. \quad (4.21)$$

Examination of these expressions show that $\sigma_{\theta\theta,\,90} > \sigma_{\theta\theta,\,0}$ meaning that the stress first becomes tensile at azimuths $\theta = 0°$ and 180°; and DITF's will be found at these azimuths. Further, if a DITF exists, the concentrated azimuthal stress at the borehole wall must overcome the rock's tensile strength T_o such that a tensile fracture is created at the borehole wall, this may be expressed as:

$$\sigma_{\theta\theta,break} \leq -T_o \,. \qquad (4.22)$$

if there is no pore pressure P_P.

The existence of DITF in the log data affirms that there are areas in the subsurface where the hoop stress is less than the tensile strength of the rock causing tensile fracturing to occur. This is satisfied when:

$$S_H + P_w - 3S_h \geq T_o \qquad (4.23)$$

but with consideration of the pore pressure P_P and the Terzhaghi effective stress (that is equivalent to reducing the tensile strength)

$$S_H + P_w - 3S_h \geq T_o - P_P \qquad (4.24)$$

which may be rewritten in the form of a constraint that a drilling induced tensile fracture exists under the condition that

$$S_H + P_w - 3S_h + P_P \geq T_o \qquad (4.25)$$

where we note that the pore pressure promotes failure.

In Figure 4.17a the value of the left hand side of equation *(4.25)* is represented by color within the S_H-S_h space for P_w = 3.9 MPa and P_P = 1MPa. It is then possible to bound combinations of horizontal stresses at a set P_w by plotting a tensile strength overtop of the borehole hoop stress at the direction of maximum horizontal stress in S_H-S_h space as shown in Figure (*4.17a)*. [Note that the dark blue on the right side of the image is an area manually filled with dark blue where S_H<S_h, which cannot exist by definition].

The white contours on the plots of Figure *(4.17a)* provide boundaries for the regions in S_H-S_h space in which the drilling induced tensile fractures are allowed or disallowed. Each contour is for an assumed value of 0 MPa, 5 MPa, or 10 MPa that cover the expected range of values of the rock tensile strength. Anywhere left and above the tensile strength contours is an area of combinations

of S_H and S_h where the rock could experience tensile failure and thus DITF would appear on the image logs. DITF's cannot occur to the right of the white lines as generally the hoop stress is everywhere in compression.

Conversely, borehole breakouts occur when stresses at the borehole wall and the borehole pressure concentrate such that the hoop stress exceeds what is needed to cause compressive shear failure of the rock (Bell & Gough 1979). Following a similar line or reasoning as done for constraint with the DITF we return to the state of stress that would be expected for an incipient borehole breakout of negligible width on the borehole wall at 90° (and 270°) to the direction of S_H leading from equation *(4.21)* including the wellbore pressure P_w

$$\sigma_{\theta\theta,90} = 3S_H - S_h - P_w. \qquad (4.26)$$

Since we assume the borehole breakout is formed by shear failure at the borehole wall then the hoop stress $\sigma_{\theta\theta,90}$ may be compared to the load σ_1 in the discussion of Mohr-Coulumb failure criterion described Chapter 2 (Figure 2.15) with the 'lateral' confining stress equal to the load of P_w at the same point on the borehole wall. Recalling from Chapter 2 that the linear Mohr-Coulomb failure criteria is given by:

$$\sigma_1 = \frac{2C\cos(\emptyset)}{1-\sin(\emptyset)} + \frac{1+\sin(\emptyset)}{1-\sin(\emptyset)}\sigma_3 . \qquad (4.27)$$

which upon substitution and rearrangement neglecting pore pressure and considering this as an inequality

$$3S_H - S_h - P_w \geq \frac{2C\cos(\phi)}{1-\sin(\phi)} + \frac{1+\sin(\phi)}{1-\sin(\phi)} P_w \qquad (4.28)$$

or

$$3S_H - S_h - \frac{2}{1-\sin(\phi)} P_w \geq \frac{2C\cos(\phi)}{1-\sin(\phi)} . \qquad (4.29)$$

The role of pore pressure in cannot be ignored and when this is included through the Terzhaghi effective stress law we have

$$(3S_H - S_h - P_w) - P_P \geq \frac{2C\cos(\phi)}{1-\sin(\phi)} + \frac{1+\sin(\phi)}{1-\sin(\phi)}(P_w - P_P) \qquad (4.30)$$

or

$$3S_H - S_h - \frac{2}{1-\sin(\phi)}P_w + \frac{2\sin(\phi)}{1-\sin(\phi)}P_P \geq \frac{2C\cos(\phi)}{1-\sin(\phi)} \qquad (4.31)$$

We expect incipient shear failure to occur once this condition exists, that is once the value of the left-hand side of equation *(4.31)* exceeds the right-hand side then a borehole breakout is expected. Alternatively, if there is no breakout then the left-hand side should not exceed the right; and as no borehole breakouts are observed this too provides an additional bound on the stresses possible.

One problem with this equation *(4.31)* is that it requires some knowledge of the rock strength through the cohesion *C* and the internal friction angle ϕ. Walton (2014) performed a series of tri-axial stress tests on carbonate rocks to investigate the stress-strain relationship and obtain information of their strength parameters. For each carbonate sample, he brought the confining and axial stresses to that which would cause rock failure to the sample and he fit a Mohr-Coulomb strength envelope to the set of his observed failure strengths using least squares regression. The model fit (equation *(4.27)*) relates the greatest compressive stress σ_1 will be during rock shear failure given: the lowest principle stress σ_3, the rock cohesion *C [MPa]* and the internal friction angle ϕ *[°]*. His final values for these fits are given in Table 7.

Therefore, substituting P_w for the lowest stress σ_3, and using cohesion and friction angle values modelled for Walton et al's (2015) Toral de Los Vados limestone, Indiana Limestone and Carrara Marble carbonates, the value of σ_1 needed for shear failure can be estimated. Next the values where shear failure could occur are plotted on top of the borehole hoop stress at the direction of minimum horizontal stress in S_H-S_h space. Any combination of S_H and S_h that form the hoop stress above the shear failure line have the potential for borehole breakouts to occur and likewise any values below represent stable conditions with no breakouts allowed. Since there are no

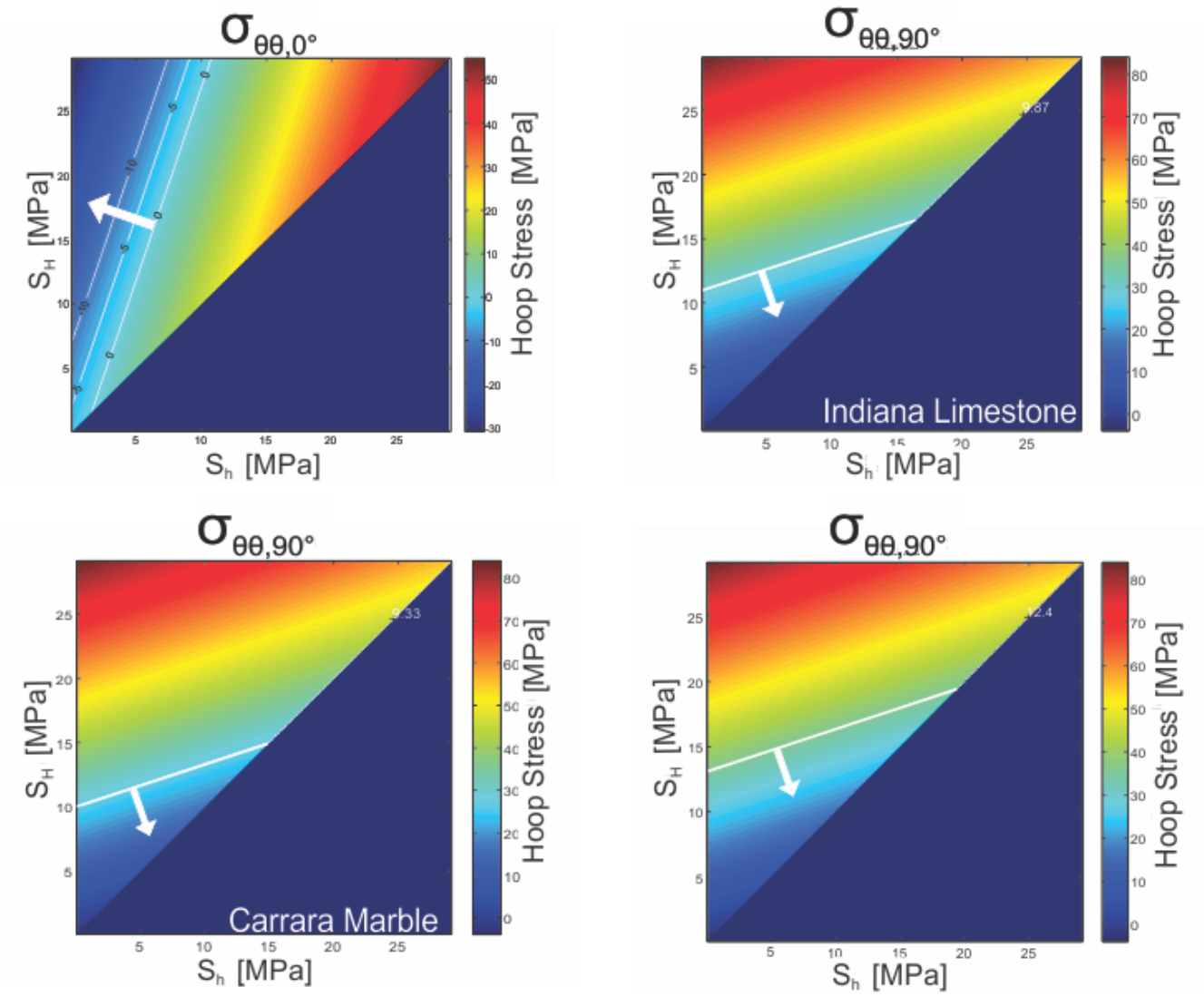

Figure 4.17:a) Image of the color coded magnitude of the hoop stress $\sigma_{\theta\theta}$ calculated at the borehole wall in the direction of S_H using equation (4.25) For DITF's to occur, given a certain tensile rock strength (white lines units of MPa for values of 0 MPa, 5 MPa, and 10 MPa), the combination of horizontal stresses must be located on the left of the white tensile strength contours given by the arrow. The regions to the right of the white lines are generally in compression and the rock cannot fail in tension to produce a DITF. Pore pressure and wellbore pressures used were 1 MPa and 3.9 MPa respectively. a-d) Image of the color coded magnitude of the hoop stress $\sigma_{\theta\theta}$ calculated at the borehole wall in the direction 90° from S_H using equation (4.31)

Rock	Friction Angle ϕ [°]	Cohesion C [MPa]	Wellbore Pressure P_W [MPa]	Pore Pressure P_p [MPa]	S_H Bounds [MPa]	S_h Bounds [MPa]
Indiana Limestone	48.4	1.2	3.9	1	12.5	5.8
Carrara Marble	46.2	1.3	3.9	1	11.6	5.4
Toral de Los Vados Limestone	46.2	3.1	3.9	1	15.0	6.6

Table 7: Final values of Walton (2014) modeled laboratory measurements of friction angle and cohesion for Indiana Limestone, Carrara Marble and Toral de Los Vados Limestone and horizontal stress bounds from Figure 4.18.

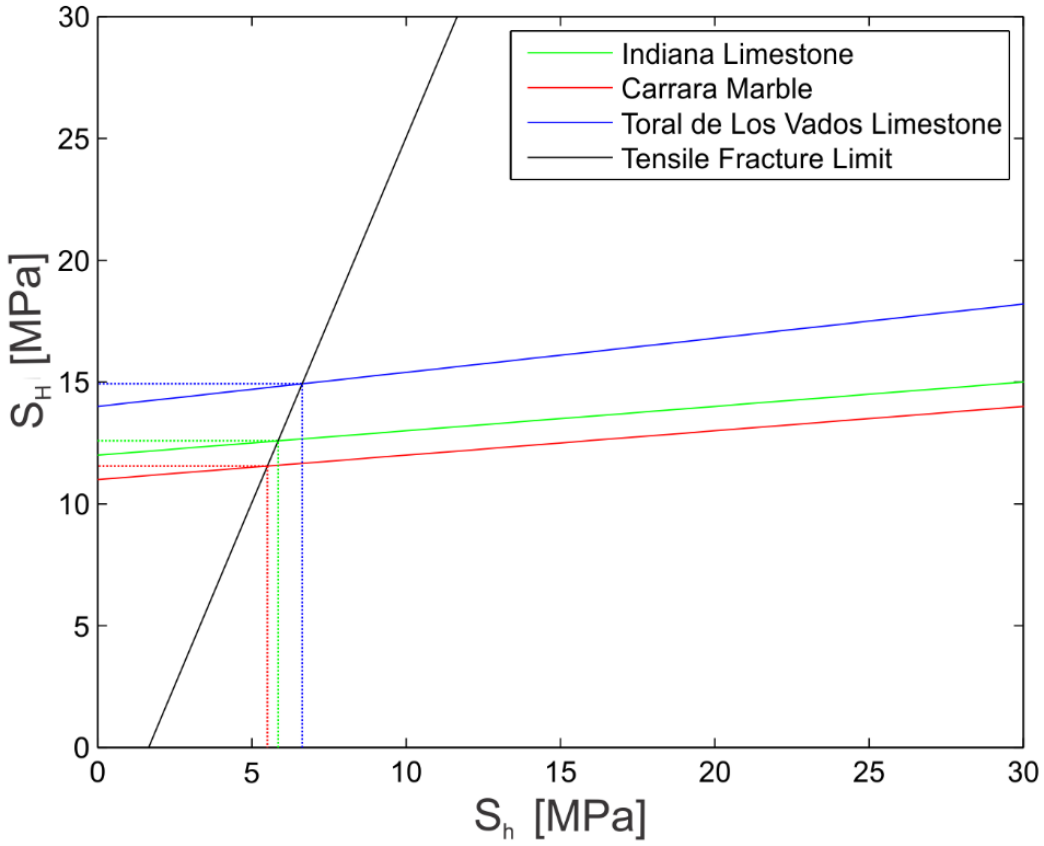

Figure 4.18: A diagram of the derived allowable horizontal stresses with the tensile fracture limit. In this illustration the tensile strength of the rock is taken to be 0 MPa. The tensile fracture limit (black line) marks the boundary at which the stresses are constrained. Where the modelled strength (colored lines) intersect the tensile fracture limit mark the maximum corresponding stress before borehole breakouts would occur. Data summarized in Table 7.

Therefore, by plotting the allowable horizontal stress states with the tensile fracture limit (Figure 4.18) of the rock, the horizontal stresses in the area are bound from the stress features logged. The maximum allowable horizontal stresses at the Grosmont depth for maximum horizontal stress are $11.6\,MPa < S_H < 15.0\,MPa$ and for minimum horizontal stress are $5.4\,MPa < S_h < 6.6\,MPa$. The average vertical stresses in all the boreholes are 7.53 and 8.31 MPa for Grosmont formations C and D respectively (Table 6). Further this suggests that the area is located in a strike slip environment ($S_h < S_V < S_H$). This information is summarized in Table 7 above.

4.7. Stability of Existing Fractures

The need for stress measurements in light of risk of motion on pre-existing faults was mentioned in Section 4.3. Once this information is obtained, it is then possible to evaluate whether the joints and faults at a given area are stable or not. Here we are fortunate to have an exceptional data base of both fractures statistics within the Grosmont formation as well as constraints on the magnitudes of the state of stress in the area, and this allows us to carry out such an analysis at the Saleski project site.

Some examples of applications of these concepts in Western Canada may be found in studies of felt induced seismicity near Rocky Mountain House by Baranova et al, (1999) and Fort St. John, British Columbia by Horner et al, (1994) and a risk analysis for fault stability during geothermal operations in the Granite Wash Formation near Peach River, Alberta by Weides et al (2014). The basic concepts underlying these fault stability analyses follow from Morris et al. (1996) who developed an early interactive program to quantitatively assess the stability of faults in a given stress state. These ideas have now been applied by many authors (e.g. Moeck et al. 2009).

The essential idea, recently reviewed by Schmitt (2016), is that a pre-existing planar fault or fracture will 'slip' once shear stress τ resolved into the fracture plane overcomes the friction μ along it and the its resolved normal stress σ. In other words, once the shear stress in the plane becomes too high relative to the other forces constraining it then the fracture or fault will move. The Coulomb frictional criterion may again be applied such that the fracture is stable as long as:

$$\tau < C + \mu(\sigma - P_p), \qquad (4.32)$$

where τ is the shear stress acting within the fracture plane, C is the cohesion, μ is the coefficient of friction, σ is the normal stress acting on the fracture plane, and P_p is the pore pressure. A simple rearrangement of equation *(4.32)* leaves criterion for slip or instability.

$$0 > C + \mu(\sigma - P_p) - \tau \qquad (4.33)$$

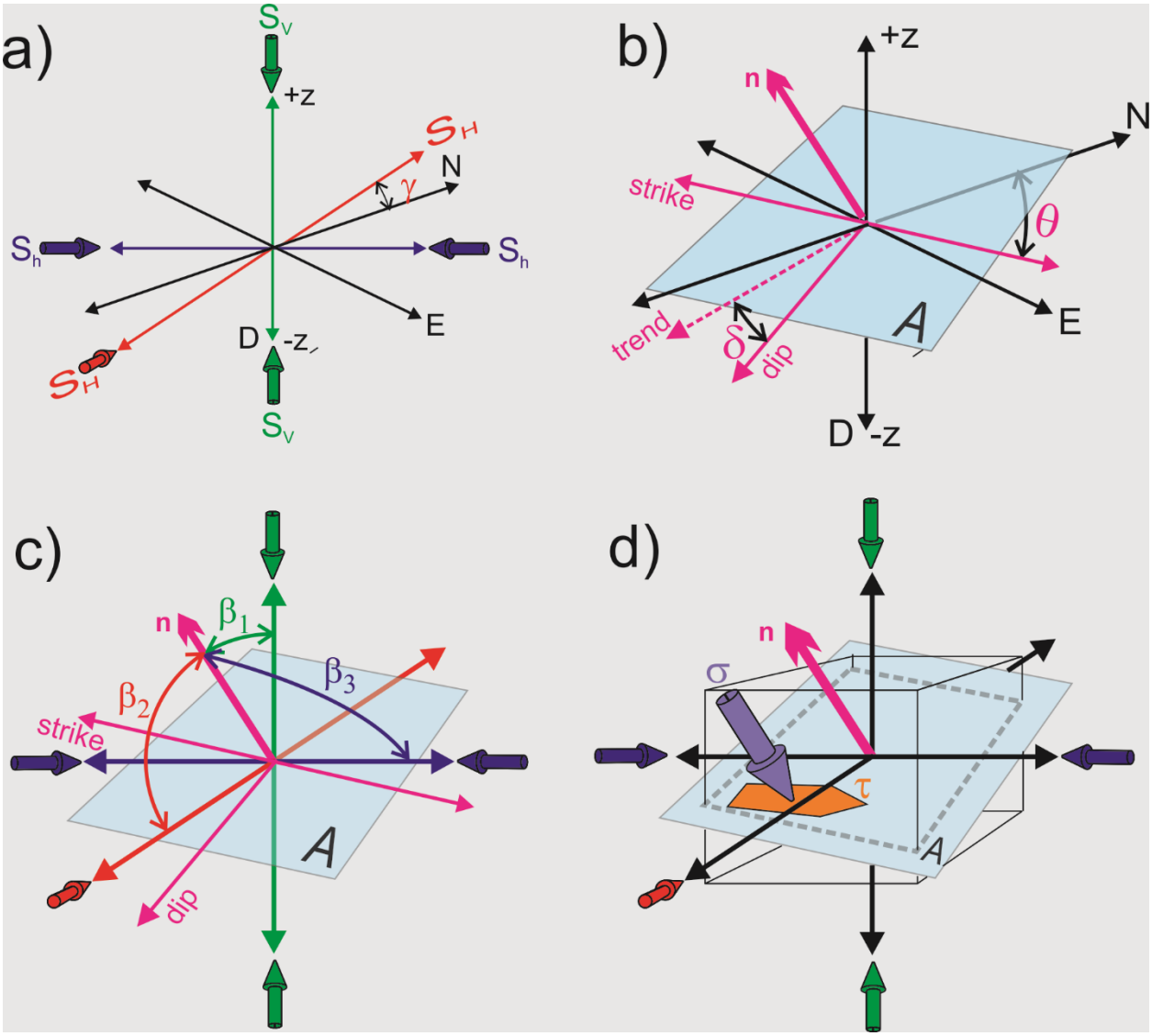

Figure 4.19: Coordinate systems and geometry of plane with principal stresses. a) The coordinate systems of the principal stresses S_H, S_h and S_V with the geographic North-East-Down system. Figures b) & c) define strike dip and trend of the plane as well as angles between the principal stresses and geographic coordinates. d) The plane with normal vector n with the normal and shear stress vectors acting on it.

This seems like a fairly straightforward concept as it relies on well accepted frictional theory. However there are a number of details to mention, and begin by considering a fracture plane defined by its strike θ and dip δ (Figure 4.19b) existing within a given state of principal stresses [S_V, S_H, S_h] with S_H at azimuth γ (Figure 4.19a). The orientation of the fracture may also be described by the vector ***n*** that is normal to its plane, this is the same as the 'poles' to the fracture planes above (Fig. 4.19b). The relative orientations of the stresses and the fracture is represented by three angles β_1, β_2, and β_3 of the between the directions of S_V, S_H, *and* S_h, respectively. With reference to Figure 4.19d this geometry $\sigma(\theta,\delta)$ and $\tau(\theta,\delta)$ can be written:

$$\sigma = S_V(\cos\beta_1)^2 + S_H(\cos\beta_2)^2 + S_h(\cos\beta_3)^2 \qquad (4.34)$$

$$\tau = \sqrt{S_V^2(\cos\beta_1)^2 + S_H^2(\cos\beta_2)^2 + S_h^2(\cos\beta_3)^2 - \sigma^2} \quad . \qquad (4.35)$$

With this theoretical background and with the knowledge of a representative state of stress derived from Table 7 of S_V = 7.53 MPa, S_H = 15.0 MPa, S_h = 5.4 MPa we calculate the total normal $\sigma(\theta,\delta)$ and shear $\tau(\theta,\delta)$ stresses resolved onto the complete possible ranges for fracture azimuths $0 \leq \theta \leq 360°$ and dips $0 \leq \delta \leq 90°$ in equal angle stereographic projections (Figure 4.20). This shows that the greatest shear stresses of about 5 MPa are resolved onto the conjugate set of planes with strikes θ of ~5° and 275°.

As discussed earlier in Chapter 2, we know that friction on the fracture surfaces shifts the orientation of the most likely planes to slip towards the direction of the greatest compression that in this case will be S_H. Hence one can use equation *(4.33)* to test whether any given arbitrarily oriented fracture with orientation (θ,δ) will be stable by simply inputting appropriate choices for the cohesion C, friction μ, and pore pressure P_P together with the values of $\sigma(\theta,\delta)$ and $\tau(\theta,\delta)$.

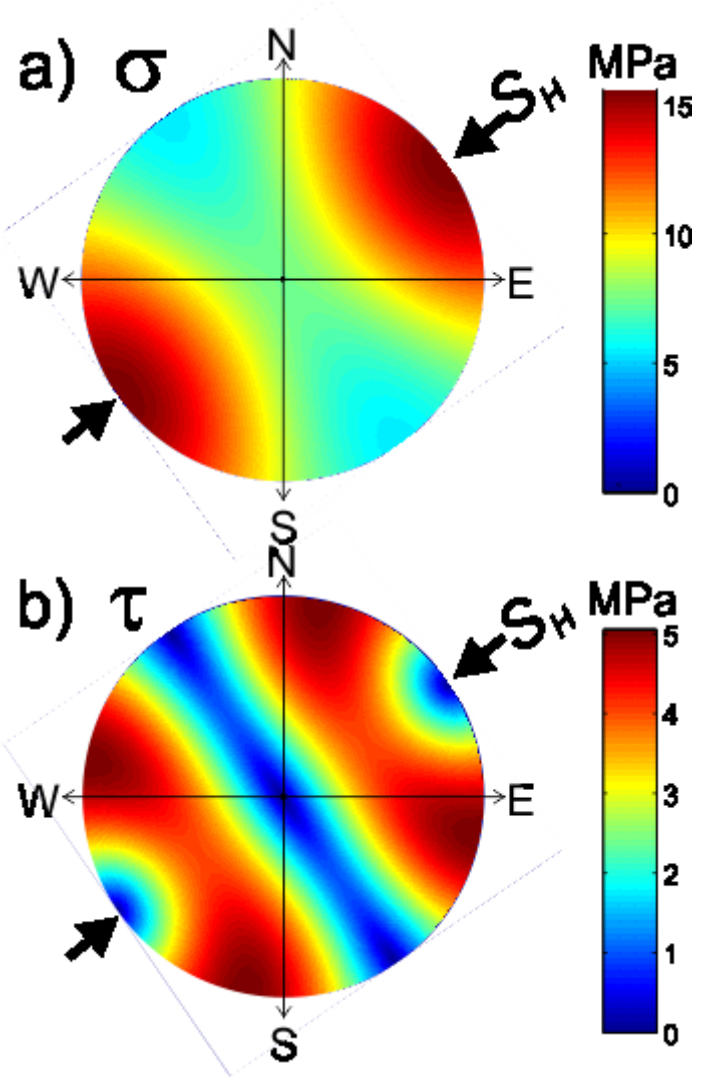

Figure 4.20: a) Lower hemisphere stereonet projection of all possible dip directions and dips of normal vectors to planes. Each point shows normal stress acting on the plane. Plot is viewed with increasing dip inward (normal vector of plane has 0° dip at outside of circle). Hotter colours represent greater compressions b) Shows the same stereonet projection but the shear stresses are plotted instead of normal stresses. Hotter colors represent greater shear stress in the plane of the fracture. Note that S_H is directed at azimuth 50°.

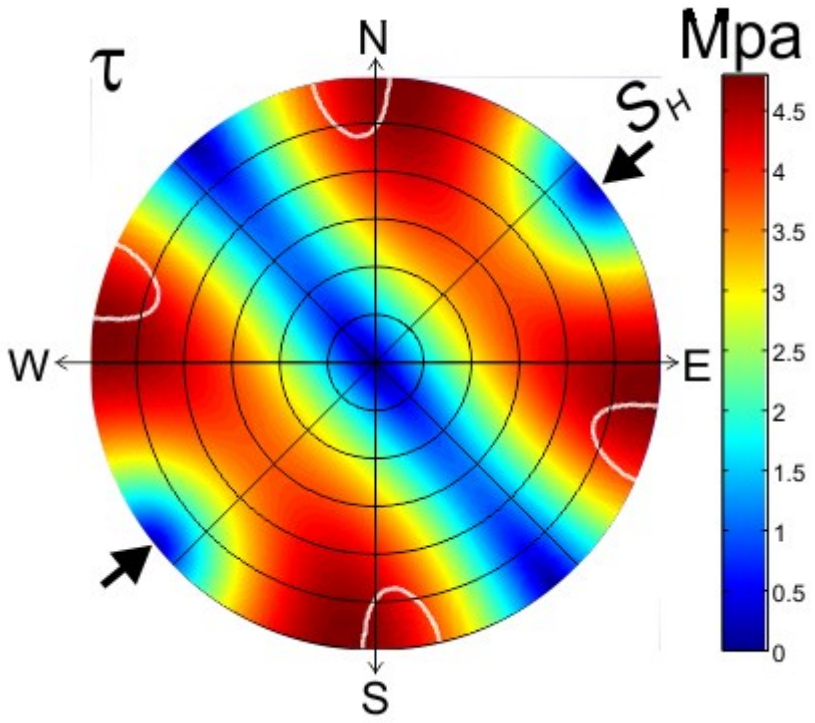

Figure 4.19: Stereonet projection of shear stresses acting on all set of dip azimuth/strike and dip of planes with area of instability contour in white. The inputs used for this model were: $S_H = 15.0\ [MPa]$, $S_h = 5.4\ [MPa]$, $S_V = 7.53\ [MPa]$, $P_p = 1\ [MPa]$, $c = 1.3\ [MPa]$, $\mu = 0.4$.

Displayed inside the white contours in Figure 4.21 are the orientations of fracture planes most likely to slip. The direction of the maximum horizontal stress S_H was determined from our analysis of the azimuths of the drilling induced tensile fractures in Chapter 4.4 and is 50°NE with circular standard deviation of 9°. Therefore, the orientations of fractures most likely to slip with these stresses and model inputs are just beyond 45-70° to offset of S_H. The vertical stress and pore pressure values are appropriate for the Grosmont D unit.

We have bounded the possible values of horizontal and stresses used for input values, calculated the vertical stress from density logs and used DST data to obtain the pore pressure of the formation. Some note should be given to the coefficient of friction, μ. Data collected by Byerlee (1978) shows that for low overburden pressure (< 200MPa) a good estimate for the friction coefficient is $\mu \cong 0.8$. However this is not the case for all shallow environments and some experimental shear experiments of carbonate rock testing has been done by Scuderi et al, (2013) to investigate frictional properties for in-situ core and outcrop dolomites. The measured coefficients of friction as a function of normal stresses on layered powdered fluid saturated samples at 75°C in and room temperature dry cases. At elevated temperature under fluid saturated conditions their resulting

friction values vary from 0.45 to 0.75. Under dry conditions at room temperature their friction range does not vary with normal stress with μ varying from 0.6-0.7.

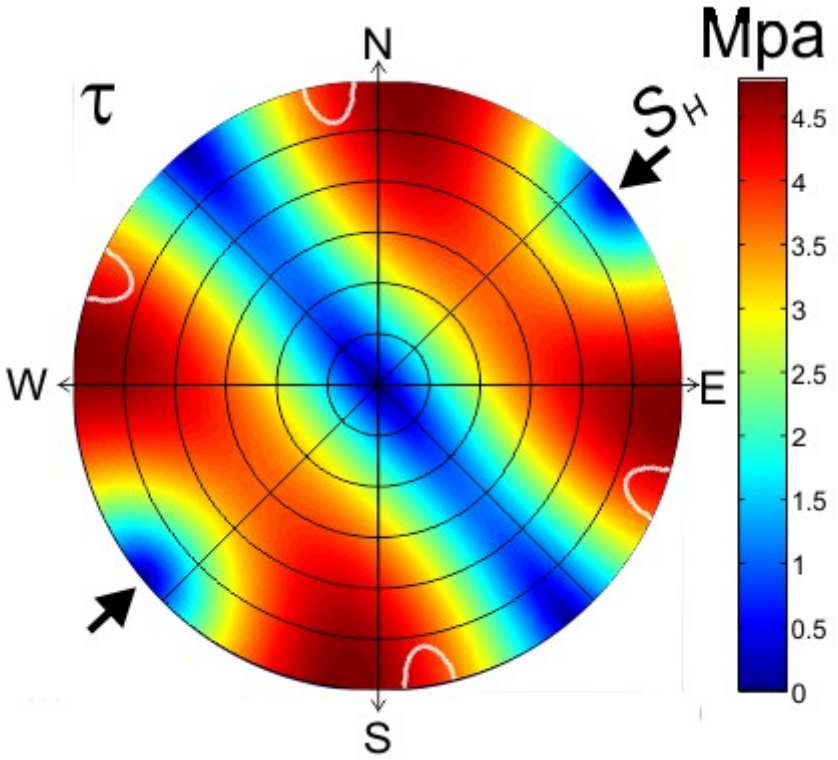

Figure 4.20: Stereonet projection of shear stresses acting on all set of dip azimuth/strike and dip of planes with area of instability contour in white. The inputs used for this model were: $S_H = 15.0\ [MPa]$, $S_h = 5.4\ [MPa]$, $S_V = 7.53\ [MPa]$, $P_p = 1\ [MPa]$, $c = 0\ [MPa]$, $\mu = 0.6$.

If we assume zero cohesion and input a higher coefficient of friction the model's orientation for zones of instability are very similar; that is, that the zones of slip maintain a 45-70° offset from the maximum horizontal stress however the area of instability is smaller. Therefore, the zones of instability maintain their orientation and only differ in dip angle depending on the true frictional and the cohesive properties. The reader should note that these models are a simplification of the true interaction of stresses, cohesive and frictional forces occurring in the Grosmont and for a more robust model we would require lab testing of Grosmont core for its bitumen saturated coefficient of friction and tri-axial strength testing for internal friction angles for stress constraint. We can

now compare the fracture poles and Kamb contouring with the zones of stability in the model seen in Figure 4.23. We can see that the majority of fractures lie in the stable zone. This is most likely due to the low pore pressure of the reservoir.

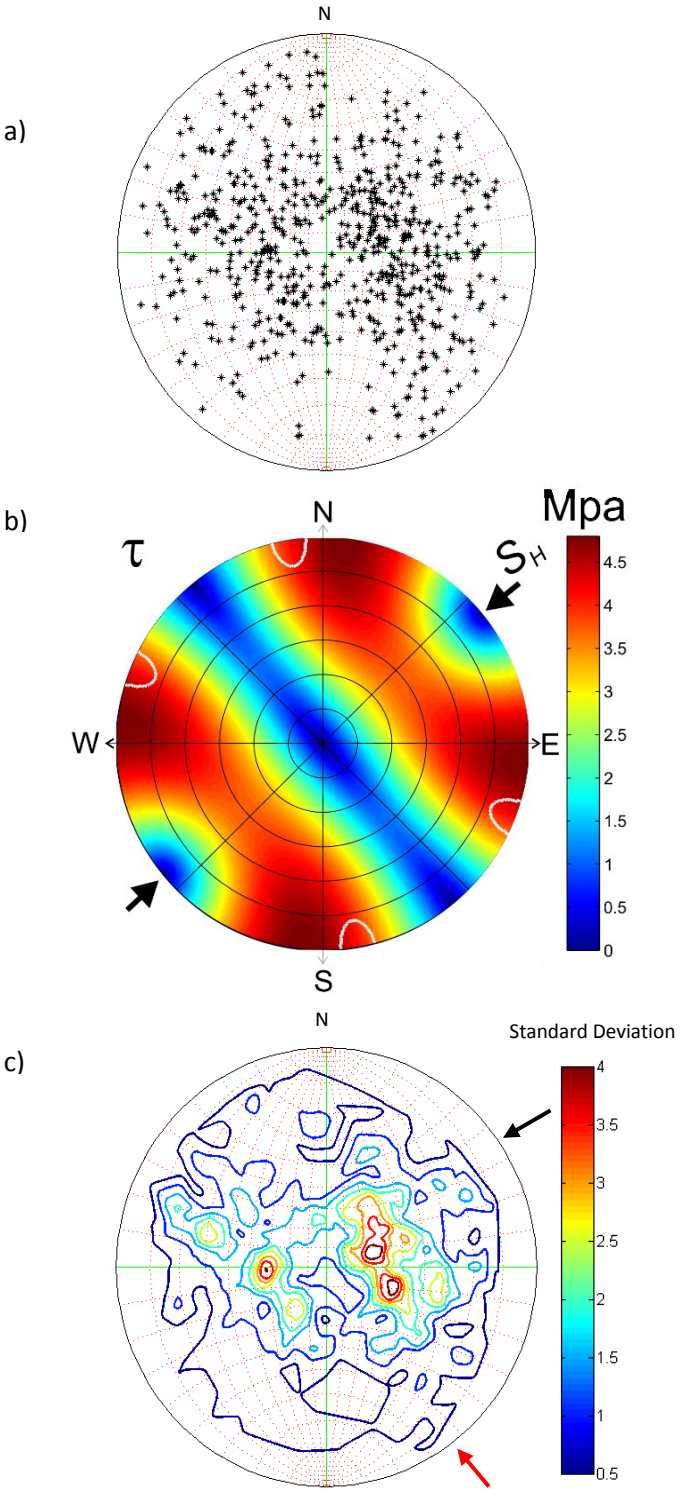

Figure 4.21: a) Stereonet projection of natural fracture planes poles b) Rotated stereonet projection of shear stresses acting on planes normal. Areas inside the white contour are where fracture slip could occur. The inputs used for this model were: $S_H = 15.0\ [MPa]$, $S_h = 5.0\ [MPa]$, $S_V = 7.53\ [MPa]$, $P_p = 1\ [MPa]$, $c = 0\ [MPa]$, $\mu = 0.6$. *Zero cohesion is assumed. c) Stereonet contour of fracture planes poles using Kamb method. Black and red arrows indicate orientation of* S_H *and* S_h *respectively. All plots are oriented to geographic North.*

4.8. Discussion

In this chapter fracture picking and interpretation from image logs were discussed. Natural fractures are distinguishable on image logs by their sinusoidal shape (Figure 4.1) but difficulties arise during picking and interpretation in a heavy oil reservoir due to the complexity of the lithology and shortcomings of the borehole tool. In this thesis, the best way to overcome these is to interpret fractures while consulting with the extracted core image data. To improve on this method of interpretation we suggest that the core should be inspected and logged in the core lab prior or during the interpretation of image logs as image log comparison and experience with actual core would be an improvement to that of core images.

Of the 22 well image logs that were interpreted, fracture depth, mean fracture azimuth, fracture dip and total well fracture count were collected. Natural fracture data logged are inherently angled fractures as horizontal fractures would be too difficult to reliably distinguish from bedding planes without extensive examination of the core. A total of 622 natural fractures were logged from the data. Figure 4.7 shows the frequency histogram of fractures with depth. Fractures appear throughout all depths of the wells; however, there is a higher abundance at approximately 300-400m depths located in the Grosmont C and D formations. We note that this is partially due to the aliasing of the logs as the Grosmont C and D are located at these depths and are the reservoir facies so therefore the log suites and image logs are targeted at these areas. As well, many of the logs were not deep enough to intercept the deepest Grosmont A. To further investigate the fracture depths we acquired topographic geospatial data from Natural Resources Canada (Figure 4.6b) and plotted fractures by elevation. Figure 4.7b shows natural fractures hung on the topographic elevation of the area. Although there is low relief in the area (40-50m height difference throughout study area) there is considerable grouping of the fractures at 200-250m elevation. This grouping corresponds to the Grosmont D member and the result is unsurprising as it is noted as a brecciated pervasively fractured unit and has vuggy with high porosity and high oil saturation.

Statistics of the fracture data were calculated including mean direction and preferred orientation testing. Rose diagrams of the fracture dip directions can be seen in Table 4. Although as a whole the orientations of the fractures in the study area appeared uniformly distributed, certain wells locally tested positive for preferred fracture directions. This implies that at these wells locally the stress regime (e.g., Queen & Rizer 1990; Barton et al, 1995) or zones of lithological weaknesses

are causing a preferential fracture orientation although some care needs to be taken with such interpretations as bridging of fractures by chemical precipitates during their formation may help to keep fractures open (e.g. Laubach et al. 2004). This is extremely important for directional well placement and fluid injection for bitumen extraction in the area from gravity drainage techniques. The main method of gravity drainage techniques is to heat the reservoir to lower the viscosity of the matrix bound bitumen such that it can be mobilized and drain so it can be produced. Therefore, our characterization of the fractures' dips and their orientation will lead to improved movement and production of the bitumen from the in-situ reservoir into the producer well. There may also be borehole biasing of the fracture data because one would expect vertical wells to naturally intersect more fractures with lower angle dips than higher angle dips as noted by Terzaghi (1965) and Priest (1985). Again, core logging may help remedy this as horizontal fractures can be difficult to interpret from image logs or separate from bedding planes. We suggest in future fracture characterization work introducing a weighting function to the statistical analysis and picking of fracture data to account for the fracture and well geometry.

To further investigate the fracture orientations, using a Schmidt net, the poles to the planes of the natural fractures (Figure 4.10) were contoured using a density contouring algorithm. A Kamb contouring algorithm was then applied to the density contour (Figure 4.11). If the natural fractures were oriented randomly then we would expect a standard deviation of points to lie inside the counting circle on the Schmidt net. Areas with 3 times higher (hot colours Figure 4.11) than the standard deviation are then assumed to be statistically significant. Therefore, with additional drilling of wells in the study area we expect to intersect more numerous North-South striking (East-West dip vectors and poles) fractures during further production. During bitumen recovery in this fracture system production depends on drainage rates, porosity and bitumen saturation systems, vertical matrix and fracture permeability and injection rates to name a few. For instance, to maximize product recovery of the injection and producing wells drilled, according to our analysis one might choose to place a horizontal well in an East-West orientation in order to intersect more natural fractures in the reservoir.

Drilling induced fractures were also observed in 20 of the wells. The interpretation DITF share many of the inherent difficulties of natural fractures, however, they are more distinct as they are vertical features located 180° from each other on the borehole. A total of 88 DITF were logged

from the fracture data (Table 2 and 3) as well as the corresponding fractures in each interval. The highest amount of DITF occur in the Grosmont C unit. This unit is pervasively vuggy (>0.5cm diameter) caused by leaching which perhaps contributed to weakening of tensile strength of the rock causing easier initiation of tensile failure. Table 4 shows the orientation of the DITF's in a rose diagram (Figure 4.13 contains all DITF's). They have a very strong orientation (circular deviation 9°) in the North-East and South-West direction indicating the direction of maximum horizontal stress,S_H, directed at 50°NE as well that the minimum horizontal stress direction, S_h, oriented at 140°SE. The maximum horizontal stress direction in conjunction with the Kamb contour plot have interesting implications as the natural fracture poles contouring (Figure 4.11) dipping East and West (fracture strikes North-South) align in between the principal horizontal stresses. However there remains some significant deviation of the contours in the direction of S_H (fracture strike in the direction of S_h). This type of geometry may suggest a strike slip or reverse faulting environment (see Figure 2.9).

The DITF were quality ranked using the World Stress Map. However it should be noted that the quality rankings are made for much deeper wells. Although the wells in this study area at face value rate poorly according to this scheme, we argue that the confidence of our interpretations remain solid the DITF are extremely distinct, the orientations have very low variance and standard deviation and with the proximity of wells we believe the World Stress Map (Tingay et al. 2008) quality rankings in this case do not properly reflect the quality of the data set itself which provides we believe very resilient stress direction indication. As this doesn't add significantly to the discussion we have included this in the appendix.

The horizontal stresses in the area were bound using 3 different scenarios based on empirical laboratory measurements on differing carbonates. Solving the borehole centric stress equations (equations *(4.14)-(4.15)*) and using the empirical rock properties given from by the characterization of each rock's Mohr-Coloumb envelope, we could better model the stress conditions in the S_H-S_h space where the borehole could experience tensile or shear failure. Because DITF's occurred in the boreholes the combination of horizontal stresses must lie above (in negative tangential stress) the tensile fracture limit. Similarly since no borehole breakouts found in the image logs the combination of horizontal stresses were bound below the shear fracture limit for each case study rock; this created the conditions for bounding the horizontal stresses. The vertical

stress was calculated using density logs included in the study data. The stress bounds of $11.6MPa < S_H < 15.0\,MPa$ for maximum horizontal stress and $5.4\,MPa < S_h < 6.6\,MPa$ for minimum horizontal stress, with average vertical stress, S_v, of 7.53 and 8.31 MPa for Grosmont formations C and D respectively (Table 6). This combination suggests that the study area is in a strike slip faulting environment ($S_h < S_V < S_H$). Our analysis compares well with the in-situ empirical measurements recorded by Bell (1994) (Figure 2.11) for S_h where in shallow depths (300-420m) his data ranged 5.6-7.9 MPa.

Lastly we applied a simple stability analysis by calculating all normal and shear stresses acting at all orientations of fracture planes. This requires knowledge of the in-situ state of stress, pore pressure of the formation and criterion for slip such as the coefficient of friction and cohesion. Using lab testing done by Scuderi (2013) of dolomite coefficient of friction as a function of normal stress we contoured areas of instability. It should be noted here that without lab measurements of in-situ bitumen saturated Grosmont core at best this model yields an estimate of probable directional instability. The contoured results showed remarkable stability even with zero cohesion assumed. The azimuthal direction of the planes that show instability remain more or less unchanged with varying coefficients of friction and cohesion (~45-70° from S_H). We can see the preferred orientations of the fractures are in the stable zone as only extremely steeply dipping (>70°) fractures within the strikes of 45-70° of S_H appear unstable; this could be due to the aliasing of high angle fractures due to their difficulty in interpretation in FMI data and lower probability of intersection with a vertical well. The apparent stability of the area could also be due to the underpressured nature of the reservoir. The only direct measurement of pore pressure is located just outside the study area and it being only 1 MPa suggests high stability.

4.9. Concluding Remarks

A total of 622 natural fractures and 88 DITF were logged. The Grosmont D was the most fractured unit in the study and from Kamb's contouring method we found that most often fracture planes preferred strikes that were oriented North-South. From the DITF data the directions of S_H and S_h were found to be 50°NE and 140°SE respectively. Interestingly the preferred orientation of the fracture strikes is between the two principal stresses. The horizontal stresses were bound at $11.6\,MPa < S_H < 15.0\,MPa$ and $5.4\,MPa < S_h < 6.6\,MPa$. The vertical stress was calculated from density log data and was 7.53 and 8.31 MPa for Grosmont formations C and D

respectively. A stability model was run and the results show that it is stable through a combination of low pore fluid pressure, frictional coefficients, and stress magnitudes. The implication of this are that one is not probably going to expect slip on these fractures, meaning no induced seismicity but probably more practically one might not expect slow slip that might damage casings in situ.

5. Conclusion

5.1. Computed Tomography

The main objective of this thesis was to characterize the fracture network and stress regime of the Grosmont study area. We attempted an orientation technique for downhole image log data and extracted core CT data. The technique would have allowed for orientation of high resolution CT image data to be used for reservoir modelling and fracture characterization. We unwrapped the CT slices and forming a whole core scan that could be oriented with the FMI image logs but due to the lack of vertical resolution the results did not yield meaningful results.

5.2. Natural Fractures

Fractures from 22 wells were logged from image logs. There are inherent difficulties in interpreting fractures from FMI logs in a complex heavy oil reservoir. The interpretation was therefore done with the aid of core imagery and apparent fractures that were present in extremely vuggy sections and in areas where the corresponding core image data was of extremely poor quality were ignored. The natural fracture dips and orientations appear random throughout the wells with few wells testing positive for a preferred orientation of fracture direction aligning between the maximum horizontal stresses. Statistical testing and contouring was then done using the natural fracture data and it was determined that the preferred orientation of fracture strikes are mainly North-South with some deviation of the poles towards S_H.

5.3. Drilling Induced Tensile Fractures, Stress Bounds and Stability Analysis

DITF were logged in 20 of the wells in the study area and the maximum and minimum stress directions were determined to be 50°NE and 140°SE respectively. The greatest concentration of DITF occurred in the Grosmont C interval. This interval has abundant vugs compared to the stacked karsted-breccia, laminated dolomite, and brecciated dolomite of the Grosmont D interval. This vugginess perhaps contributed to weakening of tensile strength of the rock initiating tensile failure. With the lack of borehole breakouts in the data we applied the equations of stress located at the borehole wall (equations *(4.14)-(4.15)*) and used empirical tri-axial stress measurements from 3 comparative carbonates (Indiana Limestone, Carrara Marble carbonates and Toral de Los Vados limestone) in order to set up allowable stress values for the study area. We found the gross estimates of maximum stress to be $11.6\ MPa < S_H < 15.0\ MPa$, as well as minimum stress to

be 5.4 $MPa < S_h < 6.6\ MPa$. The calculated average vertical stress of 7.53 and 8.31 MPa for Grosmont formations C and D respectively suggests that the Grosmont reservoir is in a strike-slip faulting environment ($S_h < S_V < S_H$). The stability analysis resulted in indicating the area is extremely stable. We can conclude that the orientation of most likely slip of fracture planes will occur 45-70° from the orientation of S_H at high dips (>70°).

5.4. Future Recommendations

For future work in fracture characterization we suggest improving on the CT core orientation method by taking higher vertical resolution CT slice data along the same order as the horizontal resolution. This would allow for accurate unwrapping of the core surface to match with downhole FMI image log data for orientation as well as high resolution 3D modelling of fractures in core.

We also recommend implementing a weighting function for fracture logging and interpretation due to the vertical well's bias of intersection a greater number of low-dipping natural fractures rather than vertical natural fractures.

Further, we recommend improving on the gross stress constraints by gathering laboratory tri-axial strength data from bitumen saturated and unsaturated Grosmont core from the individual intervals. The rock cohesion and friction angle values measured from the Grosmont intervals would yield a more accurate representation of the local stress regime. Additionally, these parameters would be of great use to the fault stability analysis. The stability analysis, too, should seek to include more knowledge on the operational parameters of the steam injection as this is expected to raise the pore pressures in the reservoir. This may cause a larger range of fractures to potentially become unstable.

There is also one final issue, not yet discussed, that is worthy of mention. The existence of the drilling induced tensile fractures points towards rather high in situ horizontal compression relatively close to the surface. High horizontal compressions are rarely discussed but in Canada have been evidenced by various 'pop-up' and low-dipping thrust fault features in freshly exposed quarry surfaces in Manitoba (Everitt 2009) and Ontario (Adam & Fenton 1994). The origins of such stresses are not completely understood; and they can also provide directions for additional study.

References

Aadnoy, B.S. & Bell, J.S., 1998. Classification of Drilling-Induced Fractures and Their Relationship to In-Situ Stress Directions. *The Log Analyst*, (November-December), pp.27–42.

Aadnoy, B.S. & Chenevert, M.E., 1987. Stability of Highly Inclined Boreholes (includes associated papers 18596 and 18736). *SPE Drilling Engineering*, 2(4), pp. 364-374.

Adam & Fenton, 1994. Stress relief and incidental geological observations in and around Ottawa, Ontario. *Current research*, pp.155–160.

Alberta Energy Regulator, 2016. *Root Cause and Regulatory Response Report*, Available at: https://www.aer.ca/documents/reports/IR_20160321-CNRL.pdf.

Anderson, E.M., 1905. Facsimile reproduction of The Dynamics of Faulting, The Geological Society of London, Special Publications 2012, vol 367, pp.231-246.

Anderson, E.M., 1951. *The Dynamicas of Faulting and Dyke Formatin with Applications to Britain*, Hardner Pub. Co.

Ardakani, E.P. & Schmitt, D.R., 2015. Investigation of Devonian Unconformity Surface Using Legacy Seismic Profiles , NE Alberta.

Babcock, A., 1974. Jointing in Central Alberta. Canadian Journal of Earth Sciences. 11(8) pp.1181–1186.

Babcock, A., 1973. Regional Jointing in Southern Alberta. Canadian Journal of Earth Sciences. 10(12), pp. 1769-1781

Babcock, E. a. & Sheldon, L.G., 1976. Structural significance of lineaments visible on aerial photos of the athabasca oil sands area near Fort Mackay, Alberta. Bulletin of Canadian Petroleum Geology, 24(3), pp.457–470.

Babcock, E.A., 1978. Measurement of Subsurface Fractures from Dipmeter Logs. AAPG Bulletin 62(7) pp. 1111-1126.

Baranova, Mustageem & Bell, 1999. A model for induced seismicity caused by hydrocarbon production in the Western Canada Sedimentary Basin. *Canadian Journal of Earth Sciences*, (36), pp.47–64.

Barrett, K.R., & Hopkins, J.C., 2010. Review of geology of a giant carbonate bitumen reservoir, Grosmont Formation, Saleski, Alberta. *Heavy oils : reservoir characterization and production monitoring*. Chopra, S., Lines, L., Schmitt, D.R., and Batzle, M. (eds.). Society of Economic Geophysicists, Geophysical Developments, (13), pp. 155-163.

Barton, Colleen A., Zoback, M.D., & Moos, D., 1995. Fluid flow along potentially active faults in crystalline rock. Geology, 23(8), pp.683–686.

Bell, D.C. & Woodland, J.S., 1989. IN SITU STRESS MAGNITUDES FROM MINI-FRAC RECORDS IN WESTERN CANADA In situ stress magnitudes from mini-frac records in western Canada. Journal of Canadian Petroleum Technology, 28(05).

Bell, J.S., Price, P.R., & McLellan, P.J., 1994. In Situ Stress in the Western Canada Sedimentary Basin. *Geological Atlas of the Western Canada Sedimentary Basin*, pp. 439–446.

Bell, J.S., Grasby, S.E., 2012. The stress regime of the Western Canadian Sedimentary Basin. Geofluids, 12(2), pp.150–165.

Bell, J.S. & Babcock, E. A., 1986. The stress regime of the Western Canadian Basin and implications for hydrocarbon production. *Bulletin of Canadian Petroleum Geology*, 34(3), pp.364–378.

Bell, J.S. & Bachu, S., 2003. In situ stress magnitude and orientation estimates for Cretaceous coal-bearing strata beneath the plains area of central and southern Alberta. Bulletin of Canadian Petroleum Geology, 51(1), pp.1–28.

Bell, J.S. & Gough, D.I., 1979. Northeast-southwest compressive stress in Alberta evidence from oil wells. *Earth and Planetary Science Letters*, 45(2), pp.475–482.

Belyea, 1956. Devonian sediments of Bow Valley and adjacent areas. *AAPG Database*, pp.66–91.

Belyea, 1952. Notes on the Devonian system of the north-central plains of Alberta. *Geological Survey of Canada*.

Broughton, L., P., 2013. Devonian salt dissolution-collapse breccias fl ooring the Cretaceous Athabasca oil sands deposit and development of lower McMurray Formation sinkholes ,. *Sedimentary Geology*, 283, pp.57–82. Available at: http://dx.doi.org/10.1016/j.sedgeo.2012.11.004.

Brudy, M. & Kjørholt, H., 2001. Stress orientation on the Norwegian continental shelf derived from borehole failures observed in high-resolution borehole imaging logs. *Tectonophysics*, 337(1-2), pp.65–84.

Brudy, M. & Zoback, M.., 1999. Drilling-induced tensile wall-fractures: implications for determination of in-situ stress orientation and magnitude. *International Journal of Rock Mechanics and Mining Sciences*, 36(2), pp.191–215.

Buschkuehle, B.E., Hein, F.J. & Grobe, M., 2007. An overview of the geology of the upper devonian grosmont carbonate bitumen deposit, Northern Alberta, Canada. *Natural Resources Research*, 16(1), pp.3–15.

Byerlee, J., 1978. Friction of Rocks. *Pure and applied geophysics*, 116(4), pp. 615-626.

Campbell, 1979. MAJOR CLEAT TRENDS IN ALBERTA PLAINS COALS. *CIM Bulletin [0317-0926]*, 72(802), pp.69–75.

Cox, J.W., 1970. The high resolution dipmeter reveals dip-related borehole and formation characteristics SPWLA 11th Annual Logging Symposium. Society of Petrophysicists and Well-Log Analysts

Cutler, W.G., 1982. *Stratigraphy and sedimentology of the Upper Devonian Grosmont Formation, Alberta, Canada*. Geology and Geophysics, University of Calgary. Available at: http://hdl.handle.net/1880/22422.

Dusseault, M.E., 1977. Stress state and hydraulic fracturing in Athabasca oil sands. Journal of Canadian Petroleum Technology, 16(03).

Ekstrom, M.P., Dahan, C.A., Chen, M.Y. Lloyd, P.M., & Rossi, D.J., 1987. Formation Imaging With Scanning Arrays. SPWLA 27th Annual Logging Symposium Society of Petrophysicists and Well-Log Analysts.

ERCB, 2013. *Alberta's Energy Reserves 2012 and Supply/Demand Outlook 2013–2022*, Available at: www.ercb.ca.

ERCB-Staff, 2010. *Surface Steam Release of May 18, 2006 Joslyn Creek SAGD Thermal Operation*, Available at: https://www.aer.ca/documents/reports/ERCB_StaffReport_JoslynSteamRelease_2010-02.pdf.

Everitt, R.A., 2009. Pop-ups and related damage in granite at the Medika Pluton in southeastern Manitoba. *NRC Research Press*, pp.1001–1008.

Ezeuko, C.C., Wang, K., Kallos, M.S., & Gates, I. D., 2015. Towards the Development of Bitumen Carbonates : An Integrated Analysis of Grosmont Steam Pilots. Oil & Gas Science and Technology - Revue d'IFP Energies nouvelles , 70(6), pp. 983-1005.

Fordjor, C.K., Bell, J.S. & Gough, D.I., 1983. Breakouts in Alberta and stress in the North American plate. Canadian Journal of Earth Sciences, 20(9), pp. 1445-1455.

Gendzwll, D.J., & Stauffer, R.M., 1986. Fractures in the northern plains, stream patterns, and the midcontinent stress field. Canadian Journal of Earth Sciences, 24(6), pp. 1086-1097.

Genter, A., Castaing, C. Dezayes, C., Tenzer, H., Traineau, H., & Vilemin, T., 1997. Comparative analysis of direct (core) and indirect (borehole imaging tools) collection of fracture data in the Hot Dry Rock Soultz reservoir (France). *Journal of Geophysical Research*, 102(B7), p.15-419.

Gough, D.I. & Bell, 1982. Stress orientations from borehole wall fractures with examples from Colorado , east Texas , and northern Canada. *Canadian Journal of Earth Sciences*, 19(7), pp. 1358-1370.

Gough, D.I. & Bell, J.S., 1980. Stress orientations from oil-well fractures in Alberta and Texas. Canadian Journal of Earth Sciences, 18(3), pp. 638-645.

Gronseth, P.R. & Kry, J.M., 1983. IN-SITU STRESSES AND HYDRAULIC FRACTURING IN THE DEEP BASIN. Journal of Canadian Petroleum Technology, 22(6).

Hamid, O.H., 2008. *In-Situ Stress Analysis of Southwest Saskatchewan*. Doctoral dissertation.

Hassan, D., 1982. A method for predicting hydraulic fracture azimuth and the implications thereof to improve hydrocarbon recovery. Annual Technical Meeting, Petroleum Society of Canada.

Hawkes, C.D., Bachu, S., Haug, K., & Thompson, A.W., 2005. Analysis of In-Situ Stress Regime in the Alberta Basin , Canada , for Performance Assessment of CO2 Geological Sequestration Sites. Proceedings of the 4th annual conference on carbon capture and sequestration DOE/NETL

Henriksen, 2001. *Fracture Interpretation Based on Electrical and Acoustic Borehole Image Logs*. BRGM Rep. BRGM/RP-50, 835-FR

Holzhausen, G.R., Wood, M.D., Raisbeck, J.M., & Card, C.C., 1980. Results of deformation monitoring during steam simulation during a single-well test. Proceedings of Applied OIlsands Geoscience: 11-13.

Horner & Barclay, 1994. Earthquakes and hydrocarbon production in the Fort St. John area of northeastern British Columbia. *Canadian Journal of Exploration Geophysics*, 30, pp.39–50.

Hunt, P.K., Engler, P., & Bajsarowics, C., 1988. Computed -Tomography as a Core Analysis Tool : Applications , Instrument Evaluation , and Image Improvement Techniques. Journal of Petroleum Technology, 40(9), pp.1-203.

Jaeger, J.C., & Cook, N. G., 1976. Fundamentals of Rock Mechanics. Third Edition, Chapman and Hall, London, p. 593.

Kaiser, P.K., Mackay, C., & Morgenstern, N., 1982. PERFORMANCE OF A SHAff IN WEAK ROCK (BEARPA W SHALE) Tragverhalten eines Schachtes in weichem Gebirge Performance d'un puits dans un rocher doux. Rock mechanics: caverns and pressure shafts 2: pp.613–622.

Kamb, W.B., 1959. Ice petrofabric observations from blue glacier, Washington, in relation to theory and experiment. *Journal of Geophysical Research*, 64(11), pp. 1891-1909.

Katsevich, A., Frenkel, M., Feser, M., Huang, Z., Andrew, M., Case, A., Gu, A., & Thompson, W., 2015. New Fast and Accurate 3D Micro Computed Tomography Technology for digitial core analysis. SPE Annual Technical Conference and Exhibition. Society of Petroleum Engineers.

Kirsch, E.G., 1898. Die Theorie der Elastizität und die Bedürfnisse der Festigkeitslehre. *Zeitschrift des Vereines deutscher Ingenieure*, 42, pp.797–807.

Lau, J.S.O. & Auger, L.F., & Bison, J.G., 1987. Subsurface fracture surveys using a borehole television camera and acoustic televiewer. Canadian Geotechnical Journal 24(4), pp. 499-508.

Laubach, S.E., Olson, J.E. & Gale, J.F.W., 2004. Are open fractures necessarily aligned with maximum horizontal stress ?, Earth and Planetary Science Letters, 222(1), pp.191–195.

Law, 1955. Geology of northwestern Alberta and Adjacent areas. *AAPG Bulletin*, 39(10), pp. 1927-1975.

Leshchyshyn & Seyer, 1990. Three field techniques to estimate the effective permeability and fracture properties of Athabasca Oil Sands. Annual Technical Meeting. Petroleum Society of Canada

Luthi, 2001. *Geological Well Logs: Their Use in Reservoir Modeling*, Springer Science & Business Media.

Luthi & Souhaite, 1990. Fracture apertures from electrical borehole scans. *Geophysics*, 55(7), pp.821–833.

Machel, H.G., Borrero, M. L., Dembicki, E., Huebscher, H., Ping, L., Zhao, T., 2012. The Grosmont : a complex dolomitized, fractured and karstified heavy oil reservoir in a Devonian carbonate-evaporite platform. *GeoConvention 2012: Vision*, pp.1–24.

Machel, H.G., Borrero, M. L., Dembicki, E., Huebscher, H., H., Ping, L., Zhao, T., 2012. The Grosmont: the world's largest unconventional oil reservoir hosted in carbonate rocks. *Geological Society, London, Special Publications*, 370, pp.49–81.

Macneil, J., A., 2015. Petrophysical Characterization of Bitumen-Saturated Karsted Carbonates : Case Study of the Multibillion Barrel Upper Devonian Grosmont Formation ,. *Petrophysics*, 56(6), pp.592–614.

Major, R.P. & Holtz, M.H., 1997. Identifying fracture orientation in a mature carbonate platform reservoir. *American Association of Petroleum Geologists Bulletin* **81**, 1063-1069.

Mardia, K.V., 1972. *Probability and Mathematical Statistics*, Academic Press London and New York.

McGarr, A., and N. C. Gay, 1978. State of stress in the earth's crust, Annu. Rev. Earth Planetary Science., 6, 405-436.

McLellan, P.J., 1988a. In-situ stress prediction and measurement by hydraulic fracturing. *Journal of Canadian Petroleum technology*, 27(2), pp.85–95.

McLellan, P.J., 1988b. In-Situ stress magnitudes from hydraulic fracture treatment records- a feasibility study. *Geological Survey of Canada*, Open File Report 1947, p.30.

Mcleod, J.G.F., 1979. SUCCESSFUL INJECTION PATTERN ALTERATION, PEMPINA J LEASE, ALBERTA. *Journal of Canadian Petroleum Technology*, 17(1), pp.51–55.

Middleton, G. V., 2000. Data Analysis in the Earth Sciences Using Matlab. Prentice Hall

Misra, K.S., 1991. Mapping of Basement and other Tectonic Features Using Seasat and Thematic Mapper in Hydrocarbon-Producing Areas of the Western Sedimentary Basin of Canada. *Canadian Journal of Remote Sensing*, 17(2), pp.137–151. Available at: http://dx.doi.org/10.1080/07038992.1991.10855287.

Moeck, I., Kwiatek, G. & Zimmerman, G., 2009. Slip tendency analysis, fault reactivation potential and induced seismicity in a deep geothermal reservoir. *Journal of Structural geology*, (31), pp.1174–1182.

Mohebati, H. M., Yang, D., & MacDonald, J. 2014. Thermal Recovery of Bitumen From the Grosmont Carbonate Formation - Part 1: The Saleski Pilot. Society of Petroleum Engineers. vol. 53(4)

Morris, Ferrill & Henderson, 1996. Slip-tendency analysis and fault reactivation. *Geology*, (24), pp.275–278.

Nelson, R.A., Lenox, L.C., Ward, B.J. 1987. Oriented Core: Its Use, Error, and Uncertainty. *The American Association of Petroleum Geologists Bulletin* 71: 357-367

Pana, D., Waters, J. & Grobe, M. 2001. GIS compilation of structural elements in Northern Alberta Release 1.0. pp. 53. Alberta Geological Survey/Alberta Energy and Utilities Board.

Paulsen, T.S., Jarrard, R.D. & Wilson, T.J., 2002. A simple method for orienting drill core by correlating features in whole-core scans and oriented borehole-wall imagery. , 24, pp.1233–1238.

Perras, M.A. & Diederich, M.S. 2014. A Review of the Tensile Strength of Rock: Concepts and Testing. *Geotech Geol Eng* **32**, 525-546.

Pezard, P. A., and S. M. Luthi 1988. Borehole electrical images in the basement of the Cajon Pass Scientific Drillhole, California - fracture identification and tectonic implications, Geophys Res Lett, 15(9), 1017-1020, doi:10.1029/Gl015i009p01017

Plumb, R.A. & Hickman S., 1985. Stress-induced borehole elongation: A comparison between the four-arm dipmeter and the borehole televiwer in the Auburn geothermal Well. *Journal of Geophysical Research*, (1).

Ponziani & Luthi, 2015. Experimental vlidation of fracture aperture determination from borehole electric microresistivity measurements. *Geophysics*, 80(D175-D181), pp.175–181.

Priest, S.D., 1985. Discontinuity Analysis for Rock Engineering. George Allen & Unwin, London, pp. 124

Proskin, S.A., Scott, J.D. and Chhina, H.S. 1990a. Current practice in the interpreation of microfrac tests. Presented at the SPE California Regional Meeting, Ventura, California, USA

Proskin, S.A., Scott, J.D. and Chhina, H.S. 1990b. Interpretation of the minimum stress from micro-frac tests. *Rock at Great Depth*, 3, pp.1509–1519.

Queen, J.H. & Rizer, W.D., 1990. An Integrated Study of Seismic Anisotropy and the Natural Fracture System at the Conoco Borehole Test Facility , Kay County , Oklahoma. , Journal of Geophysical Research, vol 95(B7), pp. 11255-11273.

Rajabi,M.R., Sherkati, S., Bohloli, B., Tingay, M., 2010. Subsurface fracture analysis and determination of in-situ stress direction using FMI logs: An example from the Santonian carbonates (Ilam Formation) in the Abadan Plain, Iran, Tectonophysics, vol 492, pp. 192-200

Rees, E.V.L., Priest, J. a. & Clayton, C.R.I., 2011. The structure of methane gas hydrate bearing sediments from the Krishna-Godavari Basin as seen from Micro-CT scanning. *Marine and Petroleum Geology*, 28(7), pp.1283–1293. Available at: http://dx.doi.org/10.1016/j.marpetgeo.2011.03.015.

Reiter, K., Heidbach, O., Schmitt, D. Haug, K. Ziegler, M., & Moeck, I., 2014. A revised crustal stress orientation database for Canada. *Tectonophysics*, 636, pp.111–124. Available at: http://dx.doi.org/10.1016/j.tecto.2014.08.006.

Russel-houston, J. & Gray, K., 2014. Karst Paleokarst in the Grosmont Formation and reservoir implications. Saleski, Alberta, Canada, Interpretation 2(3), pp.29–50.

Sausse, J. & Genter, A., 2005. Types of permeable fractures in granite. Geological Society, London, Special Publications 240.1, pp.1–14.

Scheidegger, E., A., 1983. Interpretation of fracture and physiographic patterns in Alberta, Canada. Journal of Strucural Geology , 5(1), pp. 53-59.

Schmitt, D.R., 2014. Basic Geomechanics for Induced Seismicity : A Tutorial. CSEG Recorder, 39(9), pp.24–29.

Schmitt, D.R., Currie, C. a. & Zhang, L., 2012. Crustal stress determination from boreholes and rock cores: Fundamental principles. *Tectonophysics*, 580, pp.1–26. Available at: http://dx.doi.org/10.1016/j.tecto.2012.08.029.

Schmitt, D.R. & Haimson, B., 2016. Hydraulic Fracturing Stress MEasurements for inclusion in *Rock Mechanics and Engineering*. ms, pp. 52, in press

SCHMITT, D.R. & ZOBACK, M.D., 1989. Poroelastic Effects in the Determination of the Maximum Horizontal Principal Stress in Hydraulic Fracturing Tests A Proposed Breakdown Equation Employing a Modified Effective Stress Relation for Tensile Failure. *International Journal of Rock Mechanics and Mining Sciences & Geomechanics Abstracts* **26**, 499-506.

Scuderi, M.M., Niemeijer, A. R., Collettini, C., & Marone, C., 2013. Frictional properties and slip stability of active faults within carbonate – evaporite sequences : The role of dolomite and anhydrite. *Earth and Planetary Science Letters*, 369-370, pp.220–232. Available at: http://dx.doi.org/10.1016/j.epsl.2013.03.024.

Seeburger, D. a & Zoback, M.D., 1982. The Distribution of Natural Fractures and Joints at Depth in Crystalline Rock. *Journal of Geophysical Research*, 87(B7), pp.5517–5534.

Settari, Antonin, and J. M. Raisbeck, 1979. Fracture mechanics analysis in in-situ oil sands recovery. *Journal of Canadian Petroleum Technology* 18.02: 85-94.

S Smith, R.J., 2010. 15 years of passive seismic monitoring at Cold Lake, Alberta. *CSEG Recorder*. vol 35(7) Available at: http://csegrecorder.com/assets/pdfs/2010/2010-09-RECORDER-15_years_of_passive_seismic_monitoring.pdf.

Talebi, 1991. Microseismic mapping of a hydraulic fracture. *Rock Mechanics as a Multidisciplinary Science*, pp.461–470.

Teichrob, R., Kustamsi, A., Hareland, G., & Odiegwu, U., 2010. Estimating In Situ Stress Magnitudes And Orientations In an Albertan Field In Western Canada. 44th US Rock Mechanics Symposium and 5th US-Canada Rock Mechanics Symposium, American Rock Mechanics Association

Terzaghi, R., 1965. Sources of error in joints surveys. Geotechnique. vol 15, pp. 287-304

Tingay, M.R.P., Reinecker, J. & Müller, B., 2008. Borehole breakout and drilling-induced fracture analysis from image logs. World Stress Map Project pp.1-8.

Urban, E. & Aguilera, R., 2015. Determination of Principal In-Situ Stress Magnitude from Well Logs in Unconventional Reservoirs : A Practical Application in Willesden Green Field , Canada. SPE Latin American and CAribbean Petroleum Engineering Conference. Society of Petroleum Engineers.

Wagner, P.D., Nelson, R., Lonnee, J., Costello, M., Whale, R., McKinzie, W., Jennings, J., Balzarini, M., Reed, D., A.S., A.B. & Watson, R.C. 2010. Fracture Characterization of a Giant Unconventional Carbonate Reservoir, Alberta, Canada. In: *AAPG Int. Conf. and Exhibition*, pp. 2. American Association of Petroleum Geologists.

Walton, G., Arzua, J., Alejano, L.R., & Diederichs, M.S., 2014. A Laboratory-Testing-Based Study on the Strength, Deformability, and Dilatancy of Carbonate Rocks at Low Confinement. *Rock Mechanics and Rock Engineering*.48(3) pp. 941-958.

Weides, Moeck & Schmitt, 2014. An integrative geothermal resource assessment study for the siliclastice Granite Wash Unit, northwestern Alberta (Canada). *Environmental Earth Sciences*, 72(10), pp.4141-4154.

Whitaker, A.E. & Engelder, T., 2005. Characterizing stress fields in the upper crust using joint orientation distributions. Journal of Structural Geology, vol 27, pp.1778–1787.

Wyman, R. E., Holditch, S. A., & Randolph, P. L. 1980. Analyses of an Elmworth Hydraulic Fracture in Alberta. Journal of Petroleum Technology 32(9), pp. 1-621.

Yang, D. Hosseininejad Mohebati, M., Brand, S., & Bennet, C., 2014. Thermal Recovery of Bitumen From the Grosmont Carbonate Formation — Part 2 : Pilot Interpretation and Development Strategy. Journal of Canadian Petroleum Technology 43(4) pp. 212-223.

Zoback, M. Lou, M., et al., 1989. Global patterns of tectonic stress. *Nature*, 341(6240), pp.291–298.

Zoback, M.D. & Schmitt, D.R., 1993. Infiltration Effects in the Tensile Rupture of Thin Walled Cylinders of Glass and Granite : Implications for the Hydraulic Fracturing Breakdown Equation. International Journal of Rock Mechanics and Mining Sciences & Geomechanics Abstracts, vol 30(3),pp. 289-303

Appendix

Well ID	WSM Quality
1-10-85-19W4	D
2-26-85-19W4	D
4-16-85-19W4	C
7-20-085-19W4	D
8-27-85-19W4	D
9-18-85-19W4	C
10-12-85-20W4	C
10-15-85-19W4	D
10-25-85-19W4	D
11-15-85-19W4	D
11-32-84-19W4	D
13-14-85-19W4	C
15-24-85-19W4	C
16-6-85-19W4	D
100-2-27-85-19W4	D
100-6-22-85-19W4	D
100-8-22-85-19W4	D
100-10-27-85-19W4	D
102-7-26-85-19W4	D
102-10-26-85-19W4	D

Table 8: Quality ranking index for DITF from World Stress Map Project (WSM).

WSM guidelines: A-Quality) > 10 distinct DITF zones and combined length > 100m with standard deviation < 12°; B-Quality)>6 distinct DITF zones and combined length >40m with a standard deviation < 20°; C-Quality) >4 distinct DITF zones or <20m combined length with standard deviation <40°; E-Quality) wells without reliable DITF or with standard deviation > 40°.

- Script that was used to pick natural fractures and DITF. Script concatenates image files into Matlab workspace and using graphical mouse input scales azimuthal and depth to pixels in the image. Fractures are then picked and saved.

```
% A = imread('Filename');
%%
close all;

load_data_flag =1;

%% Load data
if load_data_flag ==1;
%
%  las_file = load('Curves.txt');
%  log_depth = las_file(:,1);
%  caliper3 = las_file(:,3:5); % 1) depth, 3-4-5) calipers
%  caliper_ave = mean(caliper3(:,3:end),2);
%%
tifffiles = dir('*.tif');
nfiles = length(tifffiles);

    for n= 1:nfiles;


        data{n} = imread(tifffiles(n).name);


    end % endfor

    % concatenate all log data into one matrix

%     DATA = data;
    DATA = data{1,1};

    for i = 2:length(data(1,:))

        DATA=vertcat(DATA,data{1,i});

    end

%%  Subsection of data

clf

imagesc(data{1,3});

reply = input ('Input depth axis, subsection and 0-360 coordinates?
[Y]/[N]:', 's');
        if reply == ('Y')||('y')
    %% 1) DEPTH AXIS - INPUT
[ null, depths] = ginput(2); % log input for depth axis
% top = depths(1,1);
% bot = depths(2,1);
```

```
% imagesc(data{1,3});
%% 2) SUBSECTION - INPUT
[L, r] = ginput(2); % input for subsection of data

left = ceil(L(1,1));
right = ceil(L(2,1));

subsection_data = DATA;
subsection_data = subsection_data(:,left:right,:); % need last colon cause
its image with RGB


clf
imagesc(subsection_data);
%% 3) 0-360 AZIMUTH - INPUT
[beg, en] = ginput(2); %coordinates for 0-360 the axis of FMI

zero = ceil(beg(1,1));
three60 = ceil(beg(2,1));

        end
end % endif
%%
% appended = vertcat(A,B) ==> appended = [A | B]'


imagesc(subsection_data);

counterrow=0;
% countery=0;

for i =1:200

    reply = input ('Insert Another Stress Feature? [Y]/[N]:', 's');
        if reply == ('Y')||('y')

            counterrow = counterrow+1;
%         countery = countery+1;
            [x, y] = ginput(2);
%  make the coordinates
            DC(counterrow,:) = [y(1) y(2)]; % depth coordinates y1->y2
            DIR(counterrow,:) = [x(1) x(2)];

        elseif reply == ('N') || ('n')

          break
        end % endif

end
```

- Function that takes fracture azimuths and dip directions (or poles). And plots them on lower hemisphere stereonet. Function calls Data_density_small (listed below) to preform density contouring. Expanded on codes written by Gerard Middleton (2000).

```
function Schmidt_contour( azimuth,dip )

%% start poles
for i= 1:length(dip)
if dip(i) < 90
    dip(i) = dip(i);
elseif dip(i) > 90
    dip(i) = 180-dip(i);
%     azimuth(i)=azimuth(i)+180;
end
azimuth = wrapTo360(azimuth+180);
%% end poles
 end
N = 50;
cx = cos(0:pi/N:2*pi);                          % points on circle
cy = sin(0:pi/N:2*pi);
xh = [-1 1];                                    % horizontal axis
yh = [0 0];
xv = [0 0];                                     % vertical axis
yv = [-1 1];
axis([-1 1 -1 1]);
axis('square');
plot(xh,yh,'-g',xv,yv,'-g');                    %plot green axes
axis off;
hold on;
plot(cx,cy,'-w');                               %plot white circle
psi = [0:pi/N:pi];
for i = 1:8                                     %plot great circles
   rdip = i*(pi/18);                            %at 10 deg intervals
   radip = atan(tan(rdip)*sin(psi));
   rproj = tan((pi/2 - radip)/2);
   x1 = rproj .* sin(psi);
   x2 = rproj .* (-sin(psi));
   y = rproj .* cos(psi);
   plot(x1,y,':r',x2,y,':r');
end
for i = 1:8                                    %plot small circles
   alpha = i*(pi/18);
   xlim = sin(alpha);
   ylim = cos(alpha);
   x = [-xlim:0.01:xlim];
   d = 1/cos(alpha);
   rd = d*sin(alpha);
   y0 = sqrt(rd*rd - (x .* x));
   y1 = (d - y0);
   y2 = (- d + y0);
   plot(x,y1,':r',x,y2,':r');
end
axis('square');
```

```
theta = pi*(90-azimuth)/180 ;
rho = sqrt(2)*sin(pi*(90-dip)/360);
xp = rho .* cos(theta);
yp = rho .* sin(theta);


limits =[1 360 1 90];
levels=50;
    map = dataDensity(azimuth, dip, 360 ,90,limits);
    map = map - min(min(map));
    map = floor(map ./ max(max(map))* (levels-1));
    [xi,yi,zi] = Data_density_small(xp,yp);
    hold on;

     plot(xp,yp,'*k','markersize', 4);

    figure;
    hold on
    axis([-1 1 -1 1]);
axis('square');
plot(xh,yh,'-g',xv,yv,'-g');                        %plot green axes
axis off;
hold on;
plot(cx,cy,'-w');                                   %plot white circle
psi = [0:pi/N:pi];
    for i = 1:8                                         %plot great circles
   rdip = i*(pi/18);                                %at 10 deg intervals
   radip = atan(tan(rdip)*sin(psi));
   rproj = tan((pi/2 - radip)/2);
   x1 = rproj .* sin(psi);
   x2 = rproj .* (-sin(psi));
   y = rproj .* cos(psi);
   plot(x1,y,':r',x2,y,':r');
end
for i = 1:8                                        %plot small circles
   alpha = i*(pi/18);
   xlim = sin(alpha);
   ylim = cos(alpha);
   x = [-xlim:0.01:xlim];
   d = 1/cos(alpha);
   rd = d*sin(alpha);
   y0 = sqrt(rd*rd - (x .* x));
   y1 = d - y0;
   y2 = - d + y0;
   plot(x,y1,':r',x,y2,':r');
end
    contour(xi,yi,zi,'linewidth',1.5)
    zi_mean=mean(zi);
   size(map);
```

- Function Data_density_small calls Datadensity_newnew below and density contours points using counting circle. Function also runs mean filter over contours for smoothing

```
function [xi,yi,zi,dd] = Data_density_small(x,y)

% from KAMB 1959 --> r = sqrt(9/(pi*(n+9)))= 0.067
 dd = Datadensity_newnew(x,y,'method','circle','radius',0.067);
%  std = (n*pi*0.067^2)*sqrt((1- pi*0.067^2)/(n* pi*0.067^2)) % prints
stdeviation
dd=dd./std;

 N = 500;
xi = repmat(linspace(min(x(:)),max(x(:)),N),N,1);
yi = repmat(linspace(min(y(:)),max(y(:)),N)',1,N);
F = TriScatteredInterp(x,y,dd); %Construct interpolant
zi = F(xi,yi); %Interpolate scattered data
n =15; %running mean filter width
c = ones(n(1),1)/n(1); %running mean filter
zi(isnan(zi)) = 0;
zi = conv2(c,c,zi,'same');
dds = interp2(xi,yi,zi,x,y);
 colorbar
end
```

- Density Contours points using counting circle

```
function dd = Datadensity_newnew(x,y,varargin)
% datadensity Computes the data density (points/area) of scattered points
method = 'vo';
r = [];
for k=1:2:length(varargin)-1
    switch lower(varargin{k})
        case 'method'
            method = varargin{k+1};
        case 'radius'
            r = varargin{k+1};
        otherwise
            warning(['Unidentified Property: ',varargin{k}])
    end
end
if isempty(r)
    r = max(range(x),range(y))*0.05;
end
%Correct data if necessary
x = x(:); y = y(:);
%Asuming x and y match
idat = isfinite(x);
x = x(idat); y = y(idat);
%Initialize
Ld = length(x);
dd = zeros(Ld,1);
%Calculate Data Density
switch method(1:2)
    case 'sq'  %---- Using squares ----
        for k=1:Ld
```

```
            dd(k) = sum( x>(x(k)-r) & x<(x(k)+r) & y>(y(k)-r) & y<(y(k)+r) );
        end %for
        area = (2*r)^2;
        dd = dd/area;
    case 'ci'
        for k=1:Ld
            % AAAAAAAAAAAAAAAAAAAAAAAAAAAAA
            dd(k) = sum( sqrt((x-x(k)).^2 + (y-y(k)).^2) < r );
        end
        area = pi*r^2;

        % AAAAAAAAAAAAAAAAAAAA
    case 'vo'  %----- Using voronoi cells ------
        [v,c] = voronoin([x,y]);
        for k=1:length(c)
            %If at least one of the indices is 1,
            %then it is an open region, its area
            %is infinity and the data density is 0
            if all(c{k}>1)
                a = polyarea(v(c{k},1),v(c{k},2));
                dd(k) = 1/a;
            end %if
        end %for
    otherwise
        error('Invalid Method')
end %switch
%Relocate variables and place NaN's
dd(idat) = dd;
dd(~idat) = NaN;
return
```